

**Best
Available
Copy**

ADA131259

ATC REPORT NO. R-91100/2CR-4-B
ARPA ORDER NO. 4045-1

(12)

Afterbody Propulsor Performance Validation for A 2.65 Fineness Ratio Body Advanced Tactical Vehicle

VOUGHT CORPORATION ADVANCED TECHNOLOGY CENTER

P. O. BOX 225 S07

DALLAS, TEXAS 75265

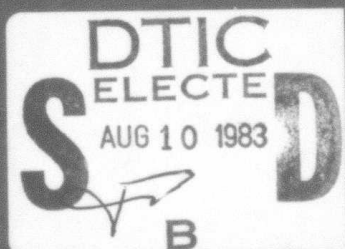
OCTOBER 1982

FINAL REPORT FOR PERIOD MAY 1981-MAY 1982

APPROVED FOR PUBLIC RELEASE; DISTRIBUTION UNLIMITED

SPONSORED BY:

DEFENSE ADVANCED RESEARCH PROJECTS AGENCY
1400 WILSON BLVD.
ARLINGTON, VA. 22209



DTIC FILE COPY



VOUGHT CORPORATION
Advanced Technology Center

83 07 29 006

AFTERBODY PROPULSOR PERFORMANCE VALIDATION FOR
A 2.65 FINENESS RATIO BODY
ADVANCED TACTICAL VEHICLE

FINAL REPORT

ATC REPORT NO. R-91100/2CR-49

Prepared by: J. G. Spangler
R. L. Mask
K. M. Krall

Sponsored by

DEFENSE ADVANCED RESEARCH PROJECTS AGENCY (DOD)
ARPA ORDER NO. 4045-1

and

AVIATION AND SURFACE EFFECTS DEPARTMENT
DAVID W. TAYLOR NAVAL SHIP RESEARCH AND DEVELOPMENT CENTER

Under Contract No. N00600-81-C-1334

The views and conclusions contained in this document are those of the authors and should not be interpreted as necessarily representing the official policies, either expressed or implied, of the Defense Advanced Research Projects Agency or the U.S. Government

VOUGHT CORPORATION ADVANCED TECHNOLOGY CENTER
P. O. BOX 226144
DALLAS, TEXAS 75266

UNCLASSIFIED

SECURITY CLASSIFICATION OF THIS PAGE (When Data Entered)

REPORT DOCUMENTATION PAGE		READ INSTRUCTIONS BEFORE COMPLETING FORM
1. REPORT NUMBER	2. GOVT ACCESSION NO.	3. RECIPIENT'S CATALOG NUMBER
	AD-A131 259	
4. TITLE (and Subtitle) AFTERBODY PROPULSOR PERFORMANCE VALIDATION FOR A 2.65 FINENESS RATIO BODY ADVANCED TACTICAL VEHICLE		5. TYPE OF REPORT & PERIOD COVERED FINAL REPORT MAY 1981 - MAY 1982
		6. PERFORMING ORG. REPORT NUMBER R-91100/2CR-49
7. AUTHOR(s) J. G. SPANGLER R. L. MASK K. M. KRALL		8. CONTRACT OR GRANT NUMBER(s) N00600-81-C-1334 ARPA ORDER NO. 4045-1
9. PERFORMING ORGANIZATION NAME AND ADDRESS VOUGHT CORPORATION ADVANCED TECHNOLOGY CENTER P. O. BOX 225907 DALLAS, TEXAS 75265		10. PROGRAM ELEMENT, PROJECT, TASK AREA & WORK UNIT NUMBERS
11. CONTROLLING OFFICE NAME AND ADDRESS DEFENSE ADVANCED PROJECTS AGENCY 1400 WILSON BLVD. ARLINGTON, VA 22209		12. REPORT DATE OCTOBER 1982
14. MONITORING AGENCY NAME & ADDRESS (if different from Controlling Office) DAVID W. TAYLOR NAVAL SHIP RESEARCH AND DEVELOPMENT CENTER BETHESDA, MD 20084		13. NUMBER OF PAGES 145
		14a. SECURITY CLASS. (of this report) UNCLASSIFIED
		14b. DECLASSIFICATION/DOWNGRADING SCHEDULE
16. DISTRIBUTION STATEMENT (of this Report) APPROVAL FOR PUBLIC RELEASE; DISTRIBUTION UNLIMITED		
17. DISTRIBUTION STATEMENT (of the abstract entered in Block 20, if different from Report)		
18. SUPPLEMENTARY NOTES		
19. KEY WORDS (Continue on reverse side if necessary and identify by block number) HYDRODYNAMIC DRAG/PROPULSION, BOUNDARY LAYER CONTROL, PROPULSION INTEGRATION, JET-BOUNDARY LAYER MIXING, ANNULAR INLETS/DIFFUSERS, ADVANCED UNDERWATER VEHICLES		
20. ABSTRACT (Continue on reverse side if necessary and identify by block number) This report presents the results from a low-speed wind tunnel test of a unique low-drag fineness-ratio-2.65 vehicle concept employing integrated boundary layer control and propulsion. The concept is based on the efficient energization of the body's boundary layer by blowing as it enters the strong adverse pressure gradient on a full and blunt afterbody. The boundary layer energization is accomplished with a full-circumferential blowing jet, designed to achieve fully-attached afterbody		

UNCLASSIFIED

SECURITY CLASSIFICATION OF THIS PAGE (When Data Entered)

flow while also providing sufficient thrust to achieve self-propulsion with low installed-power.

The analytical methodology for analysis and evaluation of the total concept, as well as the individual components, is presented and compared with wind tunnel test data. Analytical prediction accuracy has been completely validated for both turbulent and laminar vehicle configurations.

Additional considerations for a total vehicle, such as propulsor inlet performance and stability and control requirements, are also addressed analytically and experimentally.

The validity and accuracy of wind tunnel testing to obtain the performance characteristics of underwater vehicles is provided by excellent agreement of wind tunnel results with free-running in-water range test data for the laminar flow configuration.

Finally, the predictive methodology is applied to the analysis of mission capable configurations. Performance evaluations are provided for an improved Advanced Tactical Vehicle (ATV) of 2.75 fineness ratio and an Advanced Underwater Vehicle (AUV) with fineness ratio of 4.7. The predicted performance of the AUV illustrates the advantages of the compact propulsive afterbody for weapon applications. Along with a high prismatic coefficient body, and within geometric constraints to match selected launch platforms, the AUV configuration provides a substantial reduction in required propulsive power characteristics compared to all other configurations considered.

S/N 0102-LF-014-6601

UNCLASSIFIED

SECURITY CLASSIFICATION OF THIS PAGE (When Data Entered)

ACKNOWLEDGEMENTS

This work was sponsored by the Defense Advanced Research Projects Agency and administrated through the David Taylor Naval Ship Research and Development Center under contract No. N00600-81-C-1334.

RE: Classified References, Distribution Un-limited
No change per Mr. Bob Wilson, DTNSRDC/ASE

Acceptability	
NTIS	Open
DTIC	<input type="checkbox"/>
Unpublished	<input type="checkbox"/>
Justification	
By _____	
Distribution/ _____	
Availability Codes	
Dist	Avail and/or Special
A	



CONTENTS

<u>SECTION</u>	<u>PAGE NO.</u>
ACKNOWLEDGEMENTS	iii
NOMENCLATURE	vii
1.0 INTRODUCTION	1
1.1 BACKGROUND	1
1.2 OBJECTIVES	4
1.3 APPROACH	4
2.0 CONCEPT DESCRIPTION/METHODOLOGY	6
2.1 VEHICLE CONFIGURATION	6
2.1.1 Forebody	6
2.1.2 Centerbody Shroud	7
2.1.3 Afterbody	7
2.1.4 BLC Propulsor	8
2.1.5 Inlet Design and Analysis	10
2.2 ANALYTICAL METHODOLOGY	15
2.2.1 Body Shapes and Static Pressure Distribution	15
2.2.2 Drag Constituents	15
2.2.2.1 Forebody Drag	19
2.2.2.2 Spillage Drag	19
2.2.2.3 Shroud Drag	19
2.2.2.4 Afterbody Drag	23
2.2.2.5 Fin Drag	25
2.2.3 Total Aft-body Drag/Thrust Requirements	28
2.2.4 Propulsor Power	31
2.2.4.1 Inlet Power Accounting	31
2.2.4.2 BLC Jet Power	32
2.2.5 Stability and Control Surface Effectiveness	34
2.2.6 Vehicle Performance	37
3.0 TEST PROGRAM	40
3.1 MODEL CONFIGURATIONS	40
3.1.1 Hydrodynamic Demonstration Vehicle (HDV)	40
3.1.2 Improved Range Vehicle (IRV)	40
3.1.3 Advanced Tactical Vehicle (ATV)	42
3.1.4 Inlet Candidates	44

CONTENTS (Continued)

<u>SECTION</u>		<u>PAGE NO.</u>
3.2	FACILITIES AND SUPPORT SYSTEMS	44
3.2.1	Vought Low Speed Wind Tunnel	44
3.2.2	Model Mounting Facility	48
3.2.2.1	Main Support Strut	48
3.2.2.2	Image Strut	52
3.2.2.3	Bellows Assembly	52
3.2.2.4	Force Balance Adapter	52
3.2.2.5	Force and Moment Balance	53
3.2.3	Auxilliary Air System	53
3.2.4	Test Plan	53
4.0	INSTRUMENTATION	58
4.1	FORCE AND MOMENT BALANCE	58
4.2	BODY STATIC PRESSURE	58
4.3	TOTAL PRESSURE RAKES	58
4.3.1	Forebody Rakes	59
4.3.2	Inlet Rakes	59
4.3.3	Centerbody Spillage Rakes	61
4.3.4	Centerbody Boundary Layer Rakes	61
4.3.5	BLC Jet Rakes	62
4.3.6	Afterbody Wake Rakes	62
4.3.7	Preston Tubes	63
4.3.8	Far Wake Rakes	63
4.4	MASS FLOW METERS	63
4.5	PRESSURE MEASUREMENTS MULTIPLEXING	69
5.0	TEST RESULTS	70
5.1	STATIC PRESSURE DISTRIBUTIONS	70
5.1.1	HDV Static Pressure Distribution	70
5.1.2	IRV Static Pressure Distribution	70
5.1.3	ATV Static Pressure Distribution	70
5.2	FOREBODY BOUNDARY LAYER VELOCITY PROFILES	74
5.2.1	Laminar Body Velocity Profiles	74
5.2.2	ATV Forebody Boundary Layer	76
5.3	INLET PERFORMANCE	76
5.3.1	HDV Radial Inlet	76
5.3.2	Submerged Inlet	79
5.3.3	Axial Pre-diffusing Inlet	79

CONTENTS (Continued)

NOMENCLATURE

A	-	area
c	-	fin chord
C_{ax}	-	measured axial force coefficient
C_D	-	drag coefficient, $D/q_\infty V^2/3$
C_f	-	skin friction coefficient
C_M	-	pitching moment coefficient, $PM/q_\infty V^2/3L$
C_{net}	-	net axial force coefficient
C_N	-	normal force coefficient, $NF/q_\infty V^2/3$
C_P	-	power coefficient, $P/q_\infty U_\infty V^2/3$
C_p	-	static pressure coefficient, $(P-P_\infty)/q_\infty$
C_Q	-	flow coefficient, $Q/U_\infty V^2/3$
C_T	-	thrust coefficient, $T/q_\infty V^2/3$
D	-	drag force
h	-	jet exit width
H	-	total pressure
\hat{H}	-	boundary layer shape factor, δ^*/θ
L	-	body length
l/d	-	body fineness ratio, length/diameter
\dot{m}	-	mass flow rate
n	-	velocity profile power law exponent
N	-	quantity
NF	-	normal force
p	-	static pressure
P	-	fluid power
PM	-	pitching moment
q	-	dynamic pressure, $1/2 \rho U^2$
Q	-	inlet/BLC volume flow rate
r	-	radius
Re_L	-	length Reynolds number, $U_\infty L/\nu$
$Re_{V^{1/3}}$	-	volume Reynolds number, $U_\infty V^{1/3}/\nu$
s	-	arc or surface length
T	-	thrust force
u	-	local velocity
U_∞	-	freestream velocity
U_e	-	local velocity at edge of boundary layer

NOMENCLATURE (Continued)

U_j	- jet exit velocity
U_L	- local velocity outside of boundary layer
V	- body volume
V_j	- jet exit velocity expanded to freestream static pressure
x	- axial distance
y	- radial distance
α	- angle of attack
δ	- boundary layer thickness
δ^*	- boundary layer displacement thickness
δ_F	- fin deflection angle
θ	- boundary layer momentum thickness
λ_v	- viscous blockage factor, Q_{int}/Q_{inv}
ρ	- fluid density
ψ	- stream function, eqn. (2-11)

SUBSCRIPTS

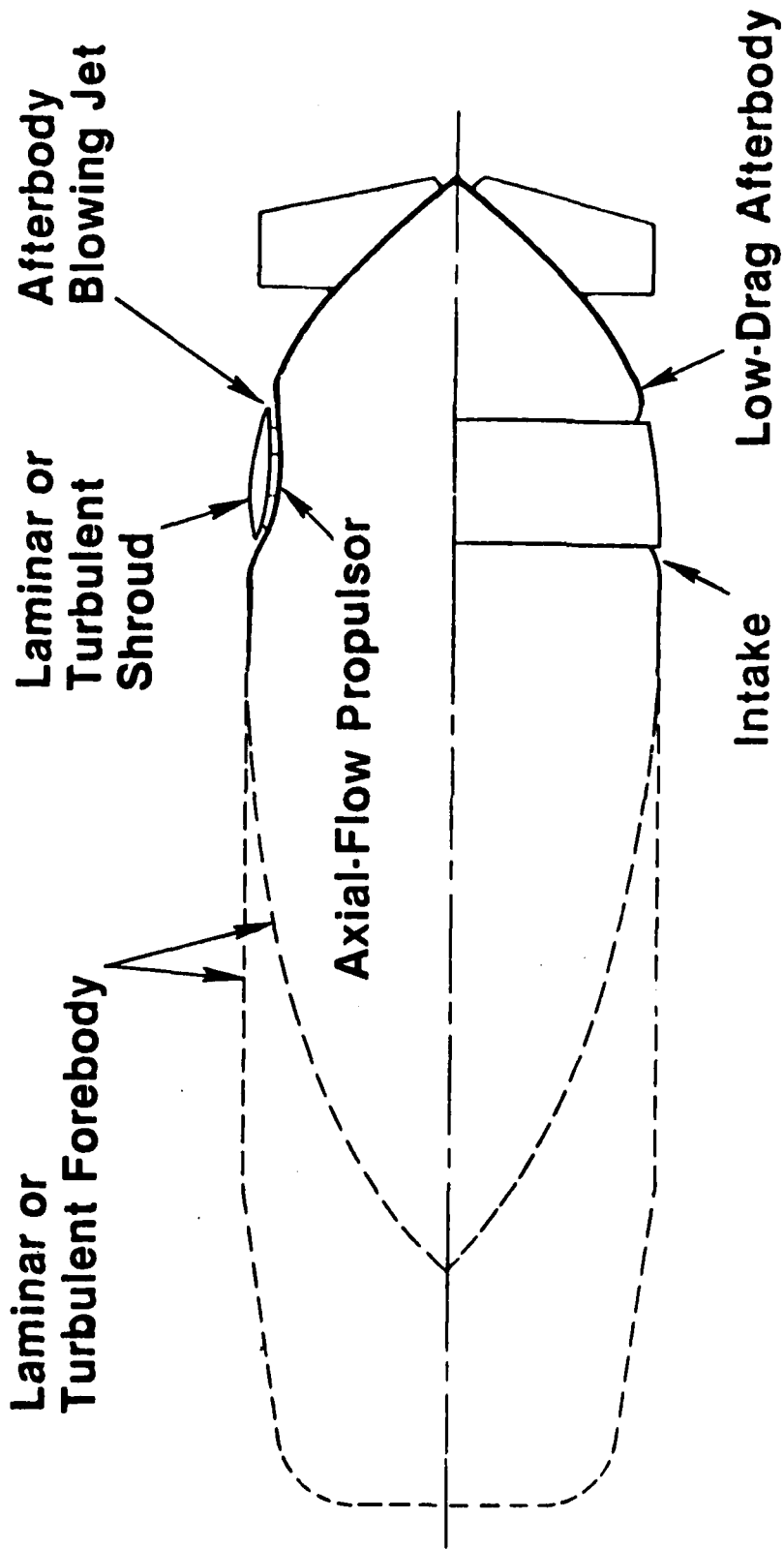
Aft-Body	- entire aft-body assembly
A/B	- afterbody
bal	- force balance measurement
F/B	- forebody
i	- inlet
in	- ingested
int	- integrated value
inv	- inviscid
lip	- BLC jet nozzle lip station
meas	- measured quantity
∞	- freestream value
1	- body station just head of inlet

1.0 INTRODUCTION

1.1 BACKGROUND

The validation objectives addressed in this program have evolved from previous work spanning the last several years. The Vought integrated afterbody propulsor concept is an outgrowth of boundary layer control (BLC) technology for high-lift airfoils and wings and was developed in the company-funded IR&D program. The BLC concept was subsequently converted to an axisymmetric application and expanded to provide propulsive thrust for a vehicle configuration.

The unique vehicle configuration, based on the propulsive afterbody concept, is illustrated in Figure 1-1. As indicated, the concept fundamentally can be applied to either laminar or turbulent-flow configurations and provides benefits of lower drag and increased available volume. Boundary layer control is employed both by ingesting viscous forebody fluid into the intake and providing boundary layer energization on the body prior to fluid deceleration on the afterbody. Previous airfoil/wing applications verified the blowing-jet BLC effectiveness, while the boundary layer inlet feature was implemented for vehicle propulsion applications. A laminar-flow vehicle arrangement, embodying the BLC-propulsive principles is shown in Figure 1-2. This configuration is specifically relevant to the current study since it provided both test hardware as well as a free-running test data base with which to validate wind tunnel test suitability for this generic type of integrated propulsor. A free-running in-water test program¹ was previously conducted to demonstrate the speed/power characteristics of the laminar flow/integrated afterbody propulsor configuration. Results of laboratory and range tests of the Vought design (designated Hydrodynamic Demonstration Vehicle, or HDV) are reported in references 2-8 and summary assessments of demonstrated and potential performance are given in references 9-11. Although the feasibility of simultaneously providing propulsion and boundary layer control was verified, the performance objectives were not achieved due to off-design operation of the integrated propulsor components (intake/pump). The key elements for an efficient integrated BLC afterbody propulsor include achievement of low afterbody drag at self-propulsion, and a suitable inlet for highly viscous (highly blocked) intake flows. The test program described in this report effectively resolved these issues and provided methodology validation to assess the applicability



- Rapid closure, low form drag
- Combined propulsion-flow control
- Efficient packaging of propulsor (larger prismatic coefficient)
- Adaptable to either laminar or turbulent forebodies

FIGURE 1-1 BLC-PROPELLIVE AFTERBODY CONCEPT

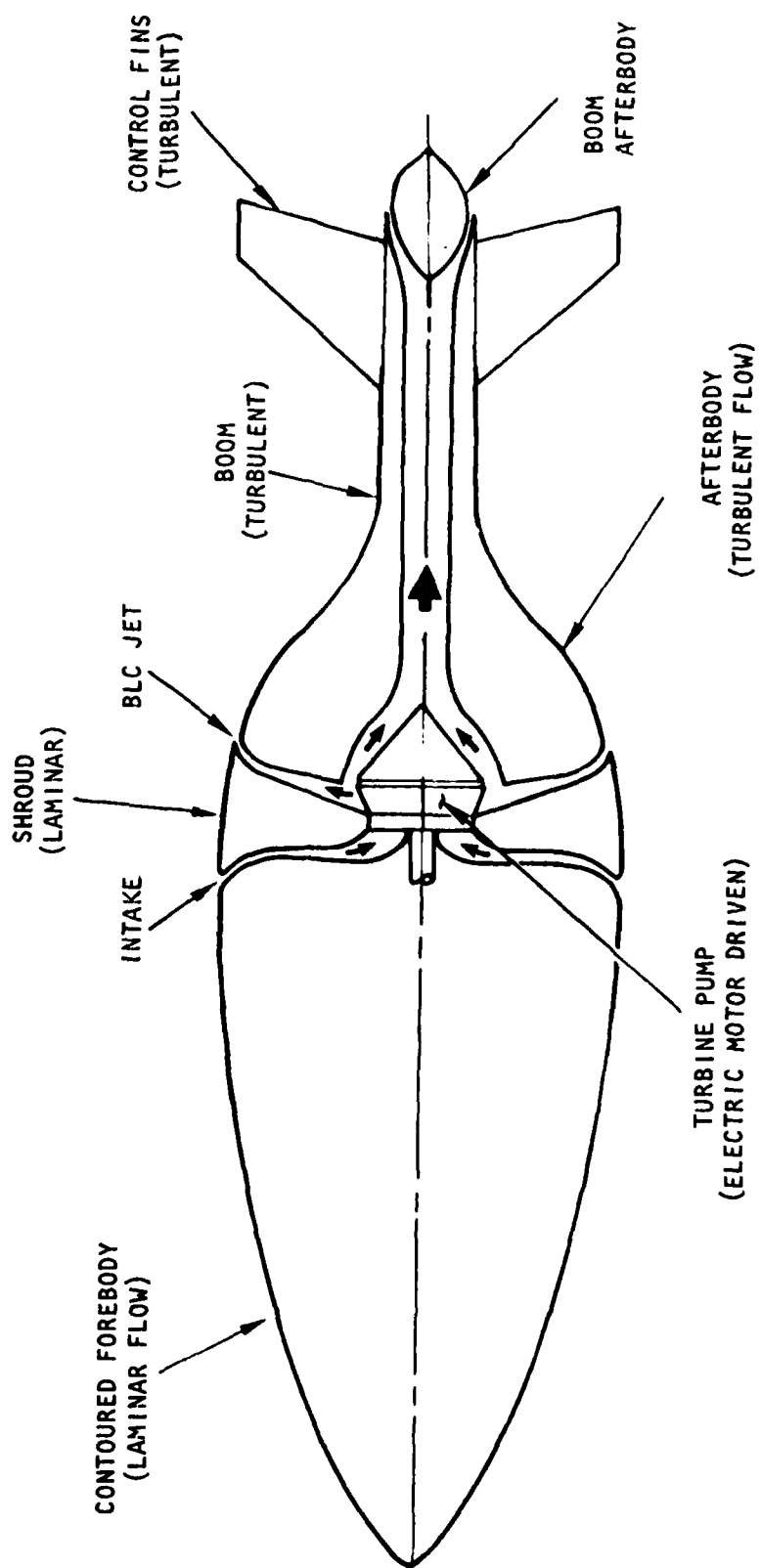


FIGURE 1-2 HYDRODEMOSNTRATION VEHICLE ARRANGEMENT

of the afterbody propulsor concept to new aerodynamic and underwater tactical vehicle configurations, including consideration of stability and control fin effectiveness.

1.2 OBJECTIVES

The overall objective of this program is to demonstrate the speed/in-stalled-power performance benefits of a class of advanced tactical vehicles employing the Vought integrated propulsive/BLC afterbody. Specific objectives are:

- (1) Demonstrate hydrodynamic propulsive performance for a 2.65 fineness-ratio turbulent-flow body employing an integrated propulsive/BLC afterbody.
- (2) Provide wind tunnel test validity for hydrodynamic vehicles by comparing with in-water free-running test vehicle performance.
- (3) Verify the "design fix" for the range test vehicle.
- (4) Assess the applicability of this concept to advanced underwater vehicles.

1.3 APPROACH

Inherent in the integrated afterbody propulsor concept is a strong interdependence between thrust and vehicle drag which precludes separate evaluation of thrust and drag characteristics, as is customarily done in more conventionally propelled configurations. Without blowing (thrust) the afterbody boundary layer will separate causing large drag, while on the other hand, adjustment of BLC blowing conditions to just prevent separation may not provide sufficient thrust for self-propulsion. Increasing the jet velocity to achieve self-propulsion can induce high skin friction drag on the afterbody and large internal viscous losses in the propulsor that seriously degrade the overall propulsive efficiency. It is thus the nature of the BLC blowing jet that is the critical factor. These considerations require that testing should be conducted at or near self-propulsion conditions with a powered test model.

The approach chosen to accomplish the program objectives was a comprehensive subsonic wind tunnel test in which individual BLC components of the integrated afterbody propulsor could be independently evaluated while testing the complete system (i.e., the intake flow and BLC blowing jet were independently controlled). Verification of wind tunnel testing as an accurate evaluation of hydrodynamic performance for an integrated propulsor of this type was provided by testing the original HDV range test vehicle in the wind tunnel as an air-powered model and correlating the data directly with the in-water free-running range test results. Additionally, the "design fix" changes considered in references 9-11 to improve the HDV performance could be evaluated.

This approach also benefitted from using a substantial portion of the existing HDV hardware modified to accept interchangeable components that allowed testing of a wide range of vehicle configurations. A moderate amount of effort was required to modify the HDV hardware and create four interchangeable inlet sets, a closed afterbody with no tailboom, and two new sets of fins that could be mounted to the afterbody. These modifications and additions provided the capability to test the original laminar HDV range vehicle configuration, an improved laminar range vehicle configuration (IRV), and a new fully-turbulent configuration for advanced tactical vehicles (ATV) in the same wind tunnel test series by simply exchanging various modular components.

Special consideration was also given to instrumentation, including complete static pressure distributions, boundary layer survey rakes, afterbody flowfield surveys, propulsor flow metering (intake and BLC jet), an internal force/moment balance, and near-wake survey rake. In addition to providing redundant measurements as well as axisymmetric checks, this detailed flowfield information provided the means to validate analytic prediction methodology. Analytical predictability is imperative for an assessment of the afterbody propulsor performance for alternate vehicle configurations, as will be discussed later in this report.

The test was tailored to use the Vought Low Speed Wind Tunnel in order to make use of existing support facilities for powered model testing. The available test conditions, coupled with the basic HDV model size, provided a Reynolds number range that matched the low-speed portion of the HDV in-water data base and coincided with the anticipated Reynolds number range for representative full-scale advanced underwater vehicle applications.

2.0 CONCEPT DESCRIPTION/METHODOLOGY

The general configuration for a vehicle with an integrated afterbody propulsor and the methodology used to analyze and predict its performance characteristics are described in this section. The described approach is applicable and valid for both aerodynamic and hydrodynamic vehicles. For simplification, and because of the relevance to current interests the following descriptions deal primarily with hydrodynamic applications.

2.1 VEHICLE CONFIGURATION

An advanced underwater vehicle with an integrated afterbody propulsor may be thought of as consisting of separate identifiable components (i.e., forebody, centerbody shroud, afterbody, propulsor/BLC jet, and control or lifting surfaces) as illustrated in Figure 2-1.

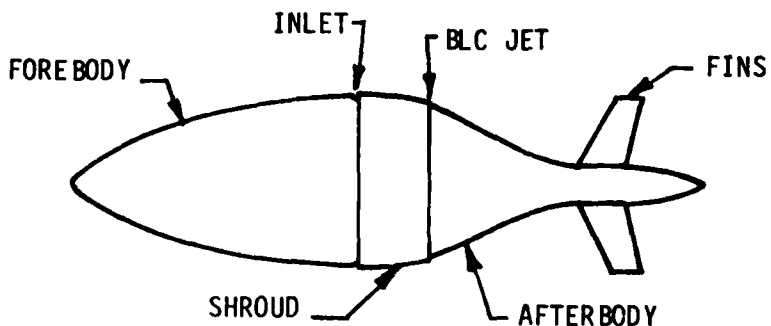


FIGURE 2-1 VEHICLE COMPONENTS

2.1.1 Forebody

The forebody is the portion of the vehicle ahead of the propulsor inlet and may be configured for either laminar or turbulent boundary layer flow. The HDV test vehicle design was based on a fully laminar flow forebody for minimum drag and high speed. The Advanced Tactical Vehicle configuration used a turbulent forebody. For convenience the HDV forebody was used in all tests and the boundary layer was artificially tripped on the ATV.

2.1.2 Centerbody Shroud

The centerbody shroud is that portion of the vehicle envelope that extends from the propulsor inlet to the BLC jet exit. The boundary layer on the shroud may be in any of three states, depending on the vehicle Reynolds number and the ingested mass flow rate in the propulsor inlet. If the entire forebody boundary layer (either laminar or turbulent) is ingested, a new boundary layer is started at the forward edge of the shroud and proceeds to develop along its length. Depending on the local unit Reynolds number, the shroud length and shape (pressure distribution), the developing shroud boundary layer may be laminar over the entire shroud or it may transition to turbulent flow at some point before reaching the BLC/propulsive jet station. If the forebody boundary layer is turbulent and not totally ingested, a portion of it will "spill over" on to the centerbody shroud. This viscous spillage will establish a turbulent boundary layer flow over the shroud whose characteristics will be dependent on the forebody boundary layer and the amount of the spillage momentum deficit. The momentum deficit in the flow at the end of the shroud is paramount in the design of the BLC/propulsive afterbody and will be discussed in the following paragraphs.

2.1.3 Afterbody

The afterbody is the aft-most portion of the vehicle that extends from the jet exit to the terminus. The specific shape and length of the afterbody is uniquely dependent on the efficient integration of BLC. Drag considerations prescribe that the afterbody be as blunt and short as possible. Since afterbody drag is one of the primary considerations for developing an optimized low installed-power configuration, the shaping of the afterbody depends directly on the ability of the BLC jet to keep the flow fully attached down to the body terminus. However, when the BLC jet flow is also required to provide the propulsive thrust it becomes obvious that the afterbody shape is dependent on the flow conditions at the shroud trailing edge, the jet/boundary layer mixing dynamics, and the internal geometry of the propulsor. This will be further explained in the following discussion of the propulsor system.

2.1.4 BLC Propulsor

The propulsor unit for this type of vehicle has a dual role - providing propulsive thrust and energizing the external boundary layer to maintain fully attached flow at minimum drag. The mechanics of afterbody propulsor matching are illustrated in Figure 2-2. The efficiency of the propulsor unit will be sensitive to the internal viscous flow energy losses. These will be a function of the total flow rate required for self-propulsion and optimum BLC. Since the propulsor inlet ingests boundary layer flow, thrust requirements can be provided with lower energy input than for a freestream inlet. Thus the ideal propulsive efficiency (no blading or ducting losses) could exceed unity, if the average inlet velocity is less than freestream. The momentum deficit due to the viscous losses in the fraction of the boundary layer that is ingested into the inlet does not contribute to the resultant vehicle drag and thus is book-kept as a propulsor loss. The BLC jet must supply sufficient thrust to overcome the resultant vehicle drag. At self-propulsion the propulsor fluid power requirement is determined simply from the difference between the BLC jet exhaust and inlet flow at zero net axial force.

The exit flow propulsor requirements are set by the momentum deficit in the exiting shroud boundary layer (dependent on "spillage," if any, and thus related to the mass flow ingestion of the inlet), the afterbody drag characteristics (intimately related to the contour closure rate, the vehicle Reynolds number, and the mixing dynamics of the jet and viscous flow over the afterbody), and the drag of any control fins, lifting surfaces, or other protuberances. In particular, for any given design point, there will be an optimum blowing jet definition (i.e., velocity and flow rate) that will provide enough momentum addition to energize the boundary layer and overcome the extraneous component drag while producing minimum afterbody drag. This condition constitutes optimum self-propulsion.

This program only addressed the inlet flow and jet exhaust characteristics for the internal propulsor. The performance characteristics of an internal pump are considered to be uniquely dependent on the impeller/stator design (given inlet and exit flow definitions) and can be subsequently pursued once flow rate and head requirements are established. Suffice it to say that test results from this program provide the characteristics necessary to define the pump blading by using flow surveys taken inside the inlet and at the jet exit.

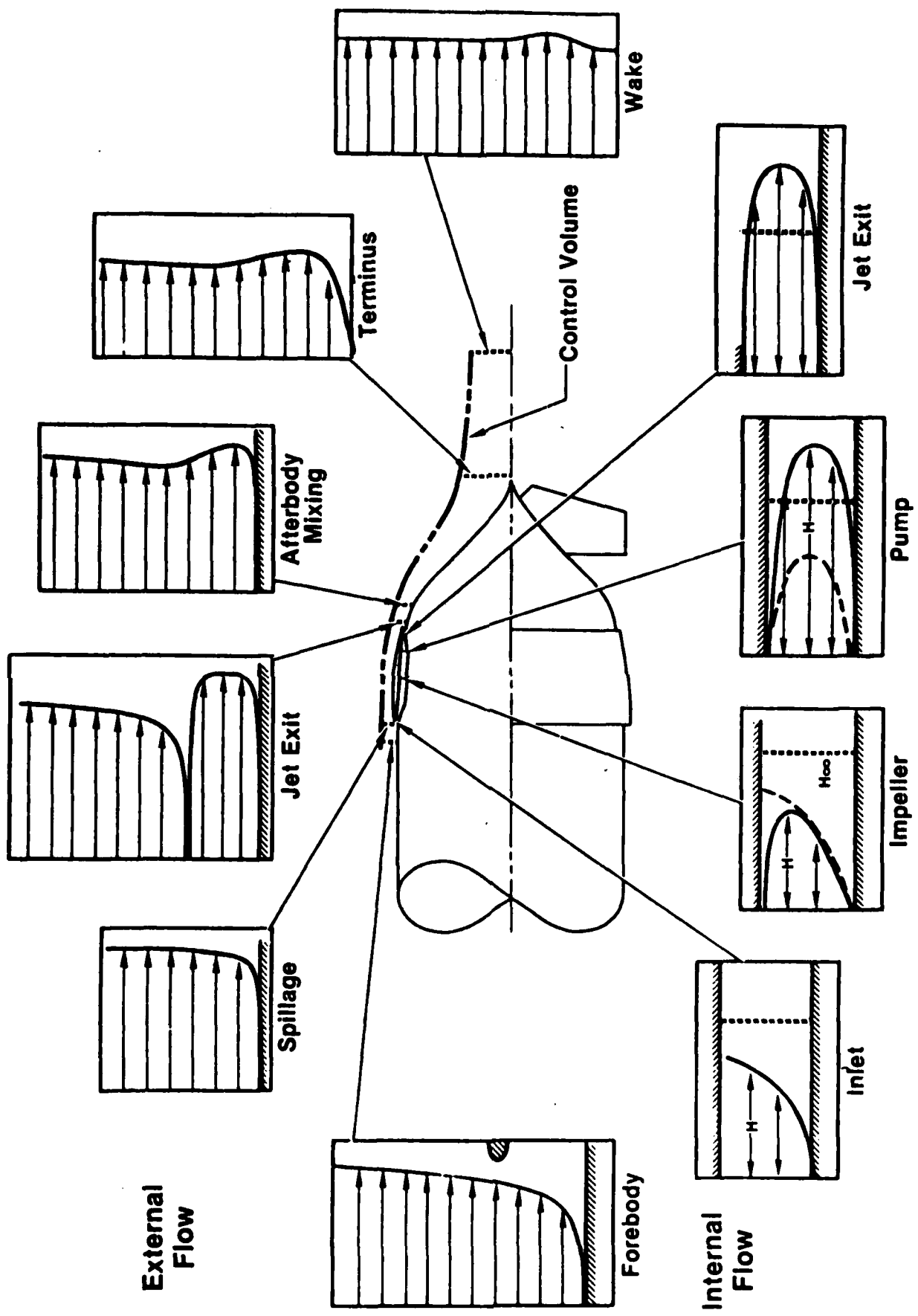


FIGURE 2-2 BLC-PROPELLIVE AFTERBODY FLOW MATCHING CONSIDERATIONS

2.1.5 Inlet Design and Analysis

Integration of an inlet into the body of a vehicle of the type under consideration presents some complex problems. The overall body shape is selected to provide a desired pressure distribution that is provided by a potential flow solution of the closed body. The inlet and intake channel designs depend on knowing the incoming flow velocity and pressure distribution. However, imposition of an inlet onto the body will perturb the local body static pressure and velocity and create a local flow situation that is different from the closed body. The local streamline pattern will also be strongly dependent on the ingested inlet flow rate. The location of the stagnation point for the capture area streamline will be influenced by local geometry as well as the flow rate. Subtle changes in local body contour can have strong effects on whether the flow enters the inlet in a constant velocity, diffusing, or accelerating mode. This will have an affect on the skewness of the velocity profile entering the inlet and be a dominant factor in the degree of blockage presented to the inlet. These factors need to be quantified in order to define the intake channel shape for efficient performance. However, all of the flow phenomena just described are highly viscous in nature and no comprehensive analysis techniques are presently available.

An approach for the design and analysis of integrated axisymmetric inlets that was used in this study is based on the Schmidt routine¹² that is an axisymmetric potential flow field engine inlet analysis computer code. The Schmidt routine calculates flow streamlines, inviscid wall pressure distributions, and inviscid flow skewness; given a geometry, free stream flow, and inlet flow rate. The boundary conditions are defined by a coordinate grid network. The maximum grid size is limited to 2500 points but can be tailored with combinations of local coarse and fine meshes to best describe the boundaries in the regions of most interest. Initial values for geometry, free-stream velocity, and inlet flow rate are selected and a potential flow solution is generated through a relaxation process. Several iterations with adjustment of the boundary conditions may be necessary to get a final satisfactory solution.

First order viscous flow corrections are made by applying conventional boundary layer calculations to the flow as it develops on the internal surfaces. The inviscid mass flow rate can then be adjusted according to estimates of blockage and total pressure losses and the potential flow solution is re-calculated and iterated with the viscous corrections.

The overall flowfield and near-field inlet grids representative of this type of solution are illustrated in Figures 2-3 and 2-4, set up for calculations of the submerged inlet, which evolved as the "improved inlet" for the laminar HDV configuration. Figure 2-5 compares the predictions of this technique with those generated with a rheo-electric analogy⁸ for the original HDV radial inlet. The primary objective of the HDV design was to prevent a sharp pressure spike and adverse gradient on the shroud that would lead to boundary layer transition. The finite-difference technique allowed later refinements to the original radial inlet that maintained the laminar external flow while providing less skewness and blockage in the inlet and thus lower power losses. Performance predictions for all of the inlet configurations generated for this study will be presented in the discussion of test results.

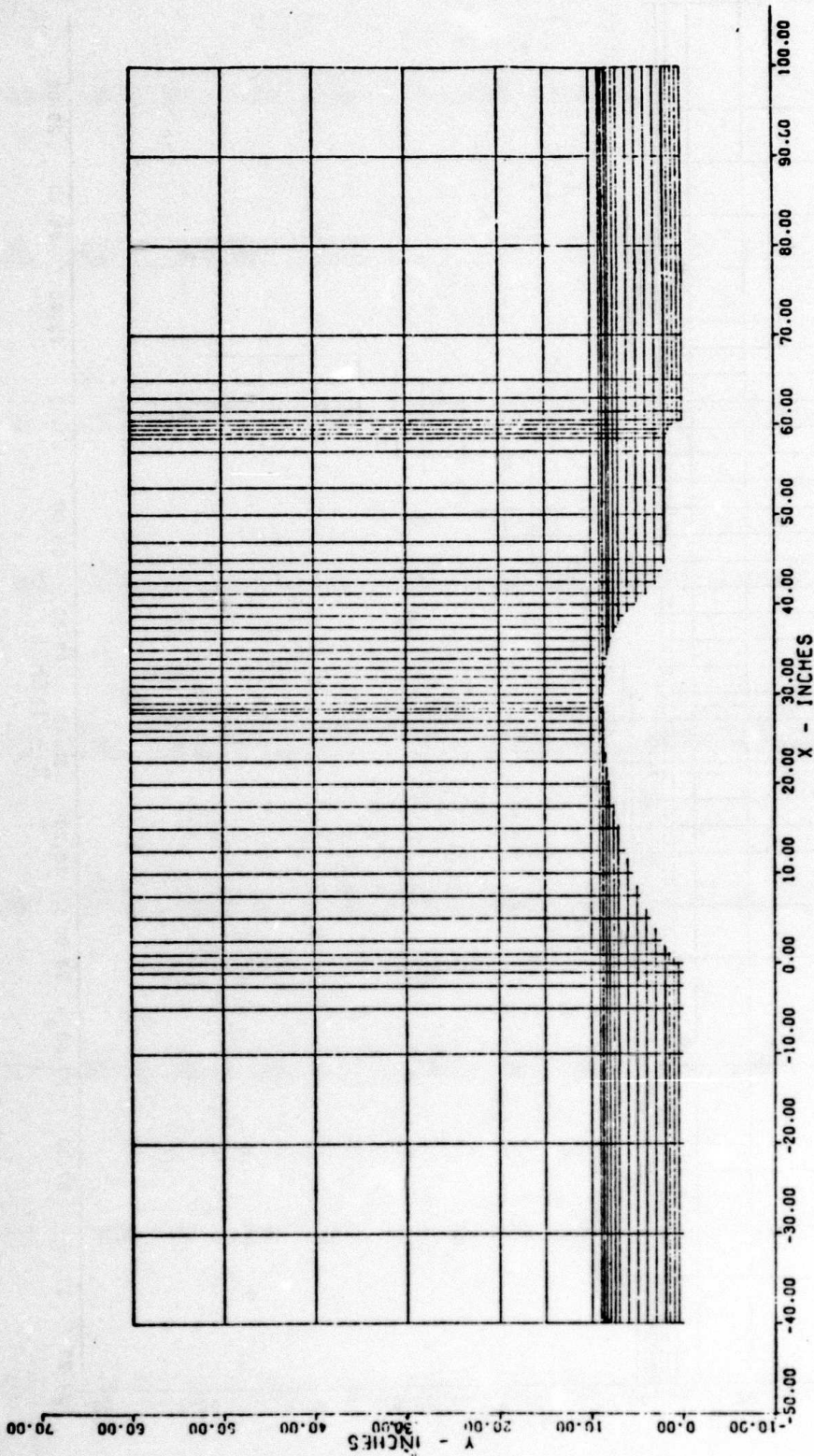


FIGURE 2-3. OVERALL FLOWFIELD GRID

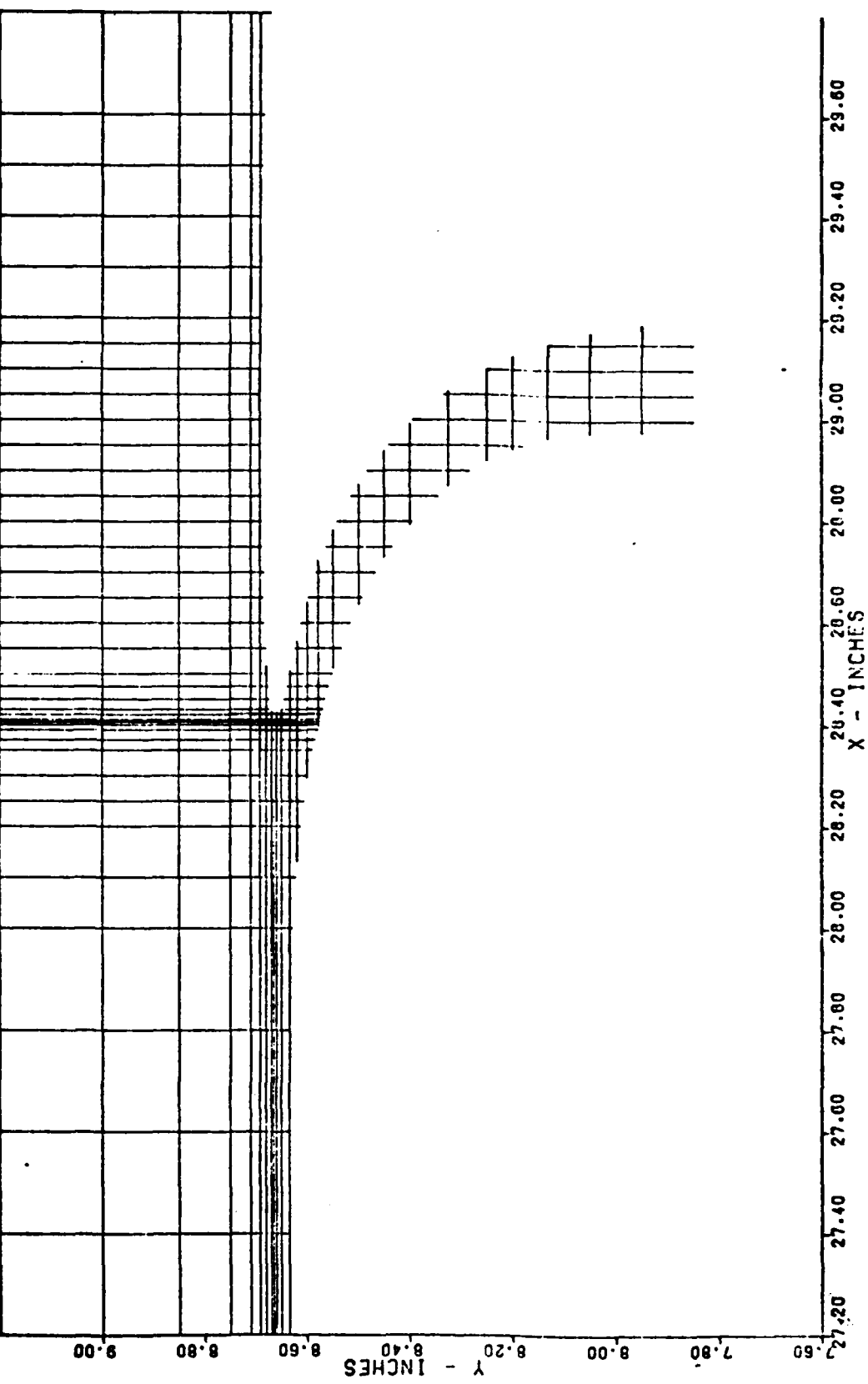


FIGURE 2-4. NEAR-FIELD INLET GRID

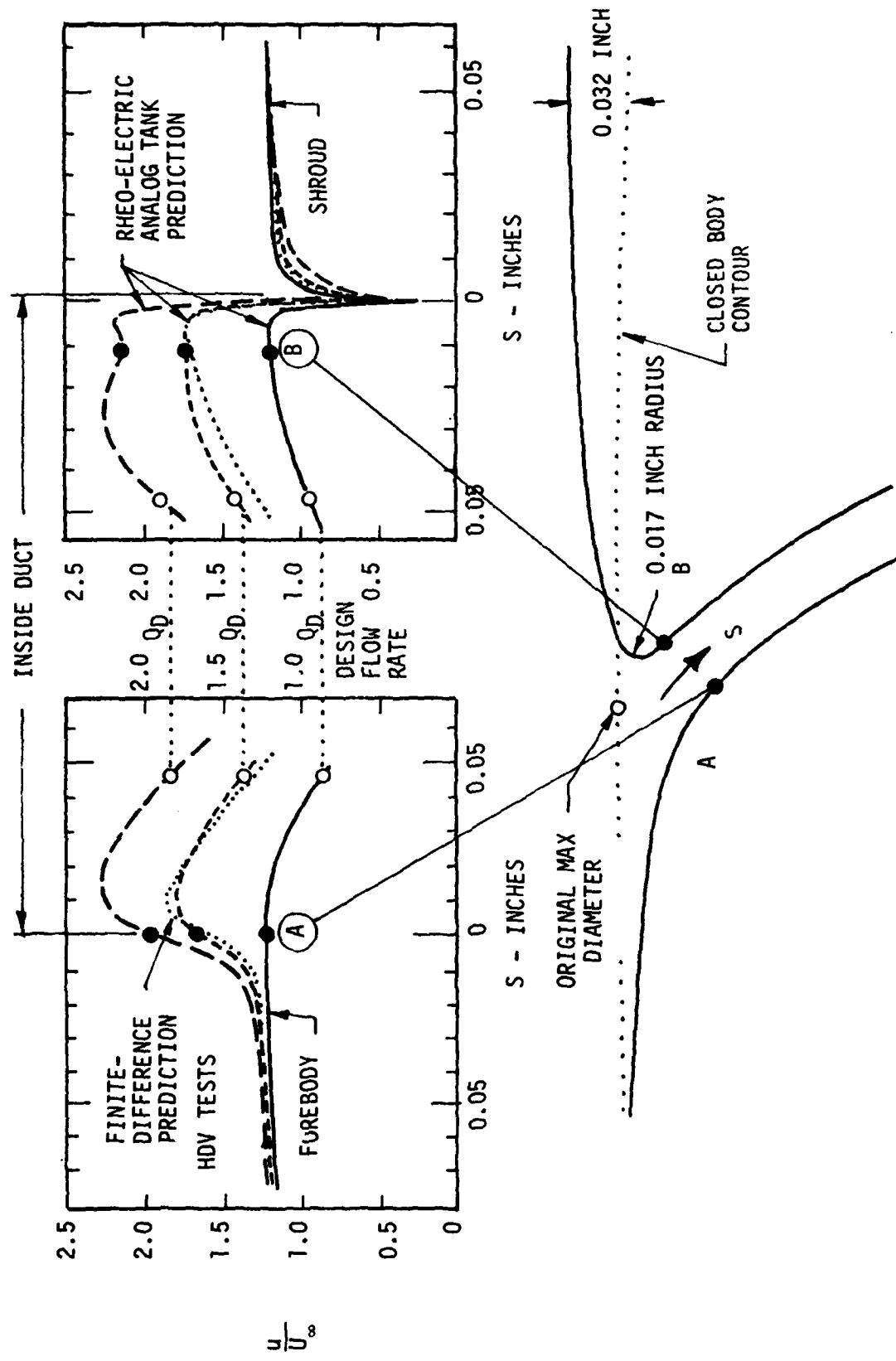


FIGURE 2-5: RADIAL INLET GEMOETRY-PREDICTED VELOCITY DISTRIBUTION

2.2 ANALYTICAL METHODOLOGY

The basic concept thesis for an integrated afterbody propulsor vehicle configuration is, that when properly done, BLC will provide a flow environment about the vehicle that very closely approximates potential flow thus effectively eliminating form drag. This reduces the self-propulsion BLC jet thrust requirement to only that necessary to overcome the spillage momentum deficit, the viscous losses incurred on the shroud, the afterbody drag, and the total drag of fins or other protuberances. The methodology employed in the design and evaluation of such a system will now be described.

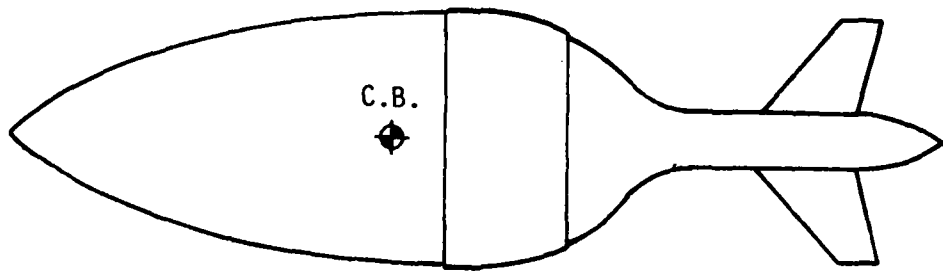
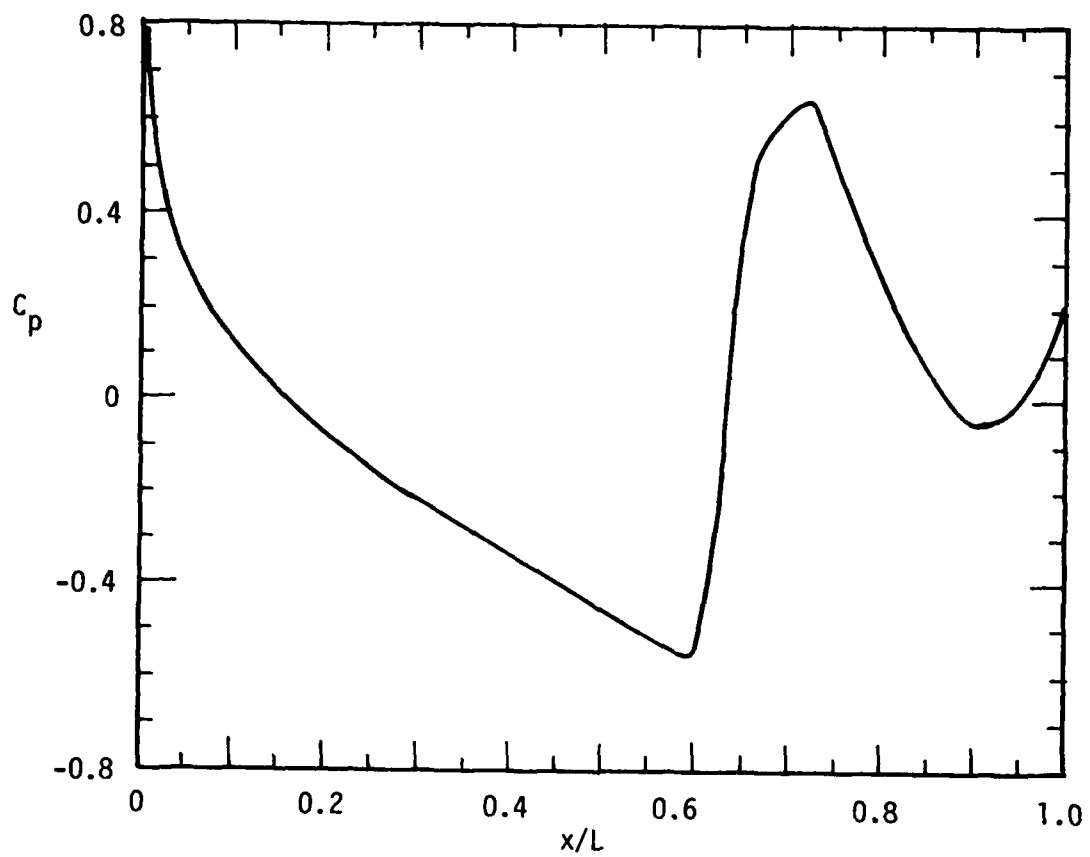
2.2.1 Body Shapes and Static Pressure Distribution

The axisymmetric potential flow routine in the Transition Analysis Program System (TAPS)¹³ was used to calculate the flow field around the bodies. This code can be used to calculate the inviscid static pressure distribution over a specified body shape or used to define the body shape required to produce a desired pressure distribution (e.g., the afterbody). Potential flow solutions may be iterated with boundary layer calculations to establish final body contour/pressure distributions that include boundary layer displacement effects. Additional, more sophisticated potential flow treatments are applied in the inlet region to integrate the inlet into the overall body shape as were discussed in Section 2.1.5.

Body specifications and the potential flow pressure distributions for the test vehicle configurations are provided in Figures 2-6 to 2-8. The strong, favorable forebody pressure gradient is typical of high-Reynolds number laminar flow configurations. As shown, the favorable pressure gradient extends just past the BLC-propulsive jet location. The following abrupt body closure on the afterbody generates very low velocities (high pressure recovery). The long tail boom on the range test vehicle was provided to simplify guidance/-control system requirements.

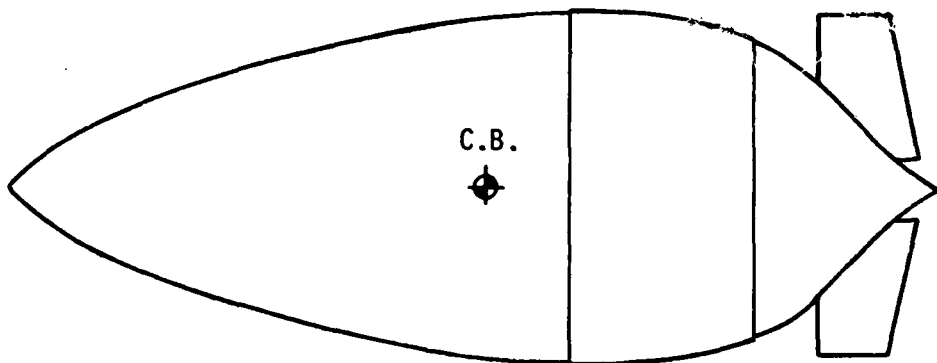
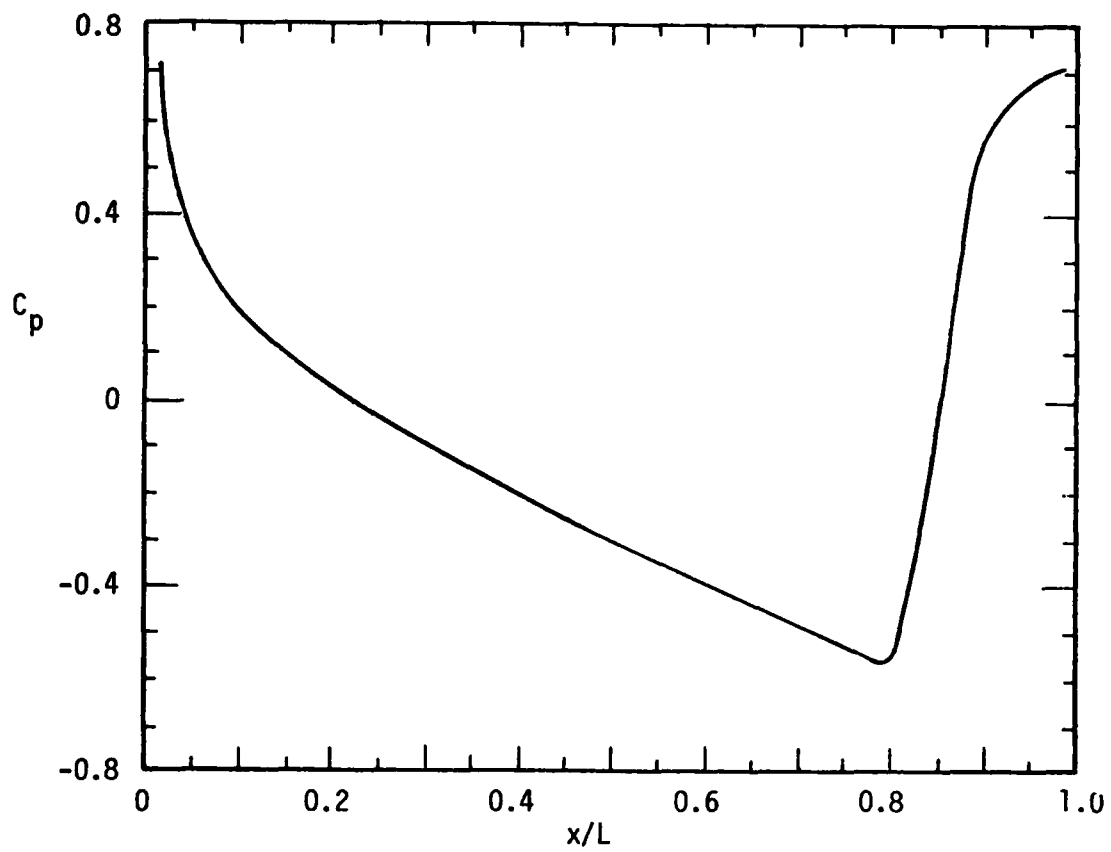
2.2.2 Drag Constituents

Although the vehicle configuration consists of separate components as identified in Figure 2-1, the interactions described in Section 1.3 preclude



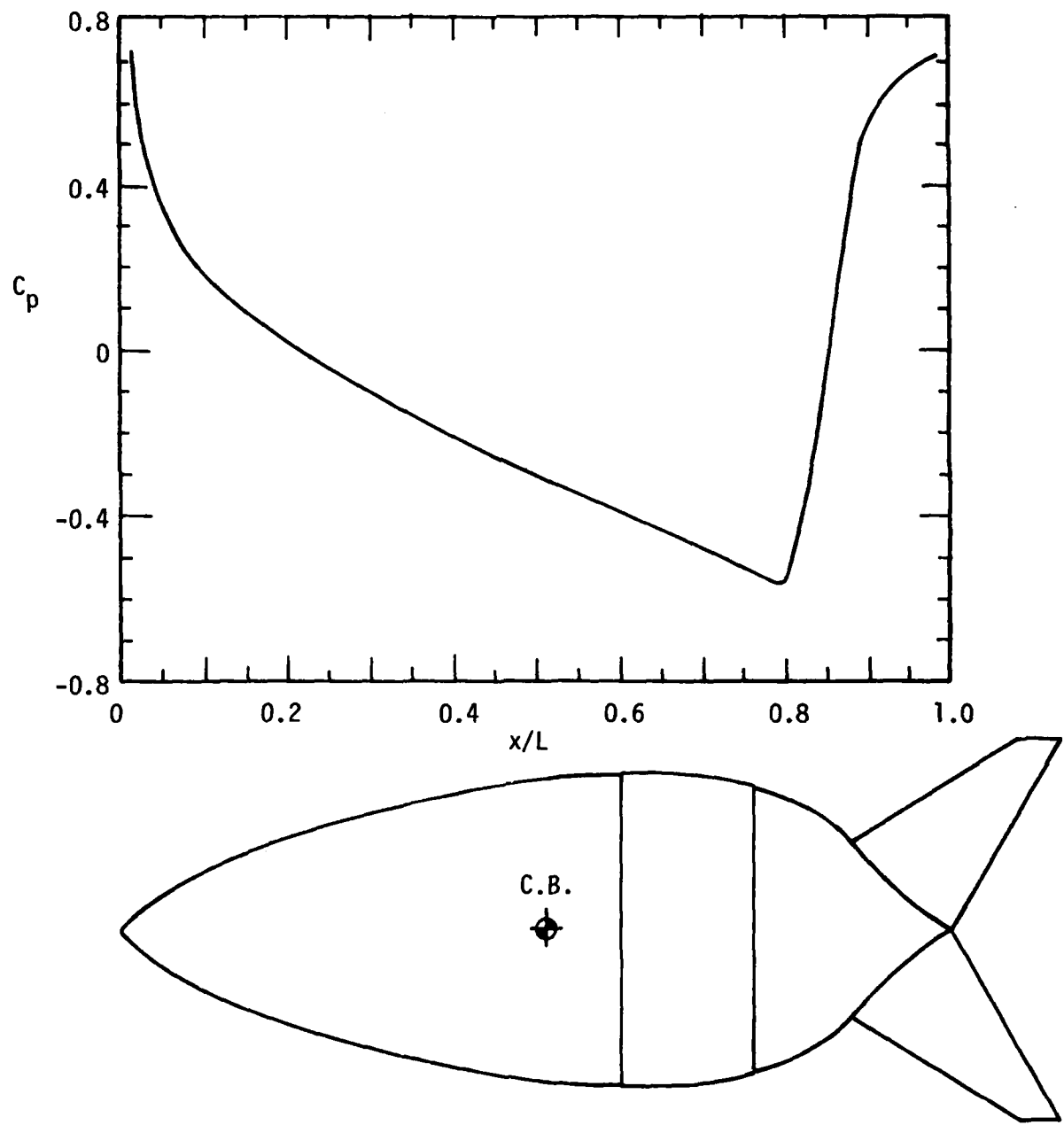
	NOSE	CENTER OF BUOYANCY	INTAKE	AFTER- BODY LIP	FIN LEADING EDGE	TERMINUS
STATION (INCHES)	0.00	25.06	28.68	37.50	48.77	61.30
DIAMETER (INCHES)	0.00	17.01	17.25	14.78	3.78	0.00
AREA (SQ. INCHES)	RADIAL		3.72	2.43		
VOLUME (CF)	3.53					

FIGURE 2-6. HDV CONFIGURATION SPECIFICATION



	NOSE	CENTER OF BUOYANCY	INTAKE	AFTER-BODY LIP	FIN LEADING EDGE	TERMINUS
STATION (INCHES)	0.00	24.70	28.25	37.50	41.30	46.70
DIAMETER (INCHES)	0.00	16.92	17.02	14.24	7.63	0.00
AREA (SQ. INCHES)		SUBMERGED		4.48	3.35	
VOLUME (CF)		3.50				

FIGURE 2-7. IRV CONFIGURATION SPECIFICATION



	NOSE	CENTER OF BUOYANCY	INTAKE	AFTER-BODY LIP	FIN LEADING EDGE	TERMINUS
STATION (INCHES)	0.00	24.70	28.20	35.40	40.70	46.70
DIAMETER (INCHES)	0.00	16.92	17.24	15.76	8.90	0.00
AREA (SQ. INCHES)	SEMI-FLUSH		12.22	8.50		
	AXIAL		12.42	VOLUME = 3.50 cf.		

FIGURE 2-8. ATV CONFIGURATION SPECIFICATION

separate and independent evaluation of their drag characteristics. Thus a unique analytical model is required. The thrust/drag components are identified in Figure 2-9. Since each drag component is affected in some way by the BLC/propulsion process, their individual values will vary with the dynamic situation (i.e., accelerating, decelerating, or steady speed). Primary interest is for the case of self-propulsion at constant vehicle velocity. For this case an axial force balance may be written expressing the thrust required for self-propulsion as the sum of the thrust-dependent drag components.

2.2.2.1 Forebody Drag

As discussed in Section 2.1.4, the forebody drag is broken into two components. Part or all of the forebody boundary layer is ingested by the propulsor intake and that momentum deficit is treated as a propulsor intake loss. Any residual portion of the forebody boundary layer going past the intake "spills over" onto the shroud and is dealt with in the evaluation of the shroud drag. Thus the axial force balance includes only part of the forebody drag (spillage) and the jet thrust does not have to compensate for the ingested momentum deficit. If a value of total drag coefficient must be defined for comparison, it will represent the sum of the momentum deficit ingested by the intake and the thrust provided by the BLC-jet. Forebody boundary layer characteristics, evaluated by an axisymmetric computer code¹⁴ are provided in Table 2-1 for all test configurations.

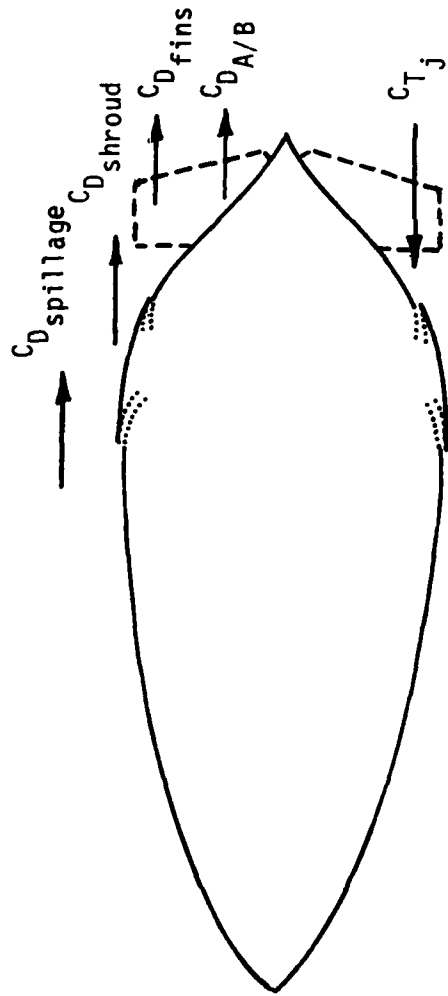
2.2.2.2 Spillage Drag

Spillage drag is defined as the portion of the momentum deficit, caused by forebody friction, that does not get ingested by the intake. The spillage drag will obviously be a function of the forebody Reynolds number, boundary layer growth, and the propulsor mass flow rate. Typical spillage drag predictions are shown for the test configurations in Figure 2-10. The zero-flow-rate spillage drag is equal, obviously to the forebody momentum deficit.

2.2.2.3 Shroud Drag

The shroud drag is generated by the viscous fluid action on the centerbody shroud surface of the vehicle and is dependent on the amount of spillage

AXIAL FORCE DIAGRAM



FORE BODY DRAG

$$C_{D_{F/B}} = C_{D_{in}} + C_{D_{Spill}}$$

AFT-BODY DRAG

$$C_{D_{1ip}} = C_{D_{Spill}} + C_{D_{shroud}}$$

$$C_{D_{aft-body}} = C_{D_{1ip}} + C_{D_{A/B}} + C_{D_{fins}}$$

AXIAL FORCE BALANCE

$$C_{\text{net}} = C_{T_j} - C_{D_{Spill}} - C_{D_{shroud}} - C_{D_{A/B}} - C_{D_{fins}}$$

BALANCE

$$C_{\text{net}} = C_{\text{bal}} - C_{\text{strut}} - C_{\text{bellows}}$$

FIGURE 2-9 THRUST/DRAG COMPONENTS AND NOMENCLATURE

TABLE 2-1. TEST CONDITIONS AND FORE BODY BOUNDARY LAYER CHARACTERISTICS

		INLET STATION					
CONFIGURATION	LAMINAR/ TURBULENT	q_{∞} (psf)	$Re_{\infty} 1/3$	Re_L	θ (in)	\hat{A}	POWER LAW EXPONENT
Advanced Tactical Vehicle (ATV)		20.7	1.18×10^6	3.02×10^6	0.030	1.361	5.5
		31.2	1.49×10^6	3.83×10^6	0.029	1.351	5.7
	TURB.	52.2	1.83×10^6	4.69×10^6	0.028	1.343	5.8
		83.2	2.32×10^6	5.95×10^6	0.027	1.334	6.0
Hydro Demonstration Vehicle (HDV)	LAM.	52.2	1.84×10^6	6.17×10^6	0.0066	2.38	-
		83.2	2.33×10^6	7.82×10^6	0.0060	2.38	-
Improved Range Vehicle (IRV)	LAM.	83.2	2.32×10^6	5.95×10^6	0.0060	2.38	-

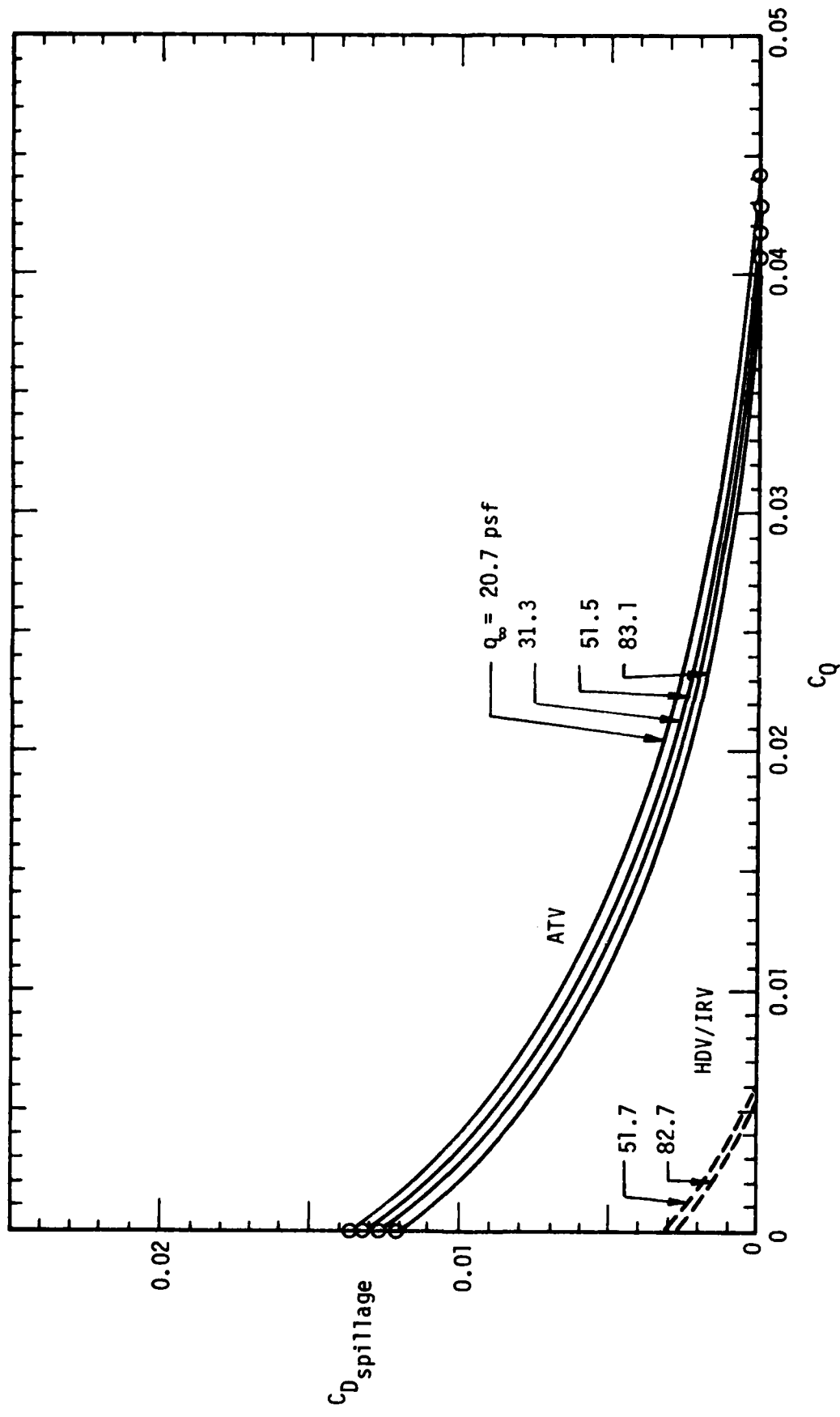


FIGURE 2-10. SPILLAGE DRAG COMPONENTS

momentum deficit. If the entire forebody boundary layer is ingested into the inlet (such as is the case for a laminar boundary layer) a new boundary layer initiates at the shroud leading edge and the shroud drag is simply the momentum deficit existing at the shroud trailing edge (or BLC jet exit). On the other hand, if a portion of the forebody boundary layer 'spills over,' the shroud boundary layer growth is influenced by a reduction in the local edge velocity generated by the boundary layer wake that washes this surface. Computationally, this phenomenon can be treated simply by considering boundary layer growth as originating ahead of the intake location. That is, a fictitious starting length experiencing the body pressure distribution in that region is provided that generates a momentum deficit at the shroud leading edge station equal to the spillage momentum deficit. The shroud drag coefficient is then simply the momentum deficit difference between that exiting at the shroud trailing edge and the spillage deficit. Since the spillage drag is flow rate dependent, the shroud drag is thus also dependent upon the ingested flow rate. Predicted shroud drag characteristics are shown in Figure 2-11 for all test configurations. As indicated the shroud drag asymptotically approaches a constant value as the flow rate approaches that needed for complete ingestion of the forebody viscous momentum deficit.

2.2.2.4 Afterbody Drag

The drag characteristics of an afterbody with integrated BLC-jet propulsor can be effectively evaluated by considering the fundamental flow behavior over the afterbody, including blowing jet effects and mixing in a strong adverse pressure gradient. Thrust may be added by any jet regardless of how or where it is introduced. The propulsive efficiency of that thrust is however strongly dependent upon how the jet mixes with the external flow. Likewise, the afterbody drag will be a function of the nature of the jet, and how it is introduced into and mixed with the flow. If fins are present in the interaction region they also can affect the basic flow field and possibly introduce interference drag effects not accounted for in a simple summation.

On a propulsive afterbody, real fluid mixing (momentum exchange) occurs between the shroud momentum deficit and the BLC-propulsive jet, that is in turn continuously eroded by shear forces near the wall in the downstream

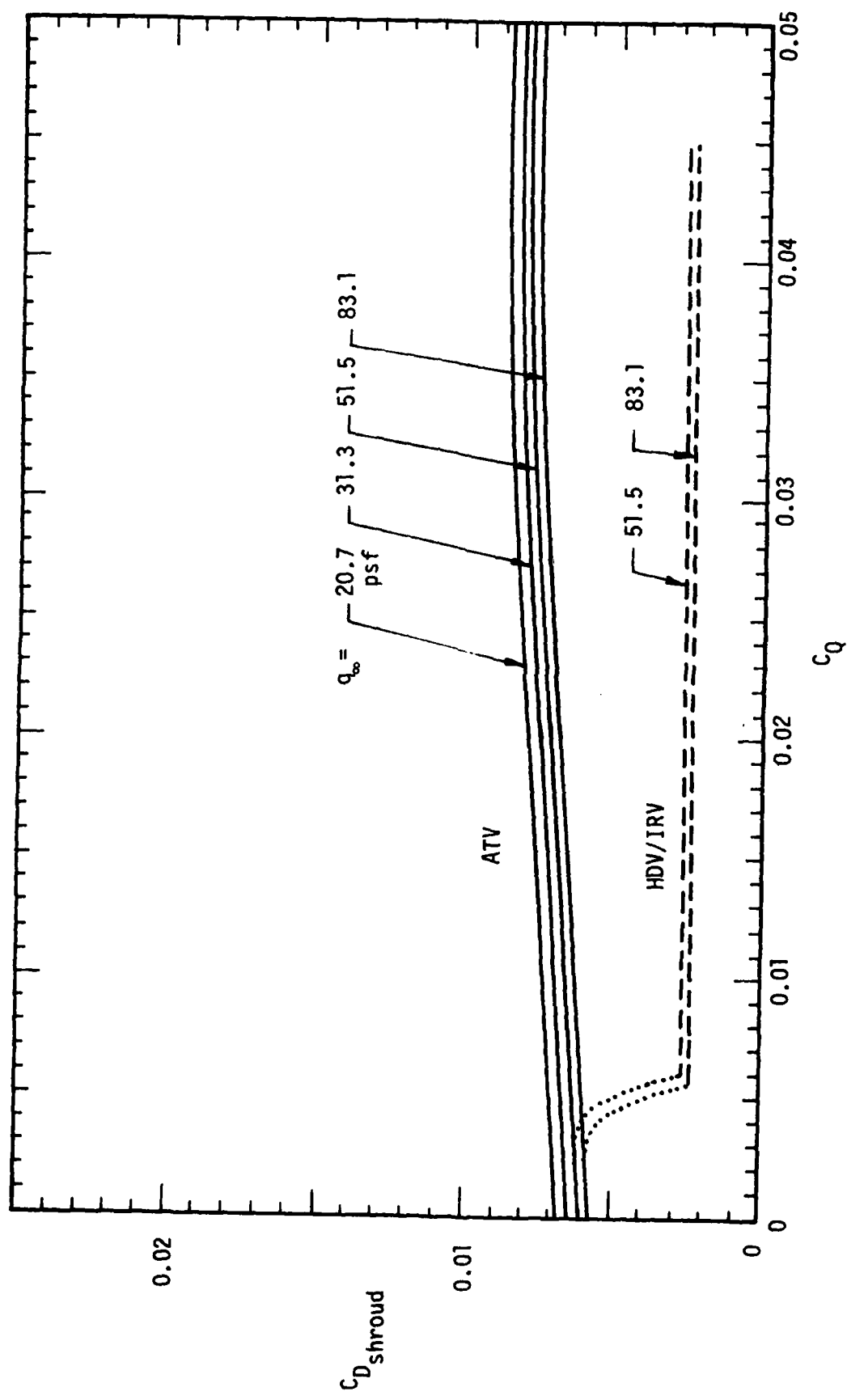


FIGURE 2-11. SHROUD DRAG COMPONENTS

region. The calculation of wall jet energization in the adverse pressure gradient for an axisymmetric body contour requires a sophisticated computational approach, usually of a finite difference type. The fundamental mixing phenomena, particularly for a laminar-flow shroud (such as on the HDV) can be modeled by the method of Gartshore and Newman.¹⁵ Axisymmetric effects can be treated by applying the Mangler transformation¹⁶ to the afterbody pressure distribution. Other boundary layer calculation procedures, such as that developed by Miner and Lewis,¹⁷ may be beneficial in treating the jet/boundary layer mixing process. However, no comprehensive analytical model has yet been developed that completely predicts the drag characteristics of such a propulsive afterbody, especially for thick turbulent boundary layers. The most accurate approach thus far has been an empirical correlation of existing data gathered from wind tunnel tests and free-running range tests of the HDV. This empirical curve is shown in Figure 2-12. It was derived by subtracting measured or predicted values of the lip momentum deficit and fin drag from total thrust measurements of the vehicle. This is a key feature of the BLC-propulsive jet afterbody. Since energization of the lip boundary layer occurs on the body, the jet thrust is a function of the lip momentum deficit and not of a drag coefficient that would be obtained by expansion of that deficit into the wake (see also Section 2.2.6). For contrast, the afterbody drag characteristics predicted by a coherent, non-mixed jet as cited in reference 10 are also shown in Figure 2-12.

Expected HDV test conditions from the range test program and design (or set-up) conditions for the IRV and ATV in the wind tunnel are also shown. That is to say that the HDV is expected to be selfpropelled (zero net axial force) at an afterbody drag coefficient near 0.008 (as indicated by range test data) and the IRV and ATV jet exit areas were selected to equilibrate at a $C_D A/B = 0.003$. The procedure followed to achieve this condition is discussed in Sections 2.2.3 and 2.2.4.

2.2.2.5 Fin Drag

The drag of control fins or lifting surfaces (for maneuvering vehicles) is normally treated as a separate increment determined from wetted area exposed to freestream velocity. The present analysis considers that the fins experience the flow field defined by the potential flow solution over the afterbody, as illustrated in Figure 2-13.

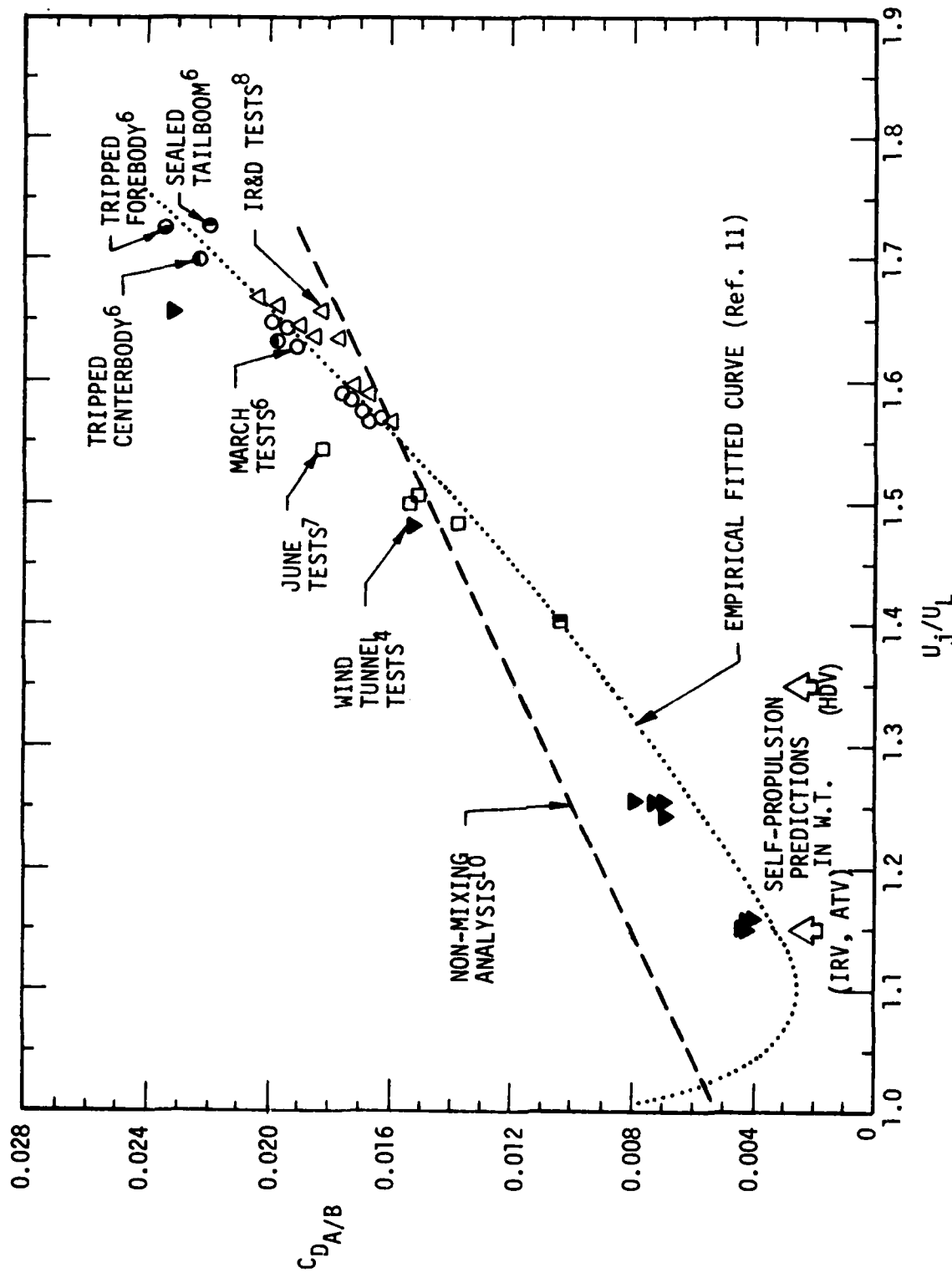


FIGURE 2-12. AFTERBODY DRAG CHARACTERISTICS

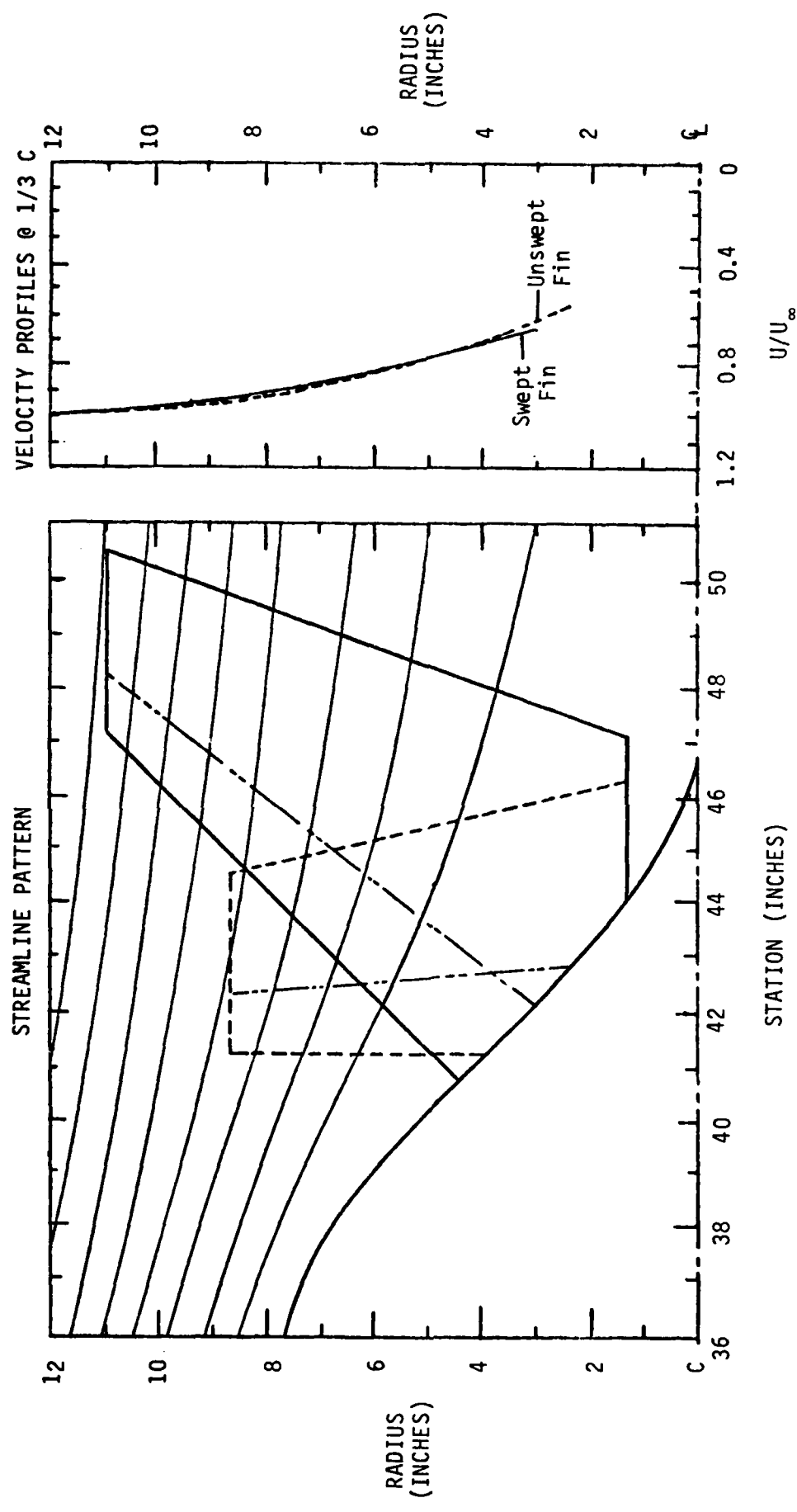


FIGURE 2-13. FIN FLOW FIELD FOR PROPELLIVE AFTERBODY

The velocity over the fins varies such that the dynamic pressure, q , increases outward along the span. There is also a slight increase in q across the chord of the fins, but for the purpose of analysis, the q at one-third chord is assumed at each spanwise station. Depending on the location of the fins there will also be some angularity of the flow which affects the effective sweep angle.

The fin drag may be determined from

$$D = N \int_{y_{\text{root}}}^{y_{\text{tip}}} q C_{d_0} c dy \quad (2-1)$$

where q and c (if tapered) are functions of distance from the body; C_{d_0} depends on Reynolds number, airfoil section, and sweep angle; and N is the number of fins. The drag coefficient based on volume is then

$$C_{D_{\text{fins}}} = \frac{N}{V^{2/3}} \int_{y_{\text{root}}}^{y_{\text{tip}}} \frac{q}{q_{\infty}} C_{d_0} c dy \quad (2-2)$$

The calculated values for the different fin sets were 0.0017 for the HDV and 0.0031 and 0.0012 for the swept and unswept ATV fins, respectively, scaled to the appropriate Reynolds number for $q_{\infty} = 30$ psf. A nominal 15 percent penalty was added to account for interference effects.

2.2.3 Total Aft-body Drag/Thrust Requirements

A force balance is used to determine BLC-jet thrust requirements based on the drag constituents described above. The total aft-body drag includes spillage, shroud, afterbody, and fin drag. For self-propulsion,

$$C_{T_j} = C_{D_{\text{spillage}}} + C_{D_{\text{shroud}}} + C_{D_{\text{afterbody}}} + C_{D_{\text{fins}}} \quad (2-3)$$

Since both the spillage and shroud drag are intake flow-rate dependent, the afterbody drag characteristics are also formulated in terms of the propulsor flow rate. The flow coefficient, based on BLC-jet exit quantities, may be written as

$$C_Q = \lambda_v \frac{A_j}{V^{2/3}} \frac{u_j}{U_L} \frac{U_L}{U_{\infty}} \quad (2-4)$$

where λ_y is a viscous blockage factor that relates 'core-type' inviscid velocity (u_j) to flow rate and accounts for viscous internal-flow nozzle losses, etc. This factor is required since the empirical afterbody drag characteristics are primarily dependent upon the jet exit 'core' velocity (ratioed to local freestream velocity as in Figure 2-12). A value of $\lambda_y = 0.96$, determined from wind tunnel data, has been used for the Reynolds number range for these tests.

The drag constituents and total aft-body drag characteristics for the ATV configuration at $q_\infty = 30$ psf are provided in Figure 2-14. A BLC-jet exit area of 8.50 square inches and the potential-flow lip velocity ratio (U_L/U_∞) of 1.25 were used to define afterbody drag dependence on flow rate and define the thrust-equal-drag condition.

The thrust for a jet is expressed by

$$T = \dot{m} (\bar{V}_j - U_\infty) \quad (2-5)$$

where \bar{V}_j is the jet exit velocity expanded to freestream static pressure. A thrust coefficient can be defined as

$$C_T = \frac{T}{q_\infty V^{2/3}} = \frac{\dot{m}(\bar{V}_j - U_\infty)}{q_\infty V^{2/3}} \quad (2-6)$$

With appropriate substitutions and manipulations this leads to

$$C_T = 2C_Q \sqrt{\left[\frac{V^{2/3} C_Q}{A_j} \right]^2 + C_{p_e}^{-1}} \quad (2-7)$$

where C_{p_e} is the body static pressure coefficient at the jet exit and A_j is the jet area.

The ATV self-propelled condition was conservatively selected for a C_Q slightly less than that at the aftbody drag minimum (i.e., the BLC-jet exit area was chosen for near, but slightly above, minimum thrust), as shown in Figure 2-14. Picking a smaller jet exit area shifts the afterbody drag curve to the left (lower C_Q 's) with self-propulsion moving to the 'front side' of the drag curve where the total drag increases rapidly. This was indeed the condition that occurred in the HDV vehicle range tests where, due to off-design inlet performance, the vehicle could never accelerate to the design condition of u_j/U_L at the appropriate C_Q .

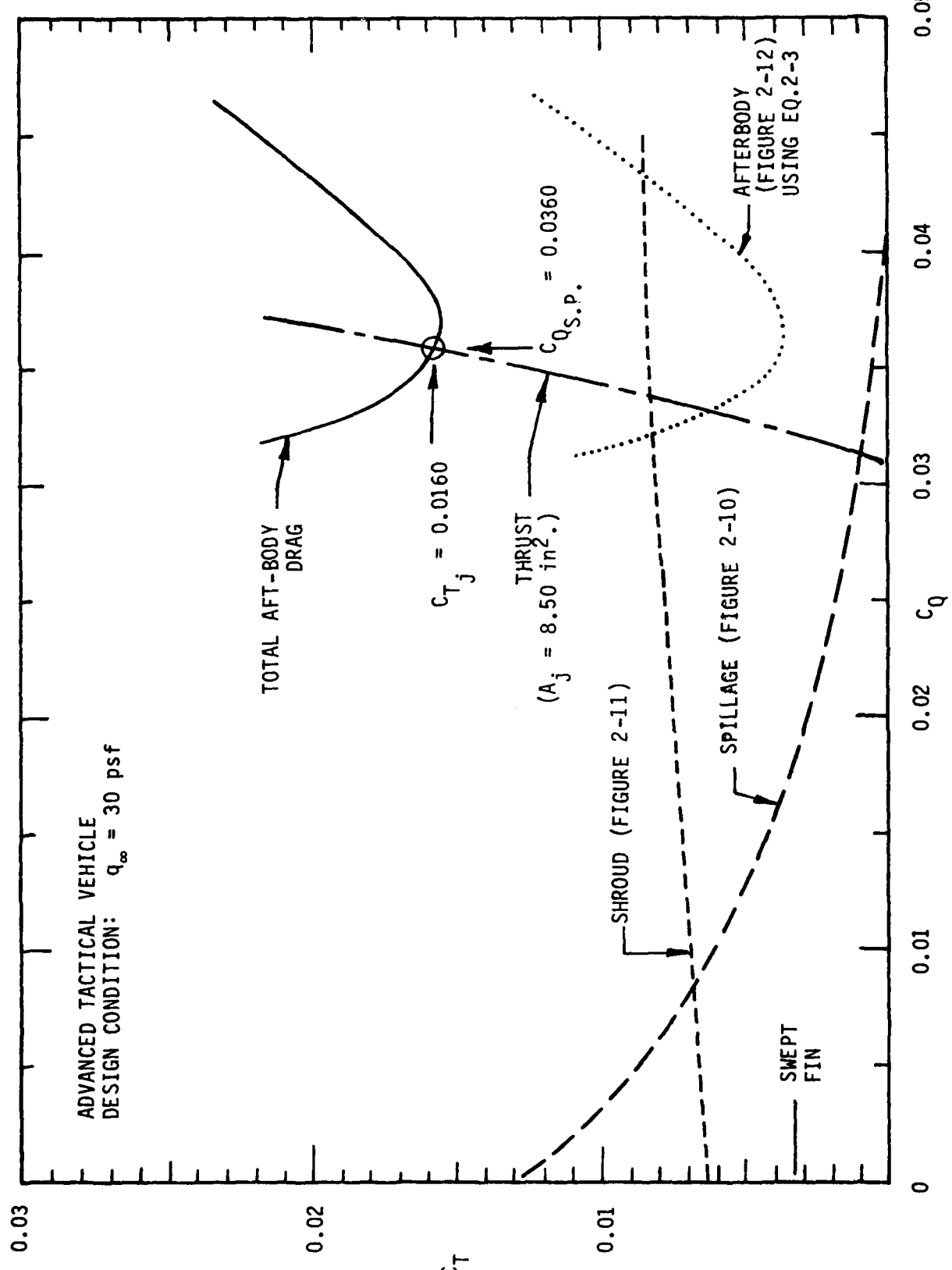


FIGURE 2-14. TOTAL AFT-BODY DRAG CHARACTERISTICS

2.2.4 Propulsor Power

A key performance parameter for all vehicles is the propulsor power requirement. For a configuration with a self-contained power system (for instance a non-air-breathing propulsor) propulsor power is the key quantity necessary to characterize the vehicle's performance. The power requirements needed to generate the thrust necessary to overcome the vehicle drag must be evaluated. The propulsor power requirements for the BLC-jet propulsive afterbody can be readily determined by considering the fluid power characteristics of the intake and jet exhaust flows. The fluid power, with respect to free-stream conditions, is given as

$$P = \int u(H - H_{\infty}) dA \quad (2-8)$$

with the integration performed both at the inlet and the BLC-jet exit. The total fluid power coefficient is then given as

$$C_{P_T} = \frac{[P_j - P_i]}{q_{\infty} U_{\infty} V^{2/3}} \quad (2-9)$$

2.2.4.1 Inlet Power Accounting

The flow into the inlet will naturally have a non-uniform total pressure distribution due to the forebody viscous losses. This can be easily measured in the inlet in wind tunnel tests. There might also be a static pressure distribution due to turning that is not so easily measured, thus direct determination of the power deficit in the inlet is difficult. However, if the total pressure recovery in the inlet is good, the total pressure distribution will be very close to that in the forebody boundary layer where the transverse static pressure gradient is small. Then the power deficit can be determined on the forebody near the inlet (station 1) for the amount of flow that is ingested in the inlet.

A power-law expression for the turbulent forebody boundary layer can be written as

$$\frac{u}{U_1} = \left(\frac{y}{\delta_1} \right)^{\frac{1}{n}} \quad (2-10)$$

A stream function for the flow can be defined as

$$\psi = 2 \pi r_1 \int_0^y u dy \quad (2-11)$$

which gives the volume flow rate contained between the wall and the streamline at any y . The total pressure deficit $(H - H_\infty)_1$ can be expressed for the power-law profile by

$$(H - H_\infty)_1 = \frac{1}{2} \rho U_1^2 \left[\left(\frac{y}{\delta_1} \right)^{2/n} - 1 \right] \quad (2-12)$$

The power deficit coefficient for the inlet is defined as

$$C_{P_i} = \frac{2\pi r_1 \int_0^{\bar{y}_1} u_1 (H - H_\infty)_1 dy}{\sqrt[2/3]{q_\infty U_\infty}} \quad (2-13)$$

The upper integral limit \bar{y}_1 will be determined by flow rate requirements. A flow coefficient may be expressed as

$$C_Q = \frac{0}{\sqrt[2/3]{U_\infty}} = \frac{2\pi r_1 \int_0^{\bar{y}_1} u_1 dy}{\sqrt[2/3]{U_\infty}} = \frac{2\pi r_1 \delta_1}{\sqrt[2/3]{U_\infty}} \frac{n}{n+1} \frac{U_1}{U_\infty} \left(\frac{\bar{y}}{\delta} \right)_1^{\frac{n+1}{n}} \quad (2-14)$$

Once the required inlet flow rate is specified the \bar{y} value for the capture boundary streamline can be determined from (2-14) with δ , r , U_1 , and n being determined for the forebody flow.

Integration of (2-13) then leads to

$$C_{P_i} = \frac{2\pi r_1 \delta_1}{\sqrt[2/3]{U_\infty}} \left(\frac{U_1}{U_\infty} \right)^3 \left[\frac{n}{n+3} \left(\frac{\bar{y}}{\delta} \right)_1^{\frac{n+3}{n}} - \frac{n}{n+1} \left(\frac{\bar{y}}{\delta} \right)_1^{\frac{n+1}{n}} \right] \quad (2-15)$$

Predictions for the three test configurations are given in Figure 2-15.

2.2.4.2 BLC Jet Power

As was done for the inlet, it is desireable to relate BLC jet power to the flow coefficient since this quantity is accurately measured in a wind tunnel test. The jet power excess is expressed as

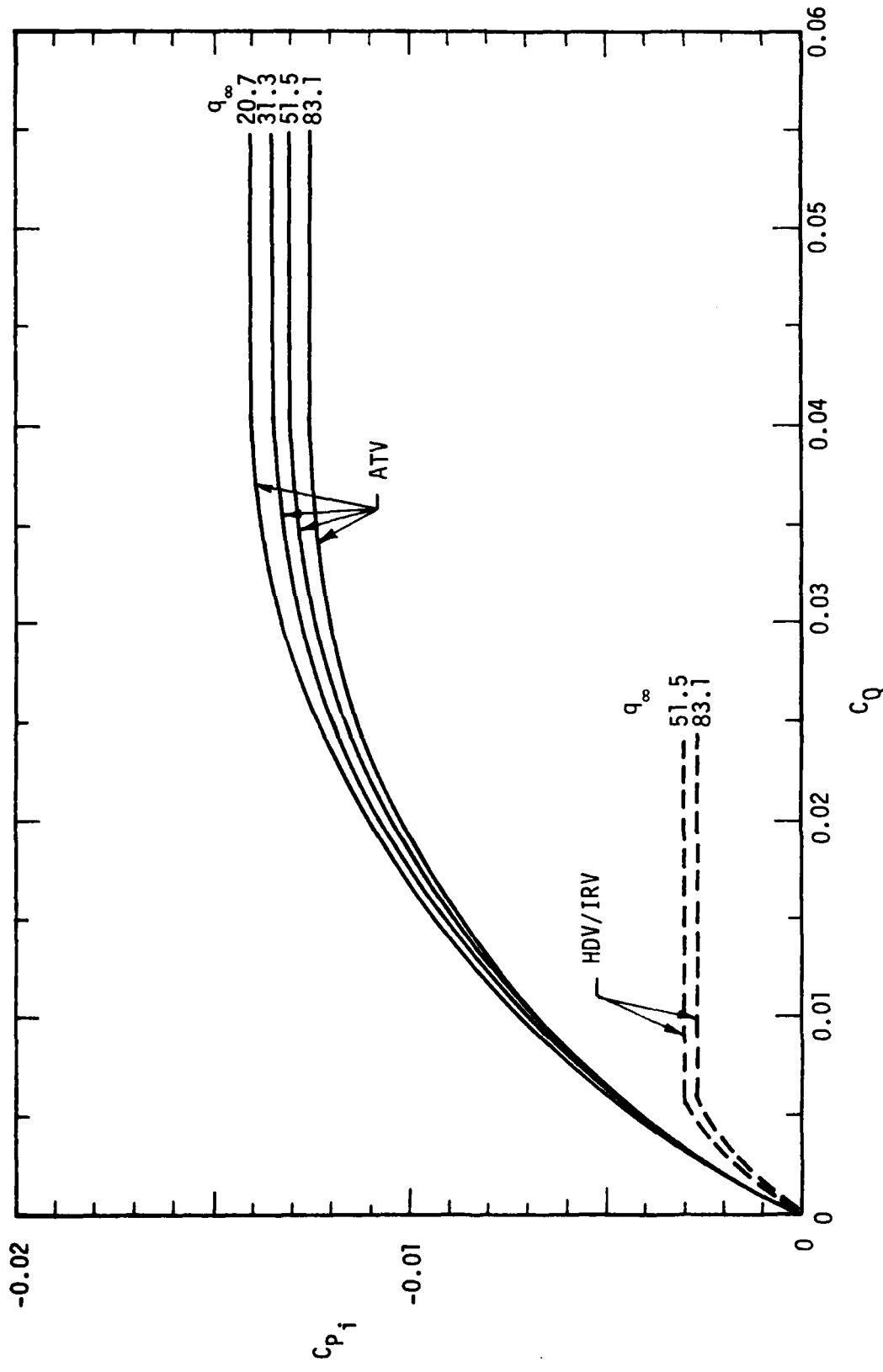


FIGURE 2-15. INTAKE POWER COEFFICIENT

$$C_{P_j} = \frac{2\pi r_1 \int_0^{h_j} u(H-H_\infty) dy}{V^{2/3} q_\infty U_\infty} \quad (2-16)$$

where h_j is the height of the jet exit.

Further development leads to

$$C_{P_j} = C_Q \left[\left(\frac{V^{2/3}}{A_j} C_Q \right)^2 - (1-C_{P_e}) \right] \quad (2-17)$$

It should be noted that equation (2-17) is exact only for a jet with uniform exit velocity and static pressure. It is to be expected that viscous effects in the BLC channel and flow curvature, both in the BLC channel and the external flow, will likely cause both to be non-uniform to some degree, and this is not easily predictable. Intuitively, one would expect the core region of the jet to be at higher velocity than \bar{u} and the edges of the jet to have a velocity distribution representative of the wall boundary layers formed in the BLC channel. Furthermore, the radial static pressure gradients due to curvature will likely cause a skewness in the jet velocity profile with the velocity being slowed next to the body and increased in the outer portion of the jet. Equation (2-16) shows that jet power will be proportional to a cubic function of jet velocity integrated over the exit slot height. Consequently a non-uniform and skewed jet velocity profile might represent a significantly higher power level than that predicted by equation (2-17) for a given flow rate. For these reasons, although more laborious, equation (2-16) was used in all data reduction.

The predicted thrust and power characteristics for all test configurations are shown in Figures 2-16 and 2-17. The flow rate required for self-propulsion is determined from thrust levels derived from the drag model at design point conditions. From these flow rate values the jet power levels for self-propulsion can be evaluated. The steep slopes of the curves illustrate the sensitivity of power requirements to trade-off in jet velocity and flow rate at the same thrust level.

2.2.5 Stability and Control Surface Effectiveness

As described in Section 2.2.2.4, control surfaces attached to a propulsive afterbody will experience a flow field somewhat different than that of free-stream conditions. Specifically, the local velocity near the root of the

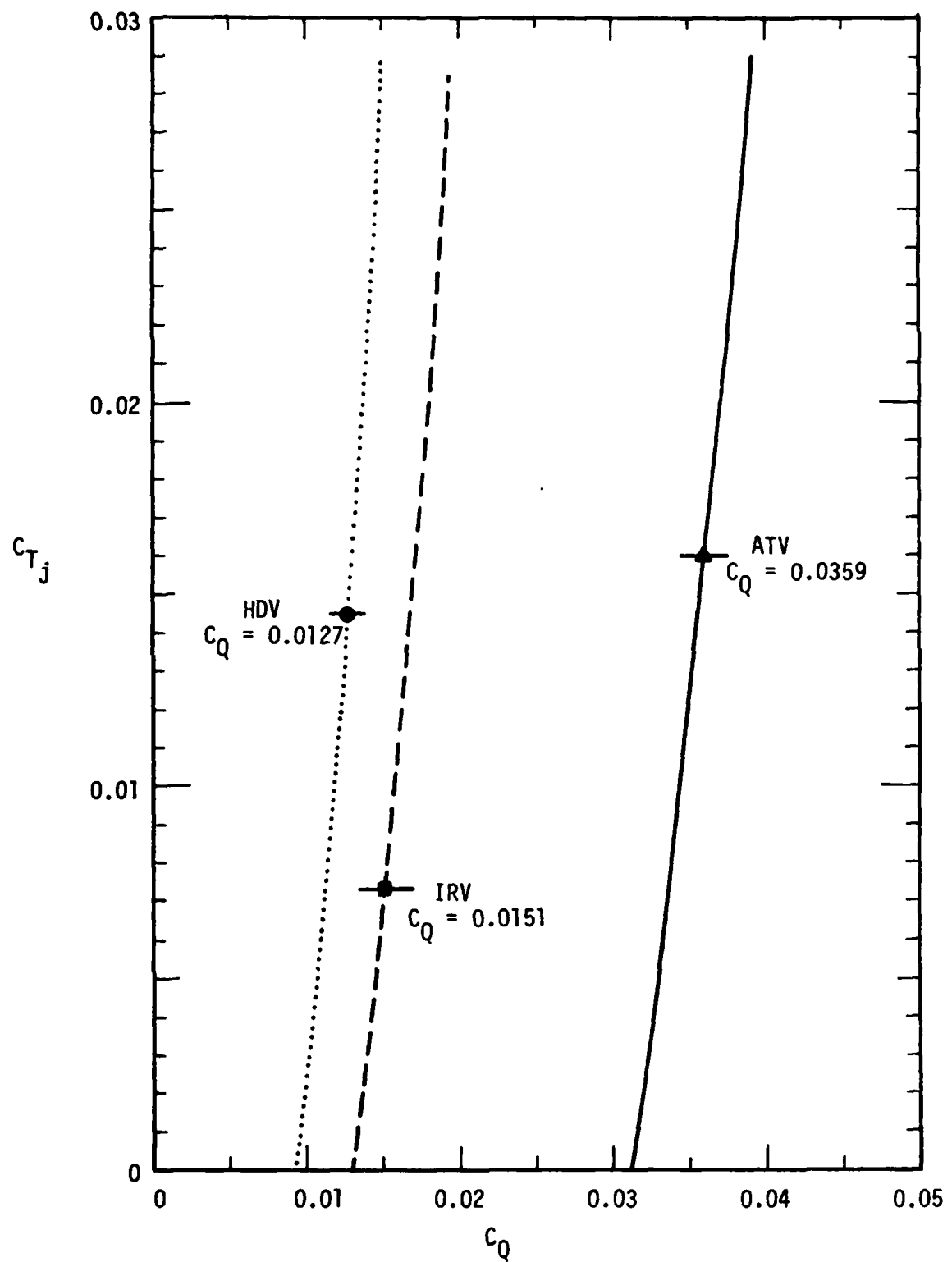


FIGURE 2-16. BLC JET THRUST COEFFICIENTS-THEORETICAL

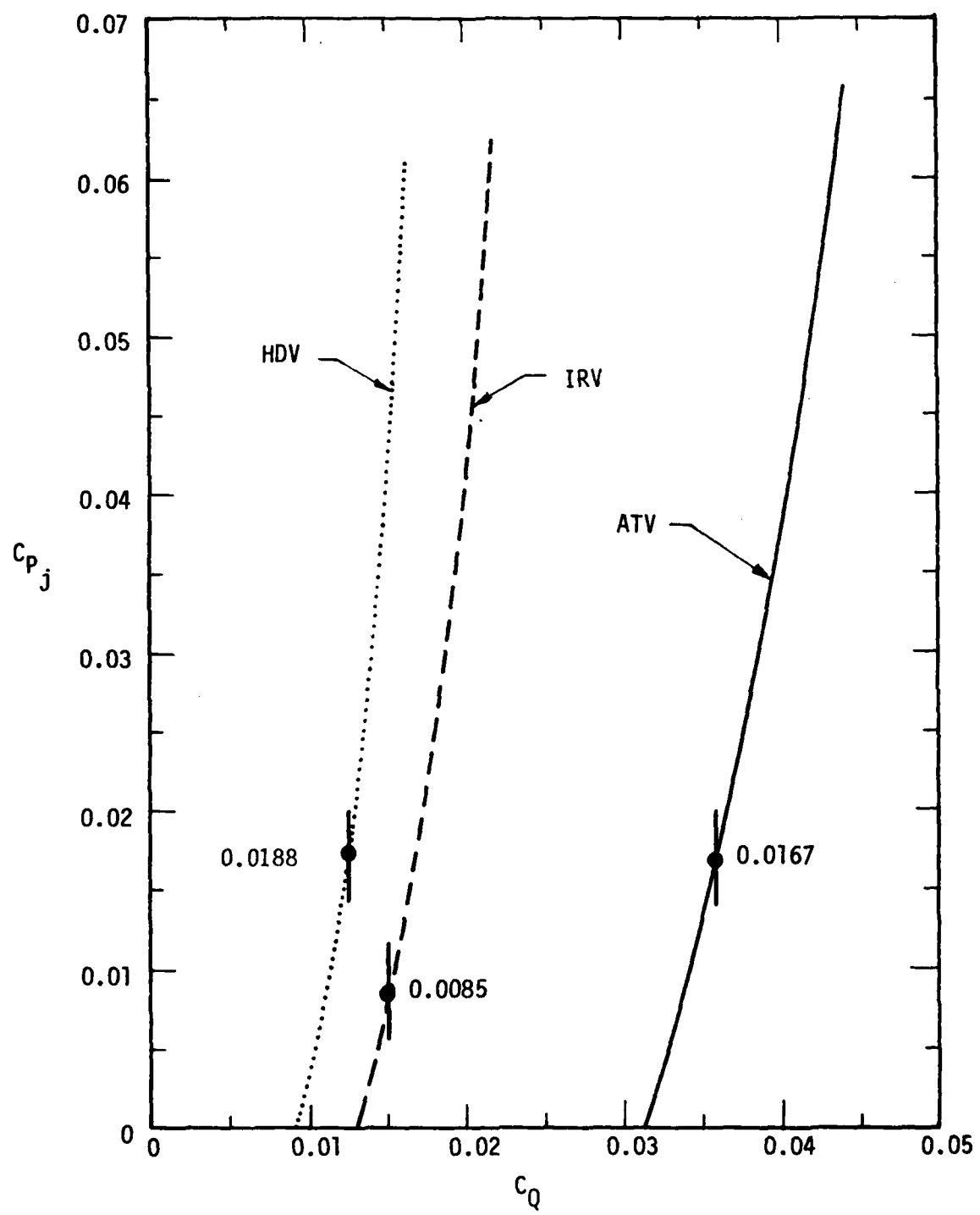


FIGURE 2-17. BLC JET POWER COEFFICIENTS-THEORETICAL

surfaces may be higher than freestream due to the BLC/propulsive jet, while outboard the velocity will be less than freestream, but increasing toward the tip, and the local streamlines will be also inclined, as predicted by a potential flow solution. Since this situation is somewhat unconventional, any exact prediction methodology will be strongly dependent on afterbody flow performance. In a conservative manner, the analytical evaluation of control surface effectiveness has been related to empirical characteristics catalogued by Hoerner¹⁸ for bodies not so blunt and without any BLC. This approach takes into account the behavior of low aspect ratio lifting surfaces on the aft end of axisymmetric bodies based on freestream flow conditions. The empirical correlations were further refined by adjusting for the distribution of flow-field dynamic pressure in the same manner as done in the drag analysis. Static stability predictions were based on the resulting lifting characteristics and a presumed neutral point determination in early wind tunnel tests of the HDV.⁸

2.2.6 Vehicle Performance Predictions

Design-point test conditions were selected for each of the vehicles as a basis for specifying intake and BLC-jet flow areas. As discussed previously, the HDV range vehicle hardware was tested in the wind tunnel at maximum dynamic head ($q_{\infty} = 80$ psf) that corresponded to the low-speed range test Reynolds number. The improved range vehicle was likewise designed for a $q_{\infty} = 80$ psf. The ATV design point was selected at a $q_{\infty} = 30$ psf which represented a mid-point in the $1 - 2 \times 10^6$ Reynolds number range.

Performance predictions for each of the test configurations were evaluated at the selected design-point test conditions. The analytical methodology, as discussed in Figure 2-14, was used to determine thrust and flow coefficients for the mixing model. A non-mixing analytical model, formulated in reference 10, can also be used to determine expected performance levels. The non-mixing model differs in two respects; 1) the afterbody drag characteristics are significantly different for low jet-to-lip velocity ratios (Figure 2-12), and 2) the jet lip momentum deficit is expanded un-mixed to freestream pressure in the wake where energization hypothetically occurs.

The wake energization/non-mixing assumption can be readily treated by using a Squire-Young correction,¹⁹ of the form

$$C_{D_{lip}} = \left(\frac{4\pi r_{lip} \theta_{lip}}{V^{2/3}} \right) \left(\frac{U_{lip}}{U_{\infty}} \right)^{\frac{H+5}{2}} \quad (\text{non-mixed}) \quad (2-18)$$

which may be rearranged to

$$C_{D_{lip}} = \left(\frac{4\pi r_{lip} \theta_{lip}}{V^{2/3}} \right) \left(\frac{U_{lip}}{U_{\infty}} \right)^2 \cdot \left[\left(\frac{U_{lip}}{U_{\infty}} \right)^{\frac{H+1}{2}} \right] \quad (\text{non-mixed}) \quad (2-19)$$

which is simply the lip momentum deficit multiplied by the lip velocity ratio to an exponent dependent on shape factor. At the lip the shape factor is about 1.35 at these test conditions. For $U_{lip}/U_{\infty} = 1.25$, the bracketed quantity is 1.30. Thus the drag coefficient at the lip (including both spillage and shroud drag) $C_{D_{lip}}$ must be multiplied by 1.30 to account for expansion into the wake prior to energization.

Self-propulsion performance predictions, for both the mixing and non-mixing analytical models, for all three vehicle configurations at design-point test conditions are provided in Table 2-2. Inspection of this table reveals two important aspects of the BLC-jet propulsive afterbody. First, a comparison of the ATV and IRV indicates that a substantial reduction in fluid power requirements occurs for a low-drag afterbody mated with a laminar-flow forebody, even at moderately low Reynolds numbers. Secondly, the effect of efficient on-the-body BLC mixing is predicted to substantially reduce vehicle propulsor power (37 percent for the ATV, 70 percent on the laminar-flow IRV) as compared to the non-mixing model. These design-point predictions will be compared with the test results in Section 5.

TABLE 2-2 VEHICLE DESIGN-POINT PERFORMANCE PREDICTIONS

VEHICLE CONFIGURATION	q_{∞} (psf)	C_Q	C_{T_J}	C_{P_1}	C_{P_J}	C_{PT}
ATV - Swept Fins	30	Mixing	0.0160	0.0133	0.0175	0.0308
		Non-Mixing	.0247	.0134	.0288	.0422
HDV-Tailboom Fins	80	Mixing	0.0145	0.0027	0.0186	0.0215
		Non-Mixing	.0184	.0027	.0245	.0272
IRD-Untswept Fins	80	Mixing	0.0074	0.0027	0.0065	0.0112
		Non-Mixing	.0138	.0027	.0163	.0190

3.0 TEST PROGRAM

The objectives set forth for the wind tunnel test program required three basic model configurations to validate the performance and evaluate the applications for the integrated afterbody propulsor concept, with the stipulation that as much use as possible be made of existing hardware from the HDV program.

The test program was designed in two phases. The first phase was conducted in the Vought Corporation's Low Speed Wind Tunnel and included tests of all three basic configurations. The second phase was conducted by the David Taylor Naval Ship Research and Development Center (DTNSRDC) in their Subsonic Wind Tunnel Facility and involved only the ATV configuration. Descriptions of the model configurations follow.

3.1 MODEL CONFIGURATIONS

3.1.1 Hydrodynamic Demonstration Vehicle (HDV)

The HDV configuration was the same as that used in the last series of free-running in-water range tests in the Navy-sponsored HDV Program.⁷ This configuration is referred to in publications as the HDV with modified afterbody. The radial inlet and jet exit areas were left the same but the tail boom exhaust was sealed and an extended terminus was installed. This exactly matches the test configuration of range run No. 27 reported in reference 7. The HDV was tested in the wind tunnel with and without fins to explicitly determine fin drag, as this was one of the issues in the Navy evaluation of the HDV performance. The HDV model is shown mounted in the wind tunnel in Figure 3-1.

3.1.2 Improved Range Vehicle (IRV)

The IRV configuration represents an approach to an optimized high-speed vehicle of the HDV type. The laminar flow forebody and centerbody shroud are retained and the afterbody has been brought to closure without a tail boom. The fins were sized to maintain controllability and minimum drag but the close-coupled location on the afterbody results in a statically unstable configuration. A new inlet, described as a submerged inlet, was designed for improved

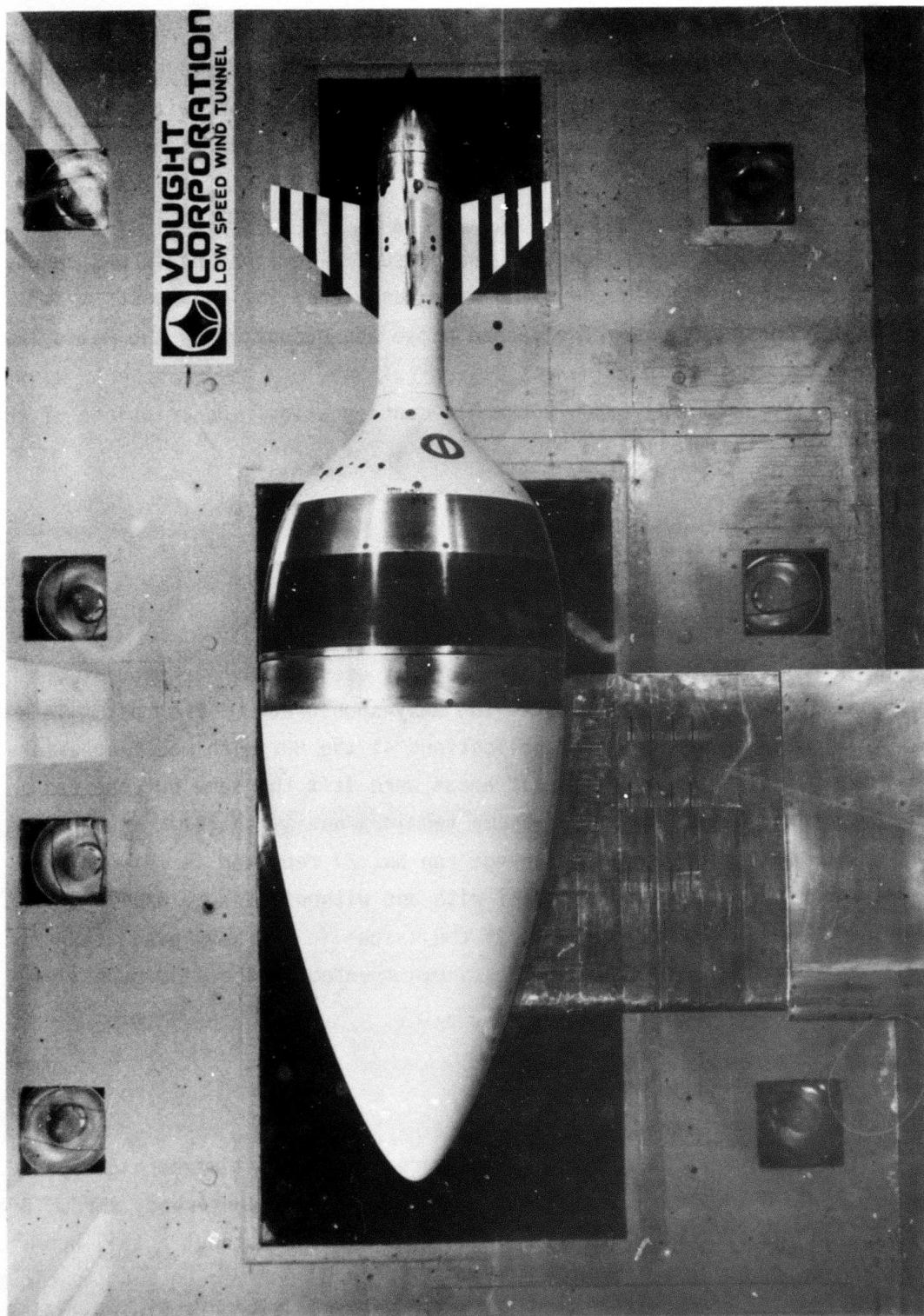


FIGURE 3-1 HDV INSTALLATION IN WIND TUNNEL

performance. Specifically, the inlet area was enlarged to increase flow rate and the curvature was changed to reduce the high velocity spike at the entrance and to reduce the diffusion rate and diffusion ratio through the intake. The jet exit area was increased to reduce the jet exit velocity and match it better to the local external velocity for minimum afterbody drag. This configuration was tested to verify the "design fix" suggested by the Navy and Vought conclusions derived from reviews^{10, 11} of the HDV range test performance. The IRV model is shown mounted in the wind tunnel in Figure 3-2.

3.1.3 Advanced Tactical Vehicle (ATV)

The ATV configuration was derived as the best approach, within the constraints of using existing hardware, to demonstrate the low installed power requirements for self propulsion provided by the integrated afterbody propulsor concept, as applicable to a class of vehicles pertinent to the undersea missions being studied in the DARPA-funded program of Advanced Fluid Dynamics Research (AFDR). Interest is primarily in low-speed, low-Reynolds number, fully turbulent vehicles with emphasis on long-range and long-endurance capabilities. It will be shown in later analyses and discussions that optimum propulsive performance for the ATV would actually be attained with a configuration of higher fineness ratio than the $1/d = 2.65$ evolved from the HDV configuration. Nevertheless, the HDV/IRV forebody was used with the ATV model and tripper strips were attached at the 13 percent body station and on the shroud to transition the laminar boundary layers to provide a fully turbulent body. The blowing jet exit was sized and located on the afterbody to provide self propulsion with minimum afterbody drag according to the same criteria used in the IRV design.

Two sets of fins were designed and tested on the ATV body. One set is the same as that used with the IRV and the other set is approximately twice as large in surface area and has sweepback, providing a slight positive static stability for the complete ATV configuration. The leading edge sweep angle is 45 degrees and the trailing edge sweep angle is 70 degrees, relative to the body axis. The airfoil section taken at 30 degrees to the body axis is a NACA 0006. This geometry gives the swept fins taper in both planform and thickness.

The smaller fins have an unswept leading edge and a slight forward sweep on the trailing edge. The total span is equal to the maximum body diameter.

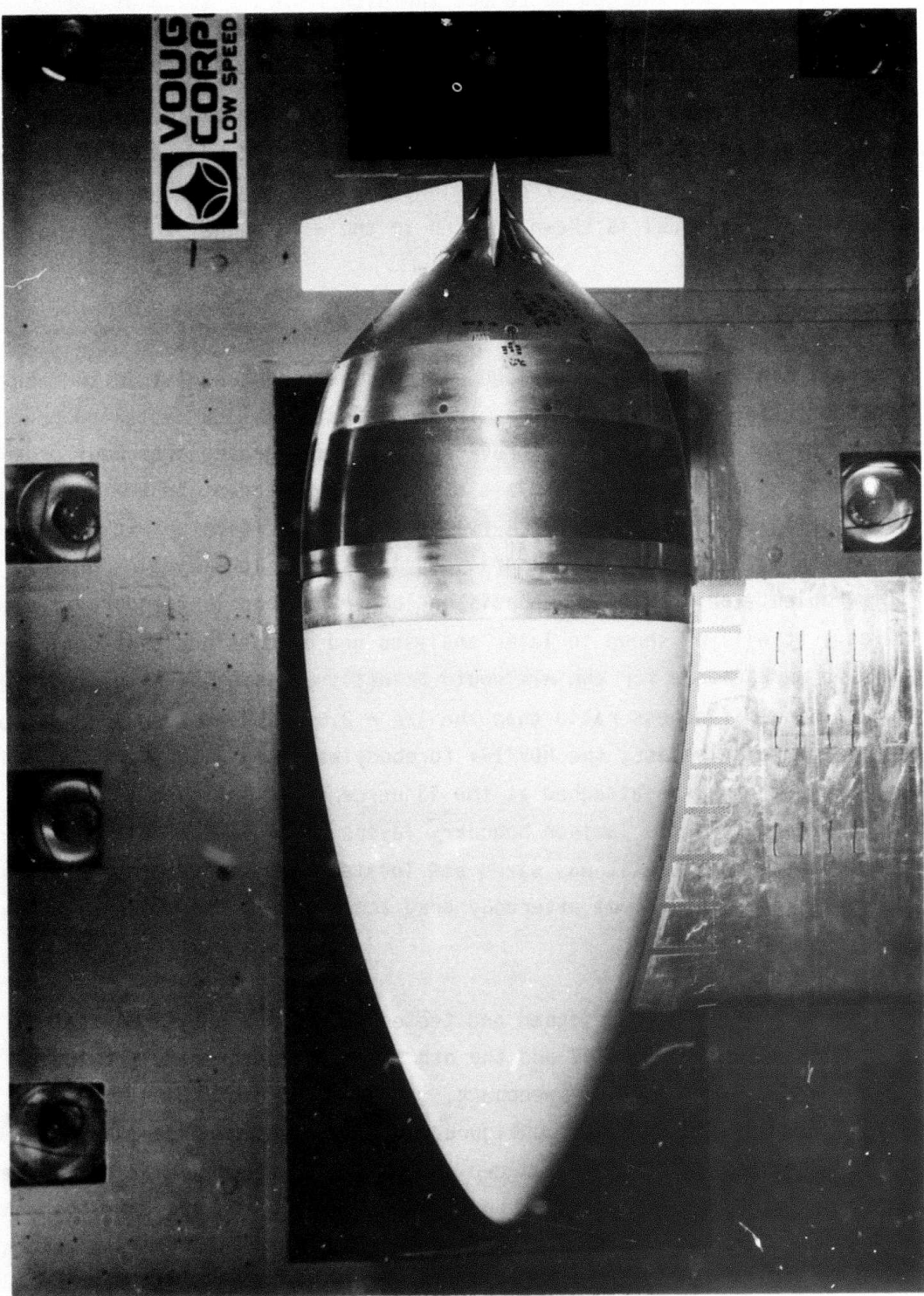


FIGURE 3-2 IRV INSTALLATION IN WIND TUNNEL

The airfoil section is a NACA 65A008, chosen for minimum drag due to the laminar flow design. The ATV model is shown mounted in the wind tunnel in Figures 3-3 and 3-4.

3.1.4 Inlet Candidates

Two inlet configurations were designed for the ATV to investigate the most efficient approach to utilizing the energy of the vehicle boundary layer in the propulsion system. The capture area of both inlets was set by the flow rate requirements calculated from the predicted vehicle drag and thrust required, assuming a fully-turbulent body. At the ATV design operating point the capture area just exceeds the total forebody boundary layer flow area. The axial-prediffusing inlet was developed for a fixed point design flow rate condition and provides some diffusion of the flow before entry into the inlet in order to reduce internal total pressure losses due to turning and viscous effects. The second inlet was designated as semi-flush and does not pre-diffuse the flow but induces some turning before entry. Theoretically, the semiflush inlet is slightly less efficient at its design point than the axial-prediffusing inlet, but it can operate off design with less degradation of performance than can the axial-prediffusing inlet.

All four inlet test configurations are shown in profile in Figure 3-5.

3.2 FACILITIES AND SUPPORT SYSTEMS

The test program first phase required the use and coordination of several Vought facilities. Some items were specially developed for this test but were designed for versatility and use in other applications. Descriptions of the facilities and support systems follow.

3.2.1 Vought Low Speed Wind Tunnel

The Low Speed Wind Tunnel (LSWT) is a closed-circuit facility with 15 x 20-foot and 7 x 10-foot test sections arranged in tandem with a total speed range of 9 to 350 fps. The air flow is provided by a twenty-foot diameter fan that is powered with a 1500 horsepower electric motor. Models are supported with either rear sting or strut mount systems. Aerodynamic forces acting on the model are measured with balances that may be located either internally or

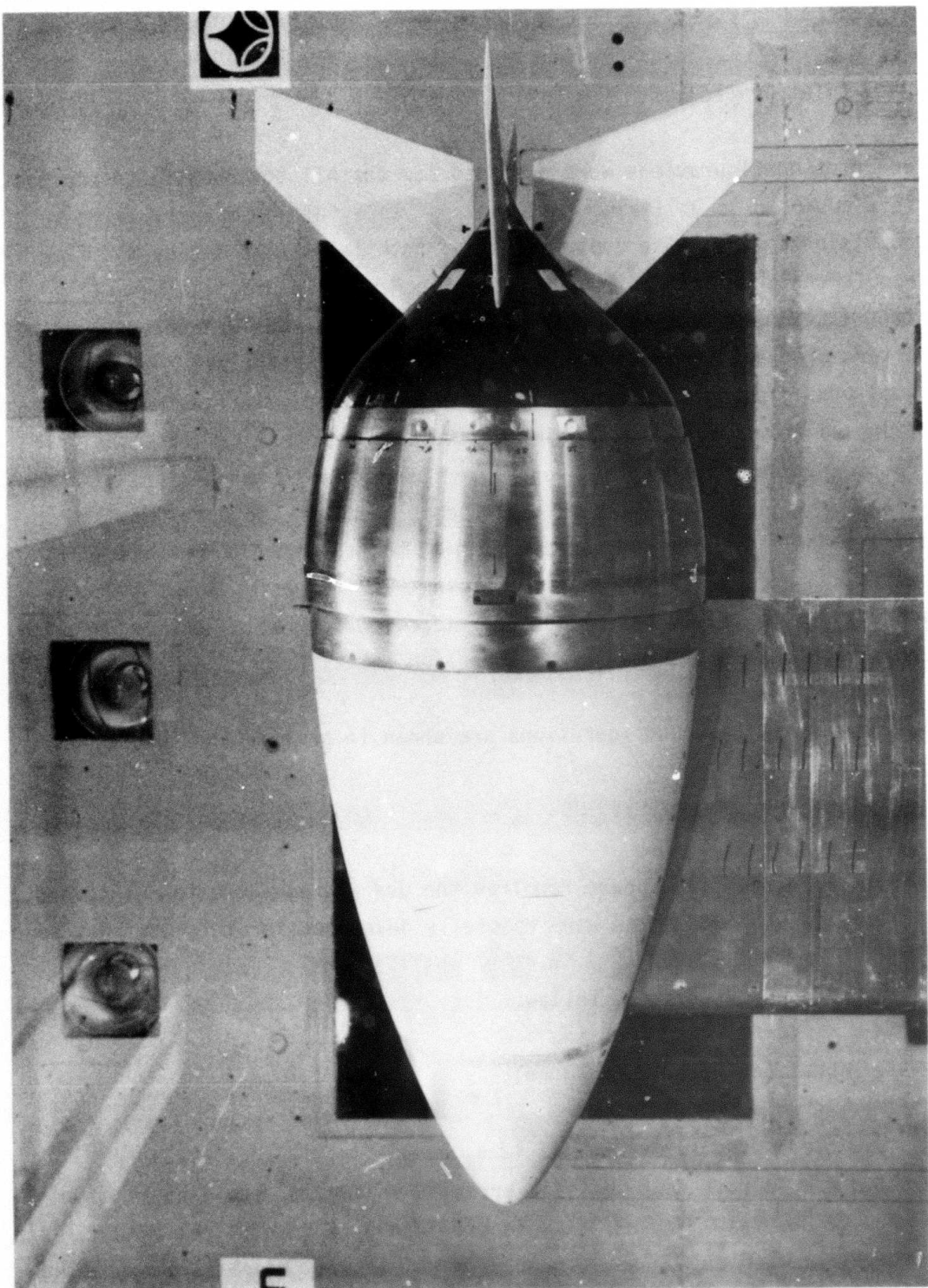


FIGURE 3-3 ATV WITH SWEPT FINS IN WIND TUNNEL

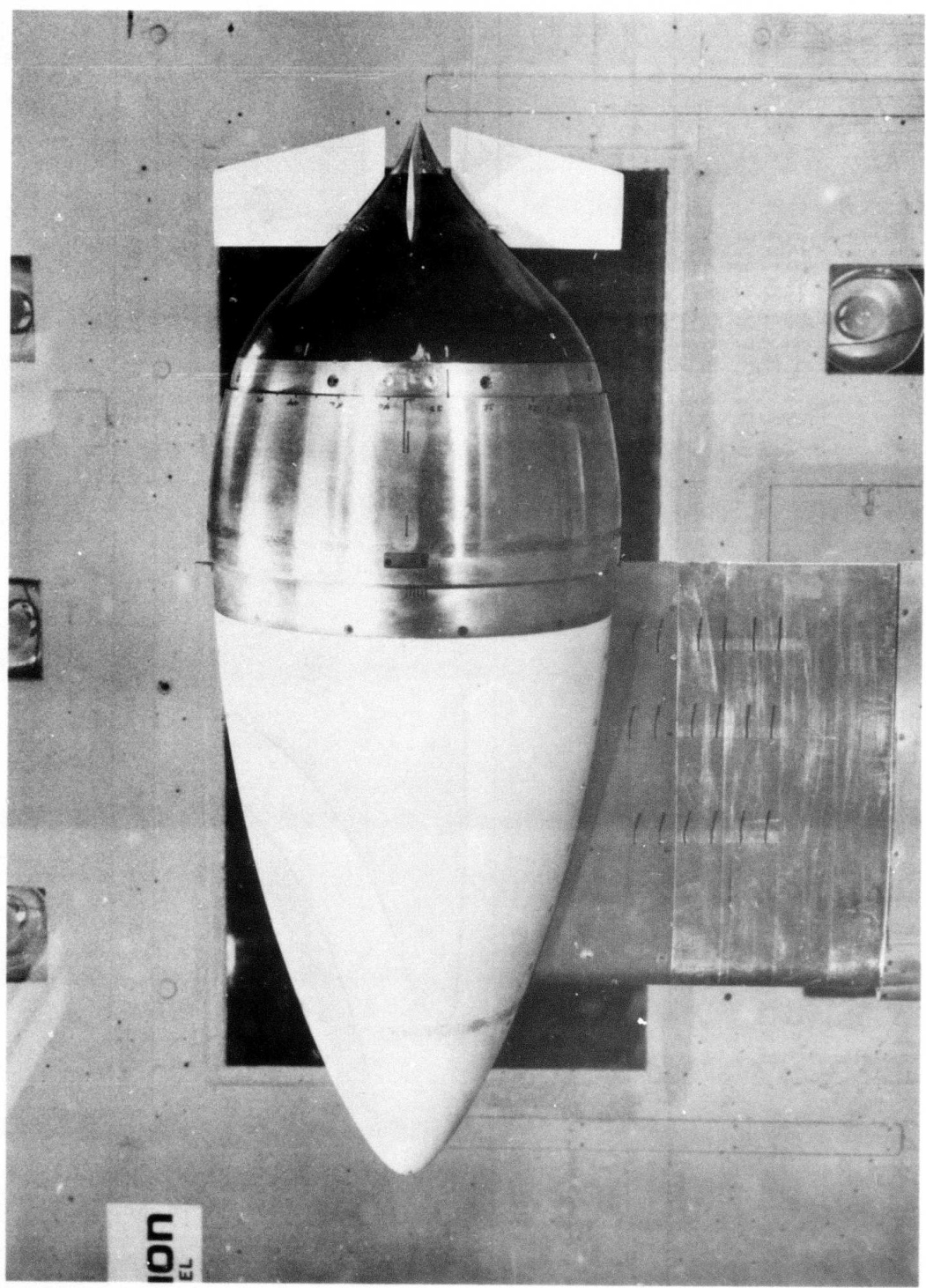


FIGURE 3-4 ATV WITH UNSWEPT FINS IN WIND TUNNEL

LAMINAR-FLOW DESIGNS

- o MINIMUM EFFECT ON EXTERNAL LAMINAR BOUNDARY LAYER
- o IMPROVED INLET PRESSURE RECOVERY WITH LAMINAR FLOW DOWNSTREAM OF LIP

RADIAL

TURBULENT FLOW DESIGNS

- o GOOD TOLERANCE TO ABOVE-DESIGN FLOW RATES
- o PREDIFFUSION DESIGN CONDITION

SEMI-FLUSH

FIGURE 3-5 INLET CANDIDATES

externally to the model. In addition to force measurements, model pressure, temperature, flutter and flow visualization are standard measurements. Three-foot span two-dimensional channels are available for wing development testing.

The 7 x 10-foot test section used in this test has a speed range of 40 to 350 feet per second at atmospheric pressure. Several model support systems are available in this test section. For example, a model may be mounted on an internal force balance and supported by a rear sting system that has 50 degree pitch and ± 90 degree yaw ranges. Alternatively, a model may be mounted to a strut using either an internal or external balance. The strut is mounted to a turntable that provides an angle of incidence (yaw) of $\pm 90^\circ$. Angle of attack for a single strut mount may normally be obtained with a hydraulically powered mechanism which is housed within the model. The external balance is also routinely used with three-support or tandem two-support systems where strut actuation provides a $\pm 60^\circ$ pitch control. For this test the support strut was pitched with the model and an internal balance was used.

3.2.2. Model Mounting Facility

Powered models can be supported in the Vought LSWT by a special mounting facility that hinges to the floor of the wind tunnel and attaches to the tunnel pitch mechanism. The facility was designed specifically for use in testing models employing blowing and suction simultaneously. The facility consists of a symmetrical-section strut with internal air passages, a force balance adapter, and a coaxial duct and bellows assembly that effectively uncouples the model from the grounded air channels. An image strut is also included for use in determining the interference effects of the mounting strut on the body forces of the metric model. The mounting facility is a Vought capital item designed for use in propulsion/BLC tests of various air-breathing missile and tactical aircraft concepts, as well as the simulation testing of underwater vehicle concepts. The complete installation is illustrated in Figure 3-6, with an Advanced Tactical Vehicle model shown. A more complete description of the various components follows.

3.2.2.1 Main Support Strut

The main support strut was sized to satisfy two criteria; provide adequate cross-sectional area to enclose the blowing and suction supply air channels, and minimally perturb the pressure distribution on a model forebody such that

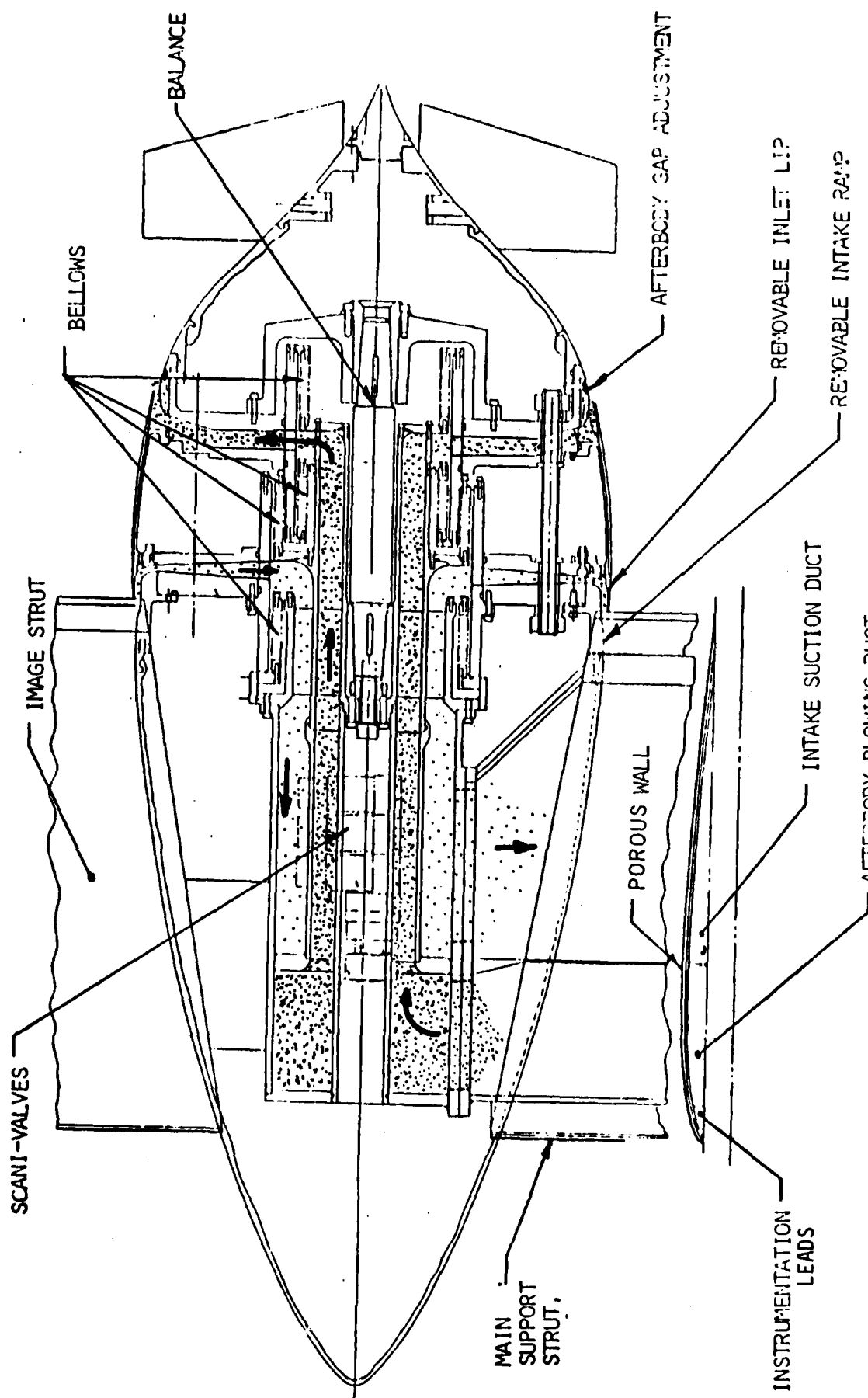


FIGURE 3-6 DUAL-FLOW BELLOWS FACILITY ARRANGEMENT

laminar boundary layer flow can be maintained, when desired, up to the inlet. This second criterion was imposed so that test results could be obtained for the Vought HDV configuration for comparison with the HDV data base from the previous in-water free-running test program. The first criterion resulted in an external cross-sectional area requirement of 21.64 in.²

Several airfoil sections were examined to determine their effect on the model pressure distribution. The approach is illustrated in Figure 3-7. The velocity distribution as established by the potential flow pressure distribution is shown for the undisturbed model forebody. A laminar boundary layer separation criterion was assumed for transition, which was specified to occur at the suction inlet. This allows calculation of the limit on local velocity overshoot on the forebody, as a function of model Reynolds number, that will just cause transition at the inlet.

The first candidate section was the NACA 0024 (24 percent thickness ratio). The severe bluntness of this section was found to produce a large velocity overshoot and adverse pressure gradient well in excess of the transition criterion limit. Although the compactness and inherent stiffness of this strut was desireable from a structural design standpoint it proved to be unacceptable. An iterative analysis showed that for the 4-digit series airfoil sections the thickness ratio would have to be reduced to 10 percent or less to satisfy the transition criterion. However, even though the NACA 0010 section produces an acceptable pressure perturbation on the model forebody, as shown in Figure 3-7, there was concern that its own boundary layer would transition and result in tripping the model boundary layer.

The final choice for the strut section was based on an NACA section series designed for laminar flow. The 65A008 section was checked against the criteria and found to be acceptable both from the standpoint of maintaining laminar flow on the strut as well as on the model. As an additional precaution the strut was configured with a porous skin over the upper half of the span so that the boundary layer could be removed by suction if and when necessary to minimize interference effects with test models. The nominal 8 percent thick strut has a chord of 19 inches and a maximum thickness of 1.6 inches.

The strut is of welded 17-4 stainless steel construction with separate

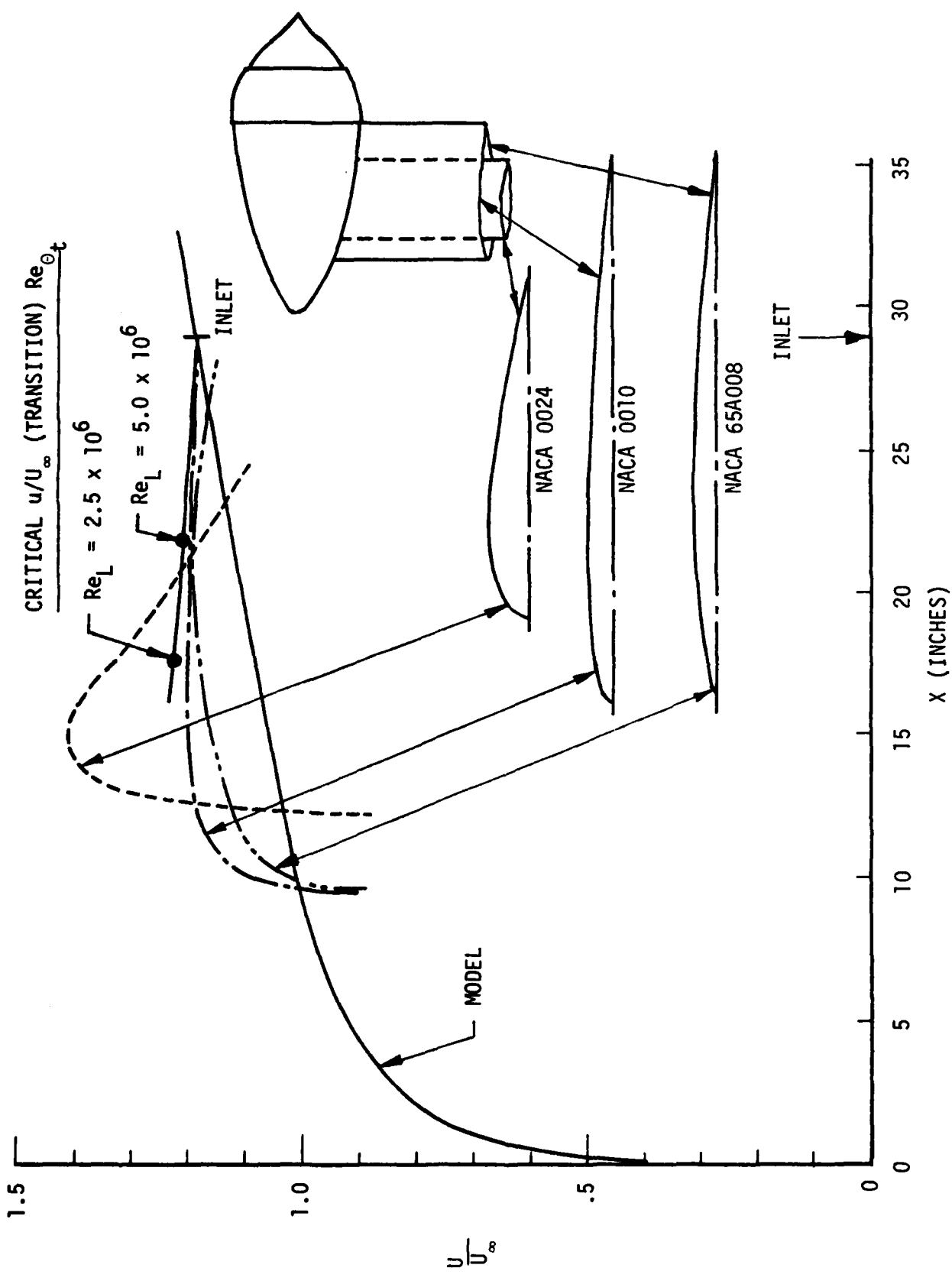


FIGURE 3-7 SUPPORT STRUT AIRFOIL SECTION DEFINITION

flow channels for the blowing, main suction, and strut suction lines. Blowing air is brought in through two 2-inch AN fittings, strut suction flow is taken out through two 2-inch AN fittings, and the main suction supply connects to a 3.75-inch diameter pipe, all welded into a mild carbon steel multi-plenum assembly. Allowable model loads used for the strut design were 25 lbs normal force, 30 lbs axial force, 3 lbs side force and 2500 inch-lbs pitching moment. A possible strut side force of 40 lbs due to angle of attack (yawed model) was also included. All structural components were sized to provide a factor of safety of 10 or greater for these loadings.²⁰

3.2.2.2 Image Strut

The image strut was designed to be externally identical to the support strut and also included the same capacity for boundary layer removal by suction. Since the image strut carries no model loads the internal structure was made more simple and included a hardwood core instead of steel. The image strut attaches to the top of the bellows assembly air chamber and the free end fastens to the tunnel ceiling.

3.2.2.3 Bellows Assembly

The bellows assembly consists of two coaxial air plenum chambers that fasten rigidly to the main support strut and two pairs of low-spring-rate bellows that complete and seal the model/flow channel interface. The bellows were custom fabricated to specifications by EG&G SEALOL Inc. The bellows system has a calculated spring rate of approximately 16 pounds per inch which is less than 0.01 percent of the axial spring rate of typical force balances and thus has no discernable effect on axial force measurements. With this degree of "softness" it is limited to working fluid pressures of about 20 psig. The bellows effectively uncouple a model from the grounded air channels in all force directions and for pitching and yawing moments, but roll freedom is lost due to the high torsional stiffness of the assembly.

3.2.2.4 Force Balance Adapter

The force balance adapter consists of a pair of adjustable fittings that can accommodate several different balances (Vought Nos. VB-13, VB-18, VB-21, VB-36) in the mounting fixture. This allows the mounting fixture to be used

with a variety of model shapes and sizes and a force balance to be selected for the best match to the loads and moment ranges expected with each configuration.

3.2.2.5 Force and Moment Balance

The basic Vought six-component balance design consists of four pieces. The forward piece includes the model-balance attachment and the forward pitching moment and yawing moment bridges. The center section is composed of two pieces, a rolling moment measuring element and an axial force measurement element. The aft piece contains the aft pitching moment and yawing moment bridges and the balance-sting attachment. Newer designs include one-piece six-component balances. The balance used in this test program was the VB-36 having load ratings of 2000 lbs. normal force, 800 lbs side force, 200 lbs axial force, 3000 in-lb pitching moment, 1200 in-lb yawing moment, and 1200 in-lb rolling moment.

3.2.3 Auxilliary Air System

The air for blowing the BLC/propulsion system was taken from the main high-pressure supply of the Vought High Speed Wind Tunnel (HSWT) facility. This air system has a volume capacity of 28,000 cubic feet stored at 600 psia and can deliver up to 18 pounds per second mass flow rates in the auxilliary mode, more than ten times the BLC requirements for this test.

The model suction was provided by two large Roots-type vacuum blowers connected in parallel to the model mounting facility. An ejector, driven also by the HSWT high-pressure air, provided suction for removal of the support strut and image strut boundary layers, although this was eventually found to not be necessary with turbulent test models.

The flow rates for model suction, strut suction, and BLC/propulsion blowing were all independently controlled and measured.

3.2.4 Test Plan

The test plan was developed to meet the objectives listed in Section 1.2. Specifically, the tests were planned to validate the HDV performance, test an

improved HDV configuration (IRV), and assess the performance benefits of an integrated afterbody propulsor for application in advanced underwater vehicle systems (ATV). The principal parameters to be evaluated were afterbody drag, fin drag, thrust conditions required for self propulsion, inlet performance, and stability and control. A sub task was to evaluate and correct for strut interference effects on model force measurements. Figure 3-8 shows the complete run schedule. A total of 70 air-on runs were made with an additional 9 runs being made with the tunnel off to provide calibrations, static bellows tares, and blowing jet velocity surveys.

Run PTS	Configuration	Inlet	Fins	q set	a set	RAKES				Image Strut Suct.	Comment	
						Wake	F/B	Snill	Jet	A/B		
53	7	Adv. Inlet	Semi-Flush	Off	80 psf	0°	0-1.5 lbm/sea. Horiz	On	Off	On	0	Untripped (1am Flg.)
54	6										0	0.1-0.6 Strut Suction Effects
55	7					30		0-1.5			0	
56	5							1.1			0.1-0.6 Strut Suction Effects	
57	7						0-1.5		Off	Off	0	
58	8							0.7 (Bal)			0.1-0.6 Strut Suction Effects	
59	7							0-1.1		On	0	Turb. Trip @ 12%
60	14									Off	0.0.6	
61	15					20						
62	10					80		1.2-max.				A/B not well attached 3 max fl
63	10						1	+5°				Strut Interference
64	15					30		0-0.8				
65	10					20		0-0.7				
66	7						1	0°	0-0.9			out 3 Force Data/Performance
67	7					30						
68	5					80						
69	5											
70	7					20	-5°/+5°	0.7				Angle-of-Attack Effects
71	7					30		0.85				
72	7						50		1.48			
73	8					Swept (0°)	20	0°	0-1.0			Swept Fin Stability
74	8						30		0-1.0			
75	6						50		0-1.4, max			
76	7						20	-5°/+5°	0.7			
77	7						30		0.85			
78	6							50		1.48		Fin Effectiveness
79	7					(-5°)						
80	7					(-10°)						
81	8					Unswept (0°)	20	0°	0.5-1.0			Unswept Fin Stability
82	8						30					
83	6						50		1.0-1.4, max			
84	7						20	-5°/+5°	0.7			
85	7						30		0.85			
86	7							50		1.48		

FIGURE 3-8. WIND TUNNEL RUN SCHEDULE

Run PTS	Configuration	Inlet	Fins	q set	a	Inlet	PAKES			Image	Strut	Content	
							lake	F/B	Stall	Jet	A/B	Strut Suct.	
87 7	Adv. Tact. Veh.	Semi-flush	Inlets	50	-5°/+5°	1.48	Horiz.	On	Off	Off	Out	0	Fin Effective Area
22 7	Adv. Tact. Veh.	Semi-flush	Inlets	50	(-10°)	1	Horiz.	On	Off	Off	Out	0	Fin Effective Area
23 -	-	-	-	0	-	0 - max.	-	-	-	-	-	-	Critice Critical Condition
93 -	-	-	-	-	-	0 - max.	-	-	-	-	-	-	Critice Critical Condition
91 -	Void	-	-	-	-	-	-	-	-	-	-	-	Critice Critical Condition
92 5	Adv. Tact. Veh.	Semi-flush	Off	50	0°	1.1 - max.	Horiz.	On	Off	Off	Out	0	Reheat
93 8	-	-	-	20	-	0.3 - 1.0	-	-	On	-	-	-	Jet/C/S Flow Test
94 3	-	-	-	30	-	0.3 - 1.0	-	-	-	-	-	-	-
95 8	-	-	-	50	-	0.8 - max.	-	-	-	-	-	-	-
96 8	-	-	80	-	-	-	-	-	-	-	-	-	-
97 5	-	-	1	-	-	-	-	-	Off	-	-	-	-
98 6	-	-	30	-	0.5 - 1.0	-	-	-	-	-	-	-	-
99 5	-	-	1	-	-	-	-	-	-	-	-	-	-
100 9	-	Axial	20	-	-	-	-	On	On	-	-	-	Remote Terminal
101 9	-	-	30	-	-	-	-	-	-	-	-	-	Axial Inlet Tests
102 6	-	-	80	-	-	-	-	-	-	-	-	-	-
103 -	-	-	0	-	0 - max.	-	-	-	On	-	-	-	Series Flow Water Test
104 7	Adv. Tact. Veh.	Semi-flush	Off	20	0°	0.4 - 1.0	Horiz.	On	On	On	Out	0	Complete Fins/Strut Test
105 7	-	-	-	30	-	0.6 - 1.2	-	-	-	-	-	-	-
106 8	-	-	-	50	-	0.9 - max.	-	-	-	-	-	-	-
107 -	-	-	-	80	-	-	-	-	-	-	-	-	-
108 -	Adv. Tact. Veh. Dada	T/B Fins	0°	0	-	-	-	-	-	-	-	-	Sealed Sicks Pressure Test
109 -	-	-	-	-	-	-	-	-	-	-	-	-	Sealed Sicks Test
110 8	-	-	80	0°	0 - 0.7	-	-	-	Off	Off	Out	0.6	Rance Test Date
111 6	-	-	-	-	0.4 (bal.)	-	-	-	-	-	-	-	0.5-1.0
112 -	-	-	-	-	(suct max)/m _{flow} = 0.3-0.7	-	-	-	-	-	-	-	-
113 3	-	-	-	-	-	-	-	-	-	-	-	-	-
114 6	-	-	-	-	-	-	-	-	-	-	-	-	-
115 6	-	-	50	-	-	-	-	-	-	-	-	-	-
116 6	-	-	50	-	-	-	-	-	-	-	-	-	-
117 6	-	-	80	-	-	-	-	-	-	-	-	-	-
118 5	-	-	-	-	-	-	-	-	-	-	-	-	0.2-0.6
119 5	-	-	-	-	+5°	0 - 0.9	-	-	-	-	-	-	0
120 9	-	-	-	-	-	-	-	-	-	-	-	-	0.6

FIGURE 3-8. WIND TUNNEL RUN SCHEDULE (Continued)

FIGURE 3-8. WIND TUNNEL RUN SCHEDULE (Continued)

4.0 INSTRUMENTATION

The wind tunnel tests described in this report relied heavily on a comprehensive set of experimental data for evaluation of the drag/power characteristics of the Vought integrated afterbody propulsor concept in a complete vehicle configuration. This required more instrumentation than is typical for most wind tunnel tests.

4.1 FORCE AND MOMENT BALANCE

To begin, the test models were a combination of force model and pressure model simultaneously. Normally, separate models are used for the two different types of test, but in this case the special mounting installation (described in Section 3.2.2) allowed the use of full pressure instrumentation without grounding out the model and force balance. The balance used was a unique Vought design capable of measuring three mutually perpendicular force components (axial, normal, and side force) and the moments about the three corresponding axes. More description is given in Section 3.2.2.5.

4.2 BODY STATIC PRESSURES

All of the test model modules were instrumented with static pressure taps such that every configuration tested had three rows of static pressure ports spanning the entire length; a row along the top, one on the bottom, and one along the port side. Additionally, there were arrays of static pressure ports located in the inlets (top and side) on both the body-side surface and on the inside surface of the inlet lip.

4.3 TOTAL PRESSURE RAKES

All total pressure rakes were made of stainless steel tubing. The ends of probes located in steep velocity gradients were flattened to an approximate 0.005-inch opening height to better localize the measurements. All external boundary layer probes were soldered in brass plugs machined to exactly match the local body surface contour. The rake assemblies could be removed and replaced with contoured blank plugs to fill the surface when making clean-body force measurements. On installation, each probe was individually sealed with small o-rings to pressure-line plumbing permanently installed inside the

model. This allowed installation or removal of the rakes at any time without having to get inside the model to make or break pressure-line connections. Each rake location had a correspondingly located body static pressure tap. Rake installation is illustrated in Figure 4-1.

4.3.1 Forebody Rakes

Each inlet configuration was equipped with two total pressure probe rakes mounted on the forebody (near the top and on the starboard side) to characterize the forebody boundary layer just ahead of the inlet. For the laminar flow bodies (HDV and IRV) the rakes had only two probes each, spaced nominally 0.020 and 0.075 inches above the surface. The probes were made of 0.050-inch diameter tubing with the ends flattened. The higher probe served only as a check on the state of the boundary layer, as it was above the outer limit of a laminar boundary layer and therefore would see local freestream total pressure unless the flow was transitioning. The lower probe was sufficient to characterize the laminar boundary layer since the velocity profile is calculable by analytical means, given a single data point and local freestream conditions.

The turbulent forebody ATV configuration had six probes in each rake spaced at nominally 0.050, 0.100, 0.150, 0.250, 0.500, and 0.800 inches above the surface. Actual probe height was checked with feeler gages on each installation and the measured numbers were input to the data reduction. Probe locations were the same for both the semi-flush and axial-prediffusing inlet configurations, although separate rakes were used because of the different body contour at the plug locations. These probes were also made of 0.050-inch diameter stainless steel tubing and the lowest probe in each rake was flattened as described previously.

4.3.2 Inlet Rakes

Each inlet module had two total pressure rakes permanently installed at or near the top and on one side to measure the total head distribution coming in at or near the inlet lip. No rakes were installed at the bottom because of the mounting strut, however the top and side rakes were sufficient for determining effects of angle of attack. The HDV radial inlet had two four-probe rakes located one on the side and one at the top. The tips of the probes were located 0.050 inches inside from the shroud lip leading edge. The spacings

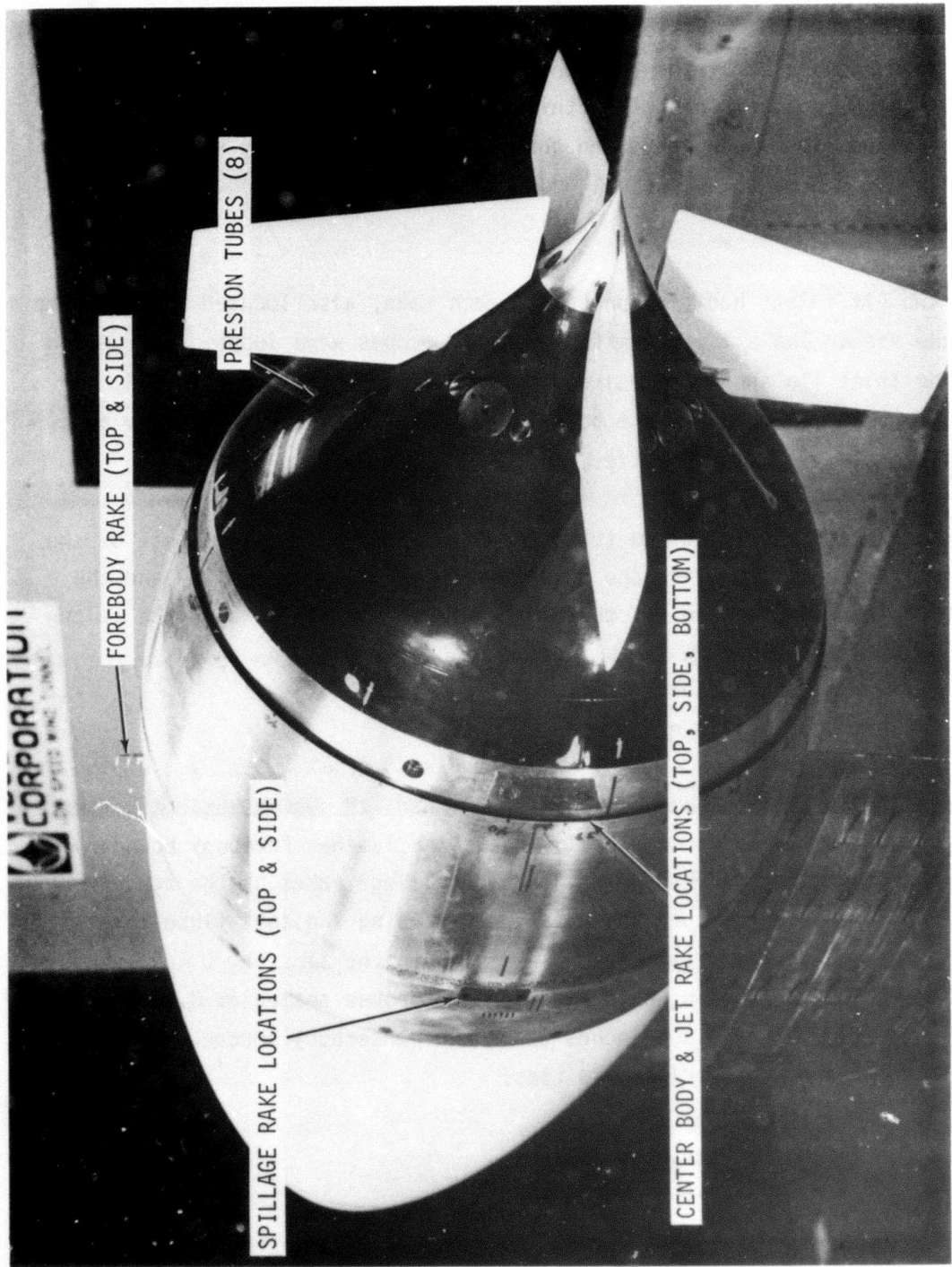


FIGURE 4-1 INSTRUMENTATION INSTALLATION - AT&T

were designed to be 0.015, 0.025, 0.035, and 0.045 inches off of the forward, or body-side, inlet surface. The probes were made of 0.043-inch diameter tubing with flattened ends.

The submerged inlet of the IRV configuration had two rakes very similar to those for the HDV radial inlet. In this case the probe tips were exactly even with the shroud lip leading edge and the spacings off the body surface were designed to be 0.020, 0.040, 0.060, and 0.080 inches. The probe tips were also flattened.

The two ATV inlets had five probes in each rake, also located near the top and on the side. The axial-prediffusing inlet probes were located 0.100-inch inside the inlet lip and were designed to be spaced 0.035, 0.085, 0.135, 0.185, and 0.215 inches above the body surface and parallel to the body axis. These probes all had flattened tips.

The semi-flush ATV inlet had total pressure rakes similar to those of the axial-prediffusing inlet, with the probes 0.100-inch inside the lip and the tips set at the same spacing off the body surface but aligned with the calculated slopes of the incoming streamlines.

4.3.3 Centerbody Spillage Rakes

No spillage rakes were provided on the HDV and IRV configurations since the inlets were designed to completely ingest the laminar forebody boundary layers. The turbulent ATV configuration had spillage rakes on the top, bottom, and port side for both the axial-prediffusing and semi-flush inlets. The probe designs were the same in both cases with the tips set 0.465 inches aft of the shroud lip leading edge and with six probes spaced at 0.020, 0.050, 0.100, 0.200, 0.300, and 0.500 inches above the centerbody shroud surface. The three lower probes had flattened tips.

4.3.4 Centerbody Boundary Layer Rakes

The boundary layer exiting the trailing edge of the centerbody was of paramount interest for all configurations, as this was the single-most important parameter in establishing the BLC requirements for the afterbody. For the HDV and IRV configurations, which were designed for no spillage and laminar flow

shrouds, the centerbody rakes had only three probes - all with flattened ends, located 0.100 inches ahead of the shroud trailing edge, and spaced 0.015, 0.030, and 0.050 inches above the shroud surface. These rakes mounted in the afterbody skin and were removable. They were located on the top, bottom, and port side.

The ATV centerbody boundary layer rakes were also mounted in the afterbody and were combined in common with the BLC jet rakes, which will be described next. These centerbody rakes each had six probes with tips located 0.100 inch ahead of the shroud trailing edge, and spaced at 0.020, 0.050, 0.100, 0.200, 0.300, and 0.600 inches above the shroud surface. These rakes were also located at the top, bottom, and port side. The lower three probes in each rake were flattened.

4.3.5 BLC Jet Rakes

Each configuration had three total pressure rakes mounted on the afterbody, with flattened probe tips at the jet exit plane. On the HDV and IRV models the jet rakes were permanently mounted beside and slightly offset from the centerbody boundary layer rakes. These jet rakes each had five probes with flattened tips spaced 0.015, 0.025, 0.030, 0.035, and 0.045 inches above the afterbody surface on the HDV, and 0.015, 0.030, 0.040, 0.050, and 0.070 inches above the afterbody surface on the IRV.

On the ATV configuration the jet probes were mounted in the same plugs with the centerbody boundary layer rakes and were therefore removable. These also consisted of five probes per rake with flattened tips and a design spacing of 0.040, 0.080, 0.090, 0.100, and 0.140 inches above the afterbody surface.

4.3.6 Afterbody Wake Rakes

The ATV configuration only was designed to have total pressure rakes that could be installed along the length of the afterbody to measure the boundary layer development in and aft of the BLC mixing region. The probes were set in alignment with the predicted streamline angles at each location. These rakes were also removable and were located in a spiral arrangement so that they were not in each other's wake. The rakes included several static pressure probes,

along with the total pressure probes, to check the radial and axial static pressure development along the afterbody. The location and probe spacings for these rakes are listed in Table 4-1. Figures 4-2, 3, 4 show the afterbody wake rakes installed on the ATV model. Also visible is the sidemounted centerbody boundary layer and jet rake.

4.3.7 Preston Tubes

A set of Preston-type total pressure tubes was mounted flush on the surface of all three afterbodies for pressure measurements that could be converted to local skin friction values. Their locations matched afterbody static pressure tap locations, necessary for the data evaluation, and were staggered to each other's wake. The Preston tubes were made of 0.026-inch o.d. x 0.016-inch i.d. tubing with blunt ends as specified in references 21 and 22.

4.3.8 Far Wake Rake

A multi-tube pressure rake was furnished by the Vought Gas Dynamics Laboratories for pressure measurements in the far wake behind the models to provide an independent check with the force balance for net model drag forces. The wake rake had a total of 80 probes spaced a constant 0.25 inches apart. There were 73 total pressure probes and 7 static pressure probes, which were distributed over the span of the rake. All probes were 1/16-inch diameter. The rake was fixed on the tunnel centerline and located three feet behind the models as shown in Figure 4-5. The rake was normally positioned horizontally but was rotated to the vertical plane for angle of attack tests. The wake rake was connected to an independent set of pressure scanners.

4.4 MASS FLOW METERS

The mass flow rates of the inlet suction, the strut boundary layer suction, and the BLC/propulsive jet flow were all measured with standard orifice plate flow meters. The inlet suction line used two orifice diameters of 3.336 and 4.245 inches, chosen according to flow rate and sensitivity trade-offs. Orifices of 1.250 and 1.500-inch diameter were likewise used in the BLC blowing line. The strut suction line used a 6-inch diameter orifice.

TABLE 4-1
ATV AFTERBODY WAKE RAKES
(S - denotes static pressure probe)

RAKE NO. I (Sta. 35.40)	RAKE NO. II (Sta. 36.75)	RAKE NO. III (Sta. 38.25)
PROBE HEIGHT = 0.040	PROBE HEIGHT = 0.040	PROBE HEIGHT = 0.020
0.080	0.090	0.030
0.090	0.115	0.090
0.100	0.150	0.100
0.140	0.170	0.265
0.225	0.300	0.380
0.255	0.470	0.590
0.305	0.700	0.880
0.405	0.900	1.000 (S)
0.505	1.100	1.140
0.805		
RAKE NO. IV (Sta. 39.50)	RAKE NO. V (Sta. 40.00)	RAKE NO. VI (Sta. 41.00)
PROBE HEIGHT = 0.050	PROBE HEIGHT = 0.060	PROBE HEIGHT = 0.100
0.100	0.170	0.170
0.280	0.250	0.320
0.360	0.370	0.520
0.480	0.460	0.760
0.600	0.600	0.980
0.790	0.800	1.220
0.970	1.000	1.500
1.250	1.360	1.610 (S)
1.450	1.510	1.830
RAKE NO. VII (Sta. 43.00)	RAKE NO. VIII (Sta. 45.75)	
PROBE HEIGHT = 0.160	PROBE HEIGHT = 0.200	
0.250	0.300	
0.380	0.550	
0.520	0.750	
0.610	1.000	
0.950	1.360	
1.600	1.910	
2.100	2.600	
2.650	3.050	
2.850 (S)	3.370 (S)	
	3.760	

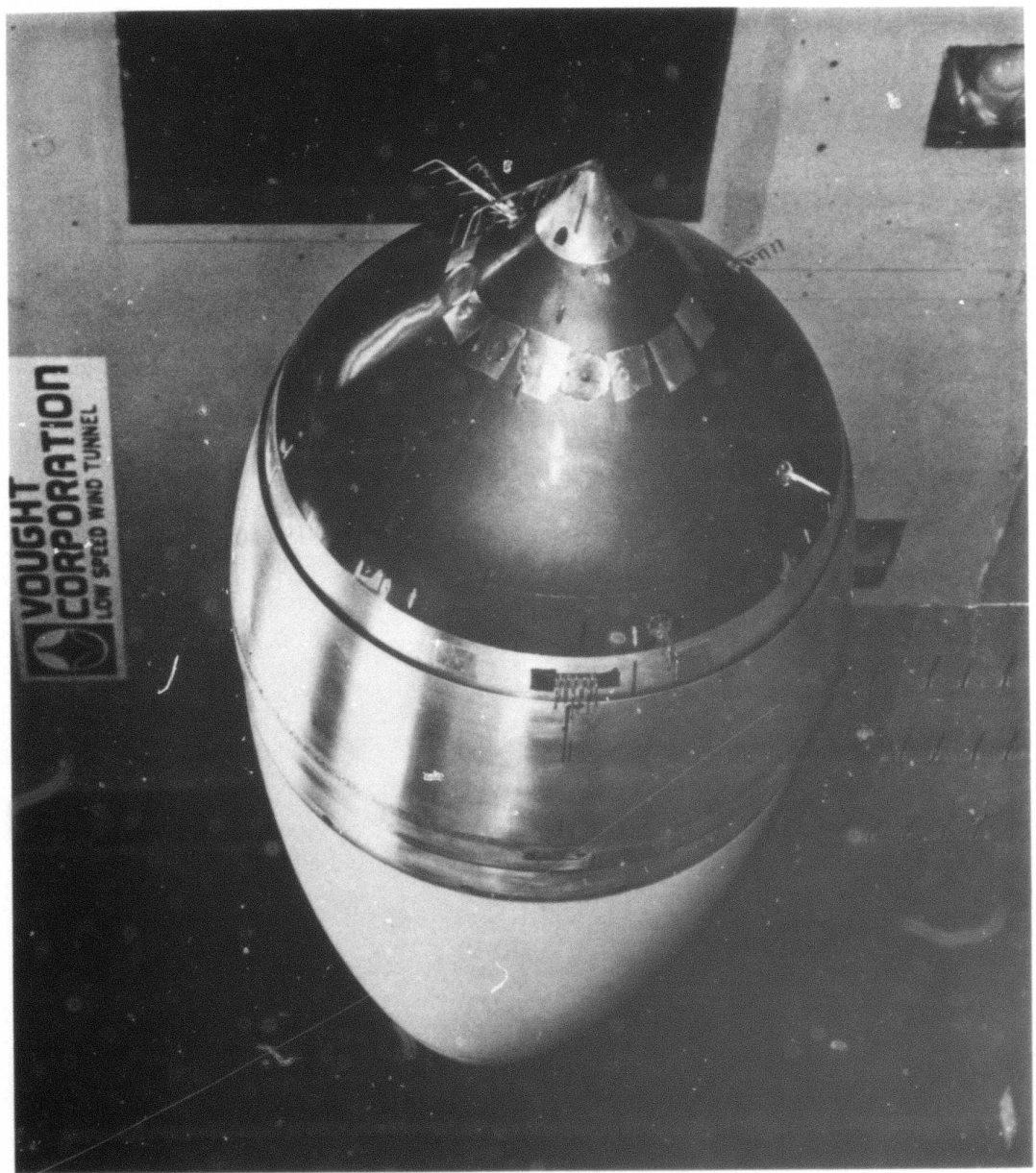


FIGURE 4-2 AFTERBODY FLOW SURVEY RAKE INSTALLATION

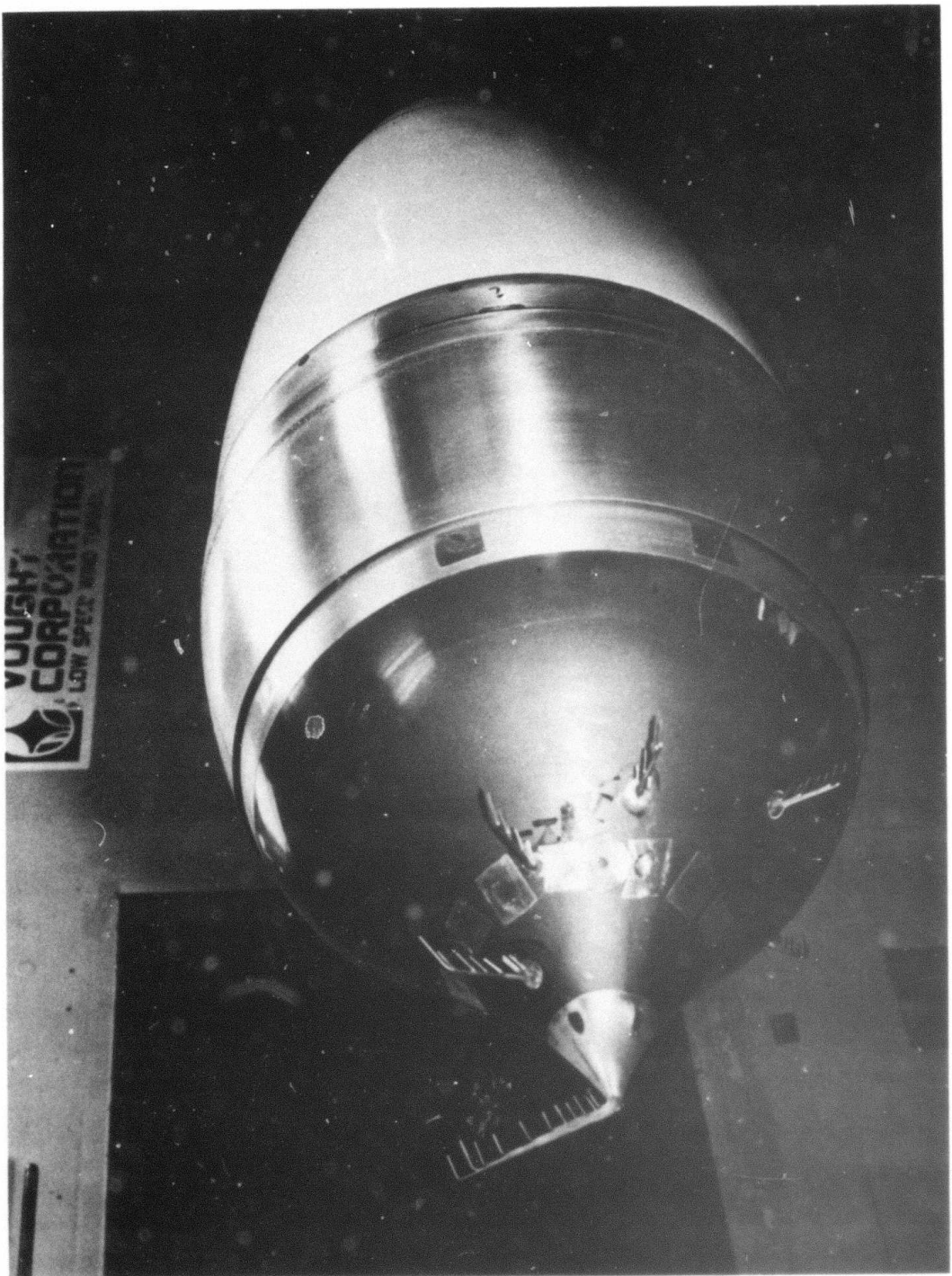


FIGURE 4-3 AFTERBODY FLOW SURVEY RAKE INSTALLATION

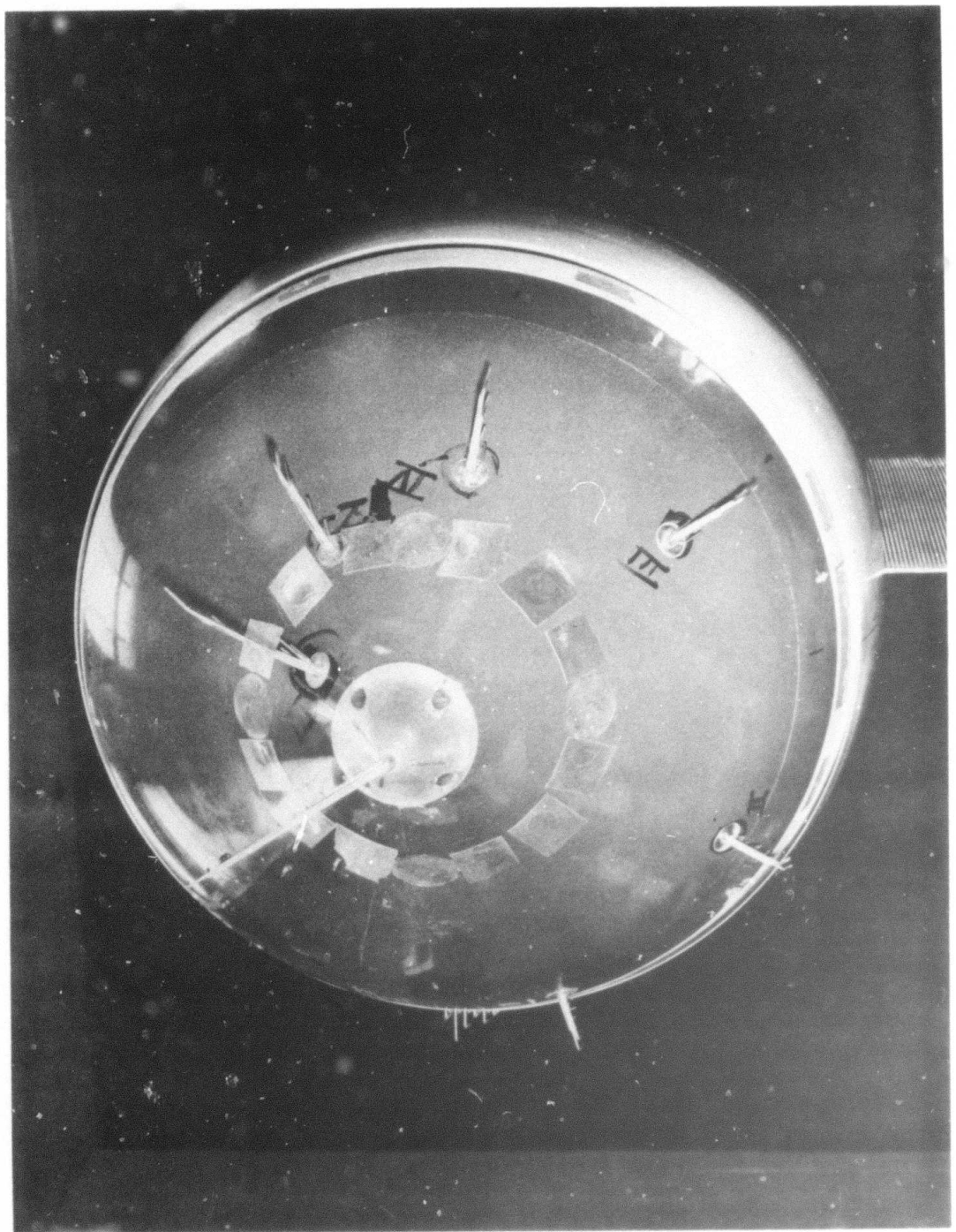


FIGURE 4-4 AFTERPODY FLOW SURVEY RAKE INSTALLATION

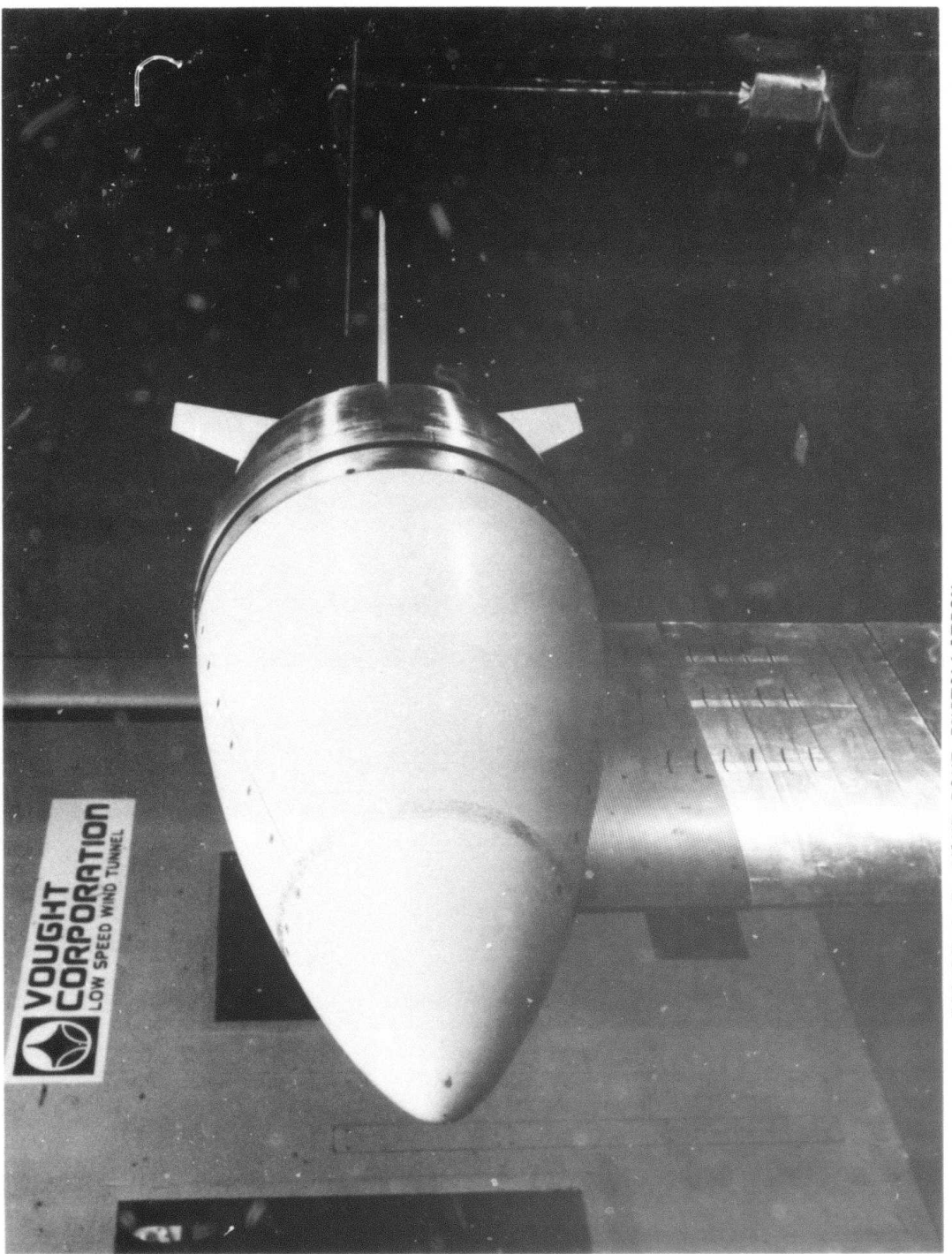


FIGURE 4-5 WAKE RAKE INSTALLATION

4.5 PRESSURE MEASUREMENT MULTIPLEXING

The many model pressures, both total and static, that were measured on each configuration were manifolded into a modular scanning and multiplexing system (tradename Scanivalve). Two banks of Scanivalve heads with five heads in each bank were mounted to the forward bulkhead of the models. Each head had its own differential pressure transducer. Each bank was powered with a stepping unit that switched pressure measurements at the rate of approximately one step per second. All transducers were referenced to room ambient static pressure and every Scanivalve head had a dedicated tap connected to a common fixed and controllable reference pressure set at 0.50 psi for a calibration check on every scan.

5.0 TEST RESULTS

This section presents the results of the Advanced Tactical Vehicle wind tunnel test program, with comparisons to analytical prediction methodology. Included are results for the HDV configuration compared with free-running in-water range data that verify the validity of the wind tunnel test approach for hydrodynamic simulation.

5.1 STATIC PRESSURE DISTRIBUTIONS

The following discusses the comparison of measured body static pressure distributions in the wind tunnel with calculated values based on potential flow theory.

5.1.1 HDV Static Pressure Distribution

In Figure 5-1 are presented the measured static pressure distributions on the HDV configuration over a range of angle of attack from -5° to $+5^\circ$ at a tunnel dynamic pressure of 80 lbs/ft² compared to a potential flow prediction for $\alpha = 0^\circ$. Data agreement with potential flow predictions is quite good, in general, with a perturbation in static pressure at the BLC jet exit and a slight velocity overshoot on the tailboom closure. Afterbody pressure recovery is excellent for a BLC-jet flow rate near self-propulsion.

5.1.2 IRV Static Pressure Distribution

Static pressure data for the IRV are shown in Figure 5-2. The agreement with prediction is again quite good and the perturbation at the BLC jet exit is much less than on the HDV due to the reduction in the jet velocity ratio and improved jet nozzle orientation.

5.1.3 ATV Static Pressure Distribution

The static pressure distribution for the ATV is shown in Figure 5-3. The agreement with predictions is generally as good as that for the laminar bodies except near the BLC-jet exit where a slight adverse gradient was generated

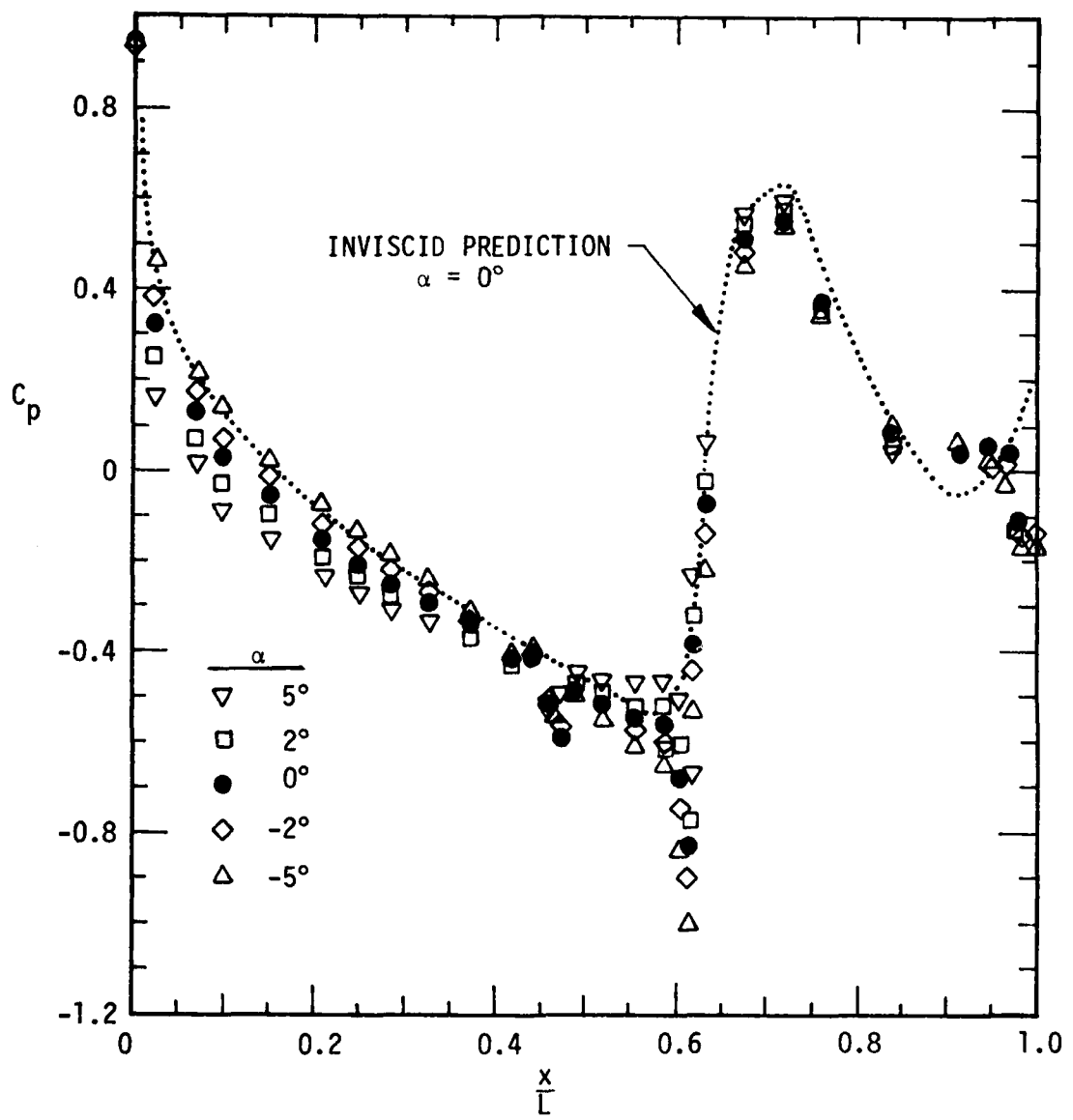


FIGURE 5-1 HDV STATIC PRESSURE DISTRIBUTION

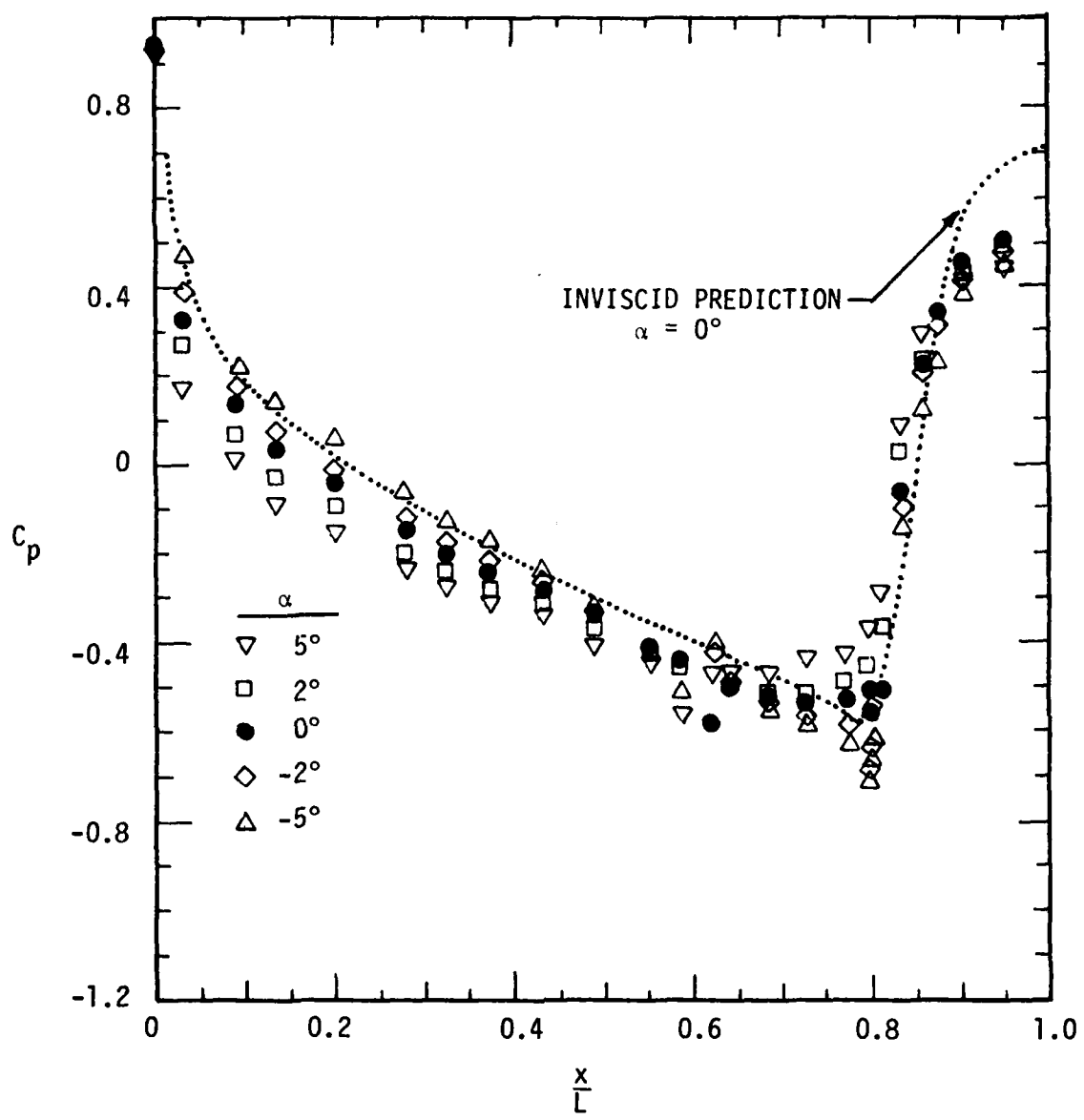


FIGURE 5-2 IRV STATIC PRESSURE DISTRIBUTION

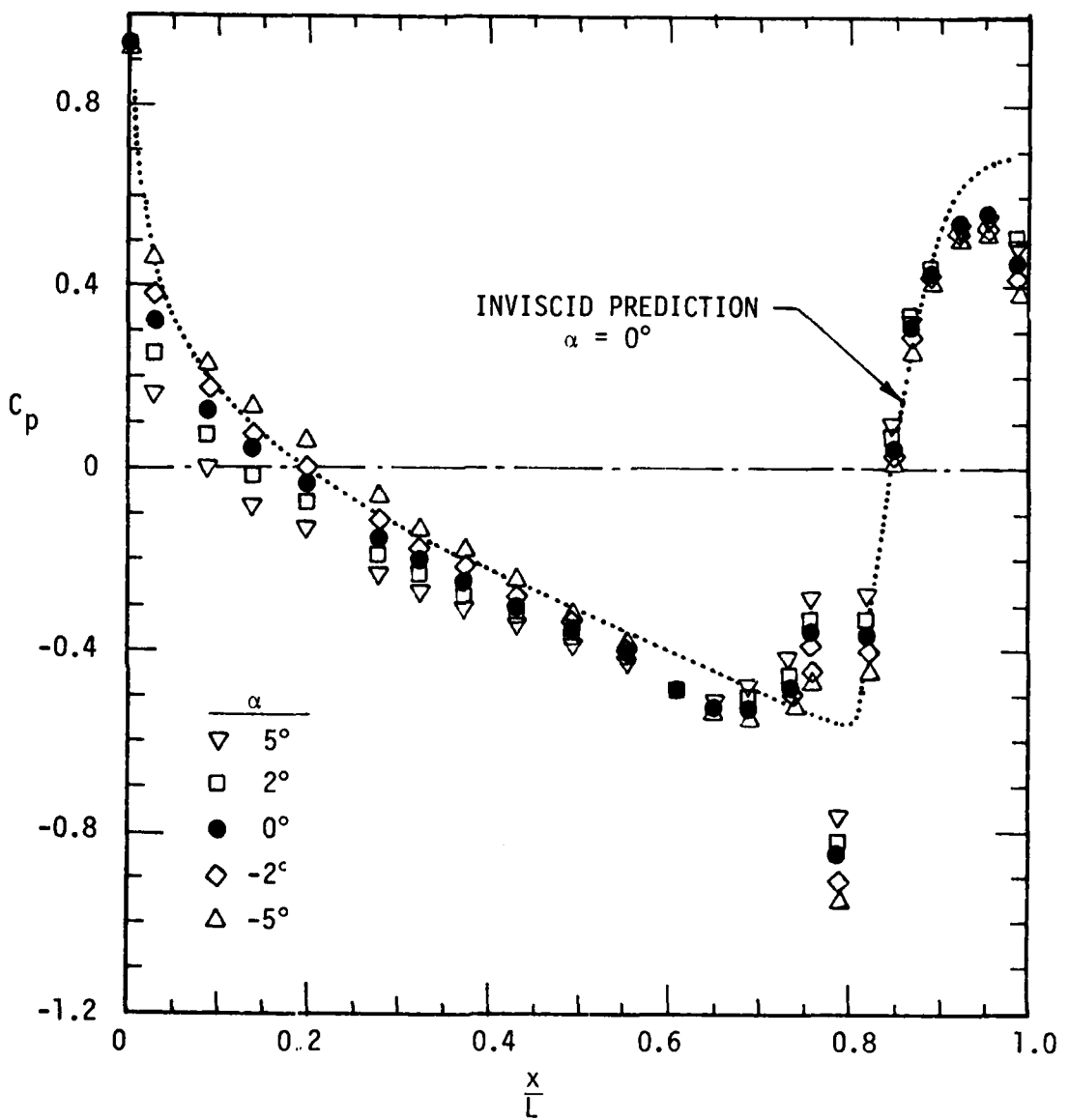


FIGURE 5-3 ATM STATIC PRESSURE DISTRIBUTION

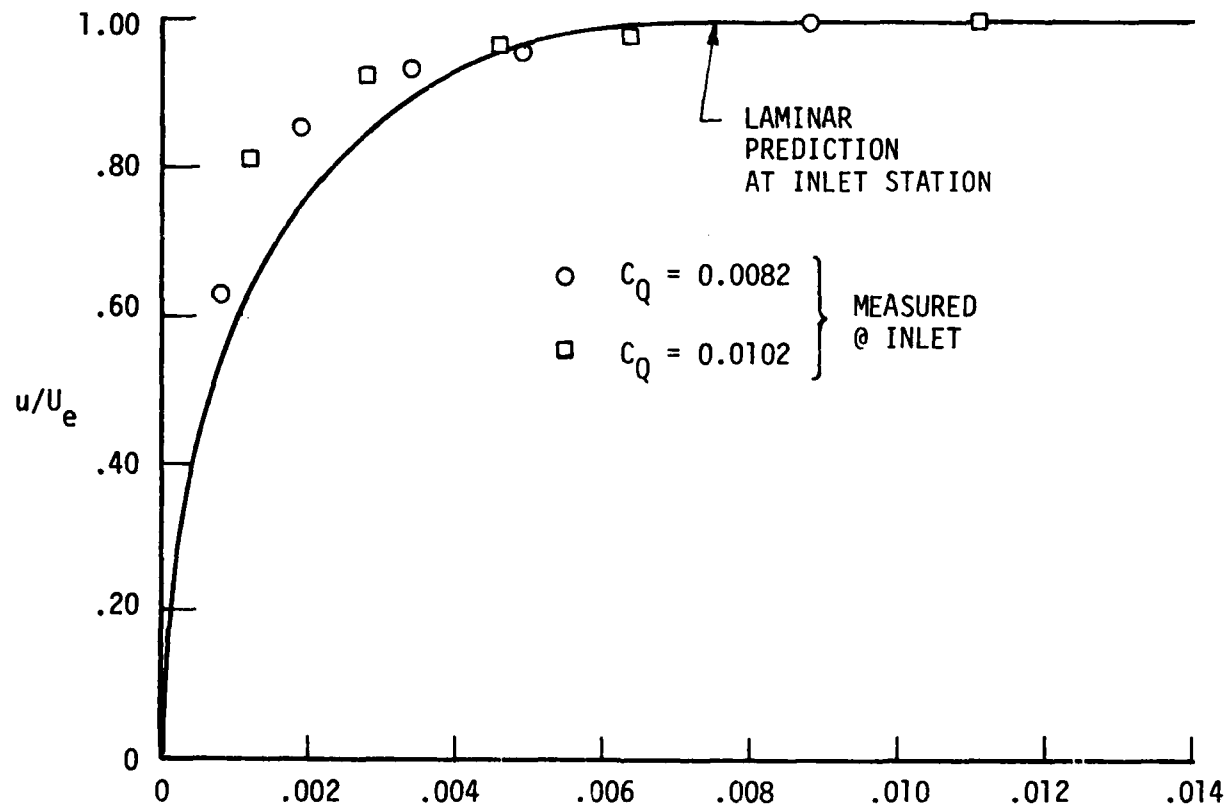
since the BLC jet was not aligned exactly with the local external streamlines. This misalignment was caused by modifying existing HDV shroud and afterbody hardware for a new jet exit location. The internal geometry resulted in the jet exiting in a nearly axial orientation.

5.2 FOREBODY BOUNDARY LAYER VELOCITY PROFILES

Forebody total pressure rakes were provided as described in Section 4.3.1. For reasons described as follows the rakes were not used on the laminar HDV and IRV models. The rakes on the turbulent ATV were installed and are discussed below.

5.2.1 Laminar Body Velocity Profiles

During the test program it was concluded that the use of any protruding probes on the forebody or centerbody at the test Reynolds numbers would trip the shroud laminar boundary layers and void the usefulness of all force measurements, either internal or external. Therefore no laminar boundary layer survey data were measured directly. However, the total pressure rakes mounted inside the inlet can be used to examine the state of the forebody boundary layer. As discussed in Section 2.2.4.1, if the total pressure recovery in the inlet is good, the total pressure distribution should be very close to that of the forebody boundary layer ahead of the inlet. There will be distortion of the velocity profile coming into the inlet due to turning and acceleration or deceleration, but the velocity distribution as a function of streamline distribution should show little change if there is no massive separation or other blockage effect just inside the inlet. This is to say that a display of measured velocity against a functional array of streamlines in the inlet provides a valid check on the state of the forebody boundary layer. Figure 5-4 shows the velocity distribution, as measured by a pitot rake in the HDV radial inlet, plotted versus the stream function across the inlet. The data are for inlet flow rates just above and just below self propulsion levels. The solid curve shows the predicted velocity distribution at the inlet for a laminar forebody boundary layer using the Polhausen approximate method as described by Schlichting.¹⁹ The agreement of the data with the prediction is sufficient to conclude that a laminar forebody boundary layer is present. In fact the data indicate a more favorable pressure gradient than predicted arising from the inlet surface curvature on the body side. These same results will be considered again in the evaluation of the radial inlet performance.



$$\frac{\psi}{V^{2/3} U_\infty} = \frac{2\pi r}{V^{2/3} U_\infty} \int_0^y u \, dy$$

FIGURE 5-4 HDV FOREBODY BOUNDARY LAYER
(As measured by inlet survey)

5.2.2 ATV Forebody Boundary Layer

The turbulent boundary layer on the ATV (due to tripping) was expected to be well behaved and the use of forebody total pressure rakes was not expected to cause significant interference with the boundary layer entering the inlet or the spillage onto the shroud. Figure 5-5 shows measured velocity profile data on the ATV at three inlet flow rates spanning the self-propulsion flow rate. The predicted velocity profile is shown for a power-law relation of $n = 5.7$ (See Table 2-1). The measured points show very close agreement with this prediction, serving to validate the artificial boundary layer tripping and the Reynolds number matching of the test conditions.

5.3 INLET PERFORMANCE

Four inlet configurations were tested, two for the laminar bodies and two for the turbulent bodies. The original HDV radial inlet was tested for comparison to existing data, and an improved submerged inlet design was tested for applications to laminar configurations. An axial/pre-diffusing inlet and a semiflush inlet were used on the ATV.

5.3.1 HDV Radial Inlet

The wind tunnel results for the HDV radial inlet are shown in Figure 5-6. It should be recalled that this inlet was designed primarily to minimize external body pressure perturbations so that laminar flow might be maintained on the forebody and the centerbody shroud. At the time the initial design was done, there was no applicable analysis methodology available for detailed internal flow behavior in this type of laminar flow inlet. Since that time analytical procedures have been developed that provide at least a partial evaluation of internal inlet flow performance (cf. 2.2.5). The predictions presented in Figure 5-6 show a large velocity overshoot on the forebody surface at the inlet plane for the flow-rate conditions achieved in the range tests and repeated here. A corresponding strong adverse pressure gradient is predicted on the inlet lip surface, such that a near-uniform velocity distribution exists across the inlet channel. The experimental data show a general agreement on the forebody surface and a good match on the internal lip surface. It should be remembered that precise experimental resolution here is difficult because of the sharp gradients. The total head pressure distribution at the

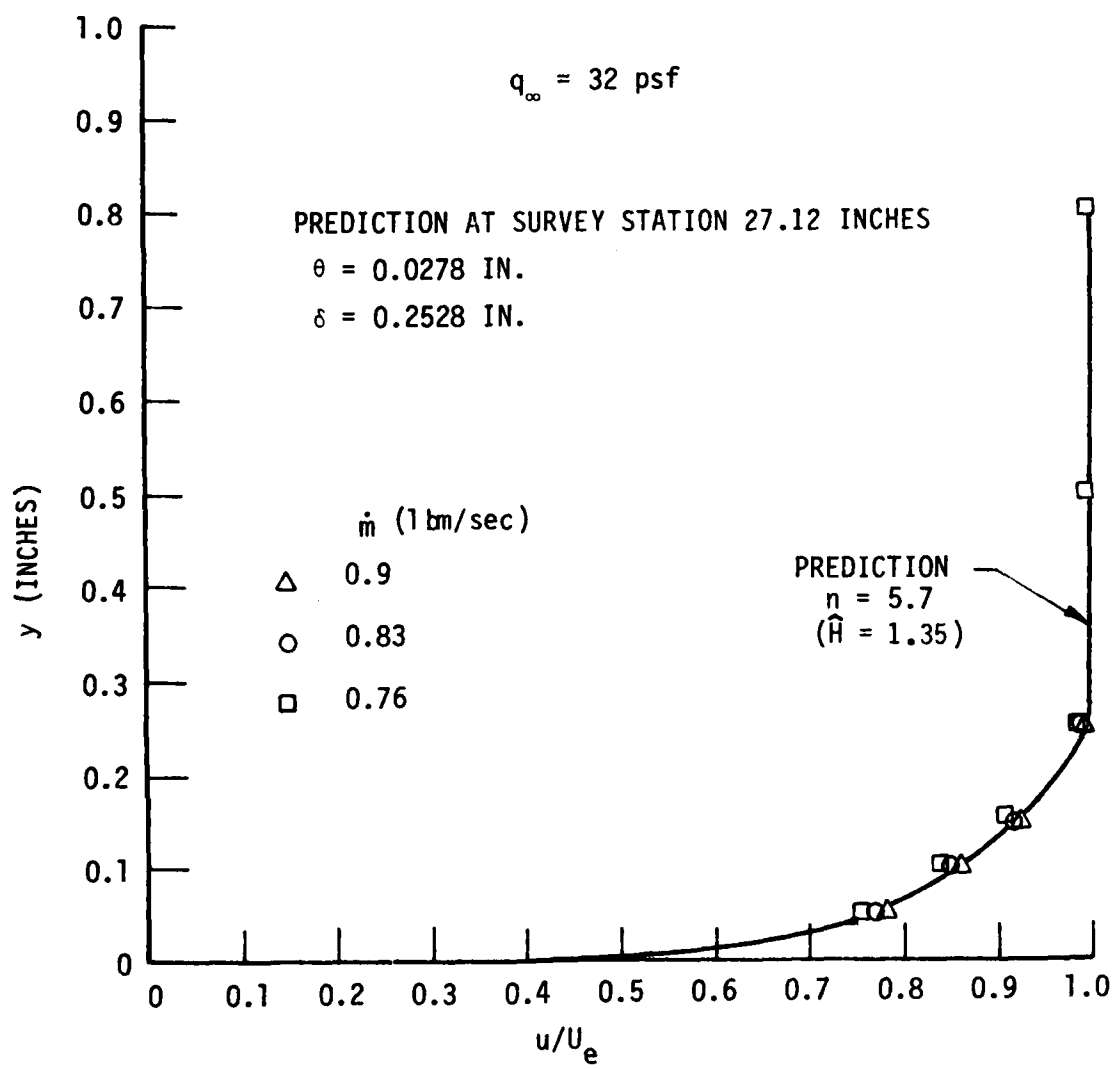


FIGURE 5-5 ATV FOREBODY VELOCITY PROFILE

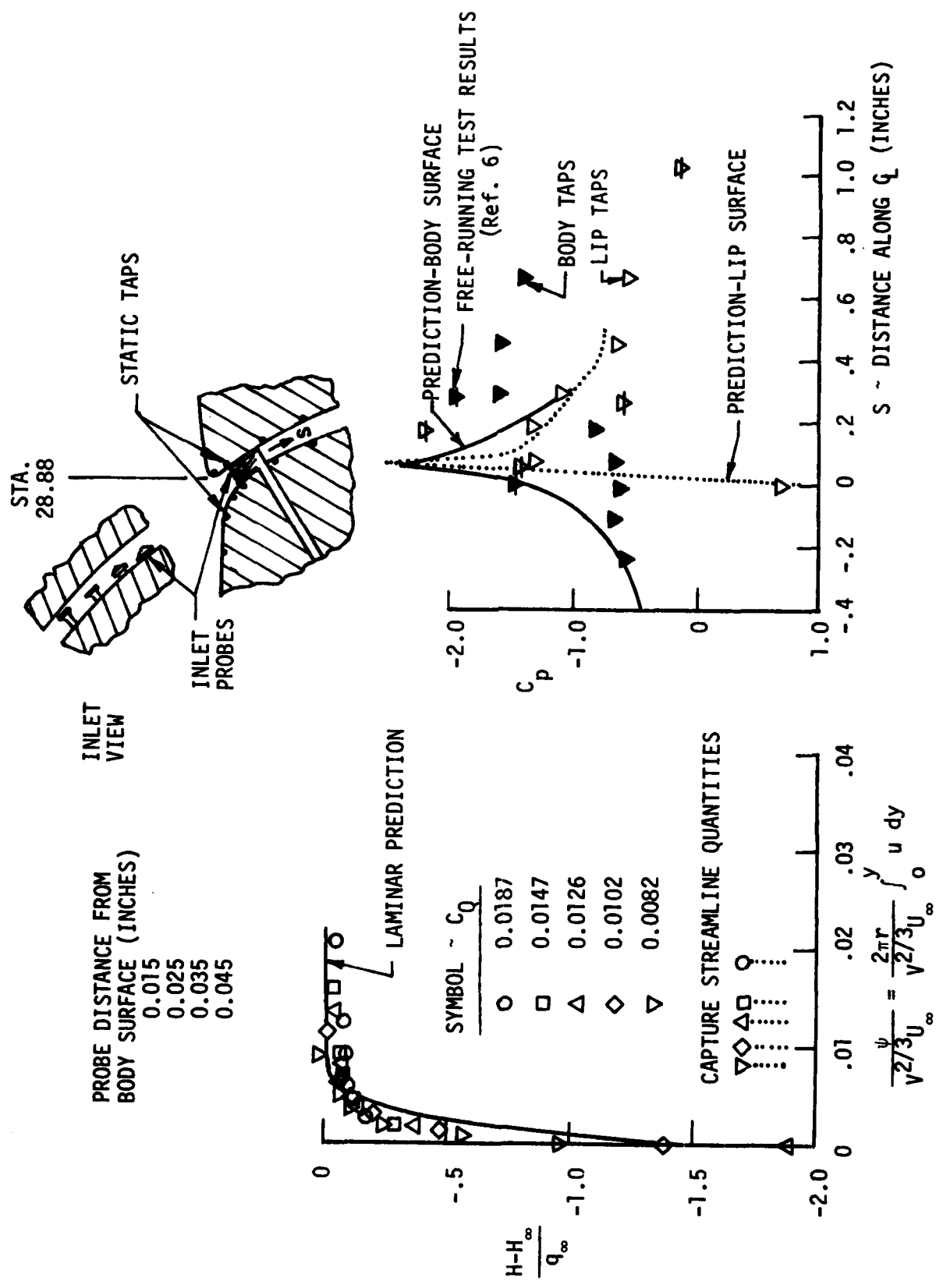


FIGURE 5-6 RADIAL INLET PERFORMANCE - HDV

inlet plane matches the predicted forebody boundary layer reasonably well, indicating that the inlet boundary layer was indeed laminar. Additionally, the designated capture streamfunction values for all C_Q 's indicate that complete ingestion of the laminar forebody boundary layer was achieved.

5.3.2 Submerged Inlet

The submerged inlet was designed to be an improvement to the radial inlet for laminar configurations. The prediction curves in Figure 5-7 show a somewhat reduced and much more restricted velocity overshoot on the inlet lip, compared to the HDV radial inlet. The forebody pressure gradient spike is also predicted to be much less severe than the radial design. However, in the inlet region, the forebody static pressure data show a reasonably strong acceleration region while the lip surface shows a retarded velocity region. The measured total head distribution for the submerged inlet shows a strong total pressure deficit near the lip surface suggesting a severe separation region. As a result the submerged inlet did not perform as expected and hence an efficient laminar flow inlet has still not been defined.

5.3.3 Axial Pre-diffusing Inlet

This inlet was designed to operate with the thick turbulent forebody boundary layer on the ATV. The forebody contour was shaped to provide some diffusion of the flow before entering the inlet. Inside the inlet the flow on the body surface accelerates slightly as the flow on the lip surface slows while developing a new boundary layer. The result is to re-shape the velocity profile and remove some of the skewness before the flow is turned. The test data presented in Figure 5-8 follow the predicted curves fairly well, even into the turning region. The total head profile was taken 0.10 inch inside the inlet and shows that pressure recovery is good with no large perturbations occurring at the lip. In general, these results confirm the validity of the design methodology quite well for turbulent-flow inlets.

5.3.4 Semi-flush Inlet

This inlet was designed to combine the best features of the axial and submerged configurations. The ram effect is retained but there is no pre-diffusion and the curvature begins immediately but ~~is~~ gradual. It was designed to

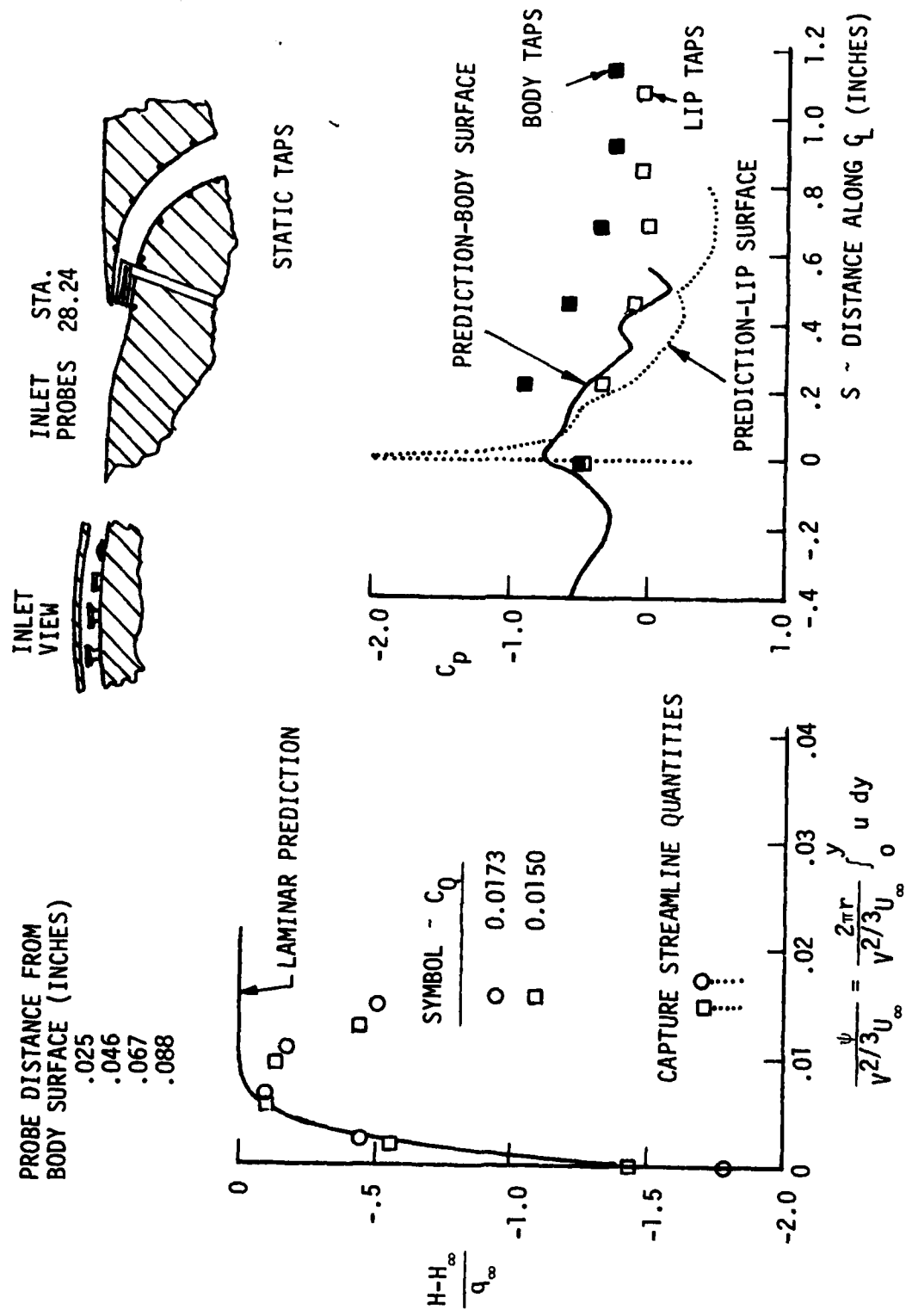


FIGURE 5-7 SUBMERGED INLET PERFORMANCE - IRV

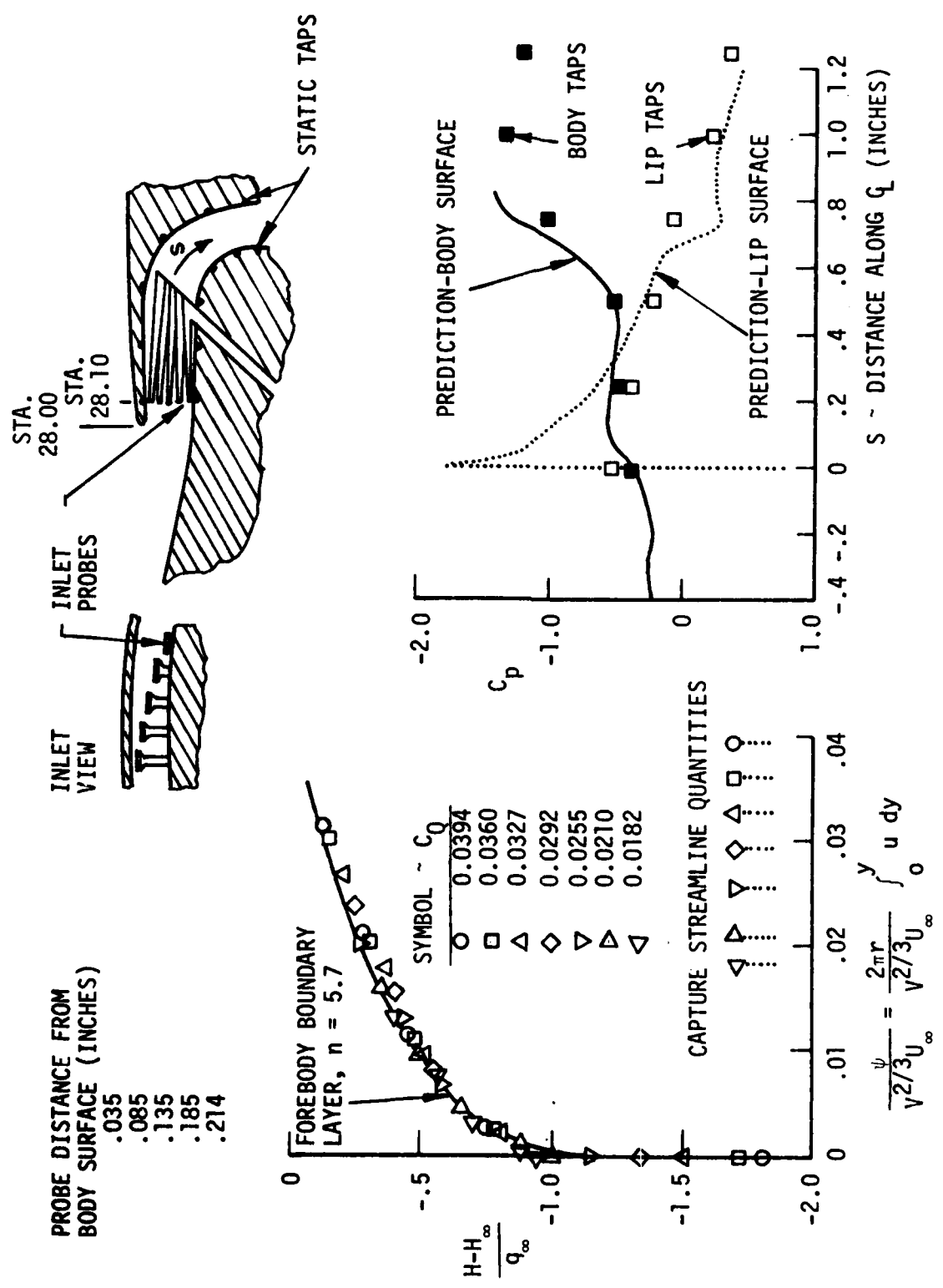


FIGURE 5-8. AXIAL-PREDIFFUSING INLET PERFORMANCE - ATv

have more tolerance to off-design operation than the axial inlet because of the larger inlet lip leading edge radius. Figure 5-9 shows how the lip pressure spike is reduced from that in the axial inlet and the relatively flat pressure distribution through the inlet. Again, the total head recovery is very good.

5.3.5 Angle-of-Attack Sensitivity

Total pressure recovery sensitivity to body angle-of-attack is addressed in Figure 5-10. The trend toward lower inlet total pressures with increasing angle-of-attack is expected from the thickening of the turbulent boundary layer on the lee side due to a change in forebody pressure gradient (See Figure 5-3). A corresponding increase in total pressure occurs at negative angles of attack due to a thinning of the boundary layer. The increased inlet blockage due to the thickened forebody boundary layer does not appear to cause any serious pressure recovery degradation over the range of angles-of-attack tested.

5.3.6 Inlet Design Methodology Assessment

An assessment of the predictive capabilities of the inlet design methodology may be made. Design of an efficient inlet for a laminar forebody such that both the upstream and downstream surfaces retain laminar flow has still not been achieved and remains a formidable challenge. Additionally, prediction of internal pressure distribution is difficult due to the small channel widths compared to the wall curvatures required for integration into a vehicle. The presence of the laminar boundary layer also requires careful attention to local adverse pressure gradients, particularly on the lip, so as to prevent poor intake pressure recovery.

Turbulent-flow inlet design, on the other hand, can be approached with some confidence using the techniques described in Section 2. Static pressure predictions appear reasonably accurate throughout the inlet region. Internal viscous turbulent mixing appears to generate a more-uniform static pressure gradient across the channel, thus implying that the turbulent flow is more forgiving to local wall curvature effects than a laminar boundary layer. Total pressure recovery is quite good for both inlet designs.

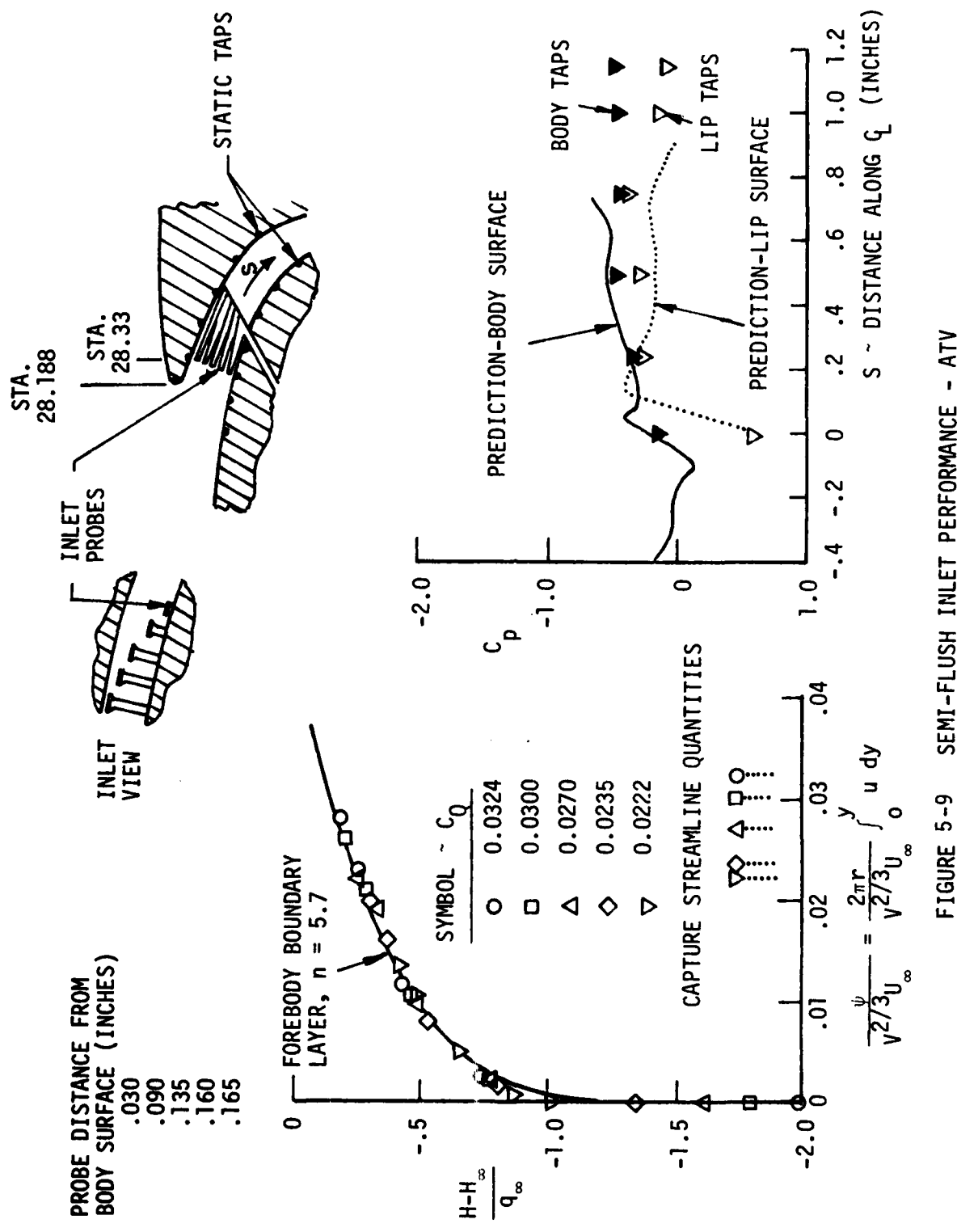


FIGURE 5-9 SEMI-FLUSH INLET PERFORMANCE - ATV

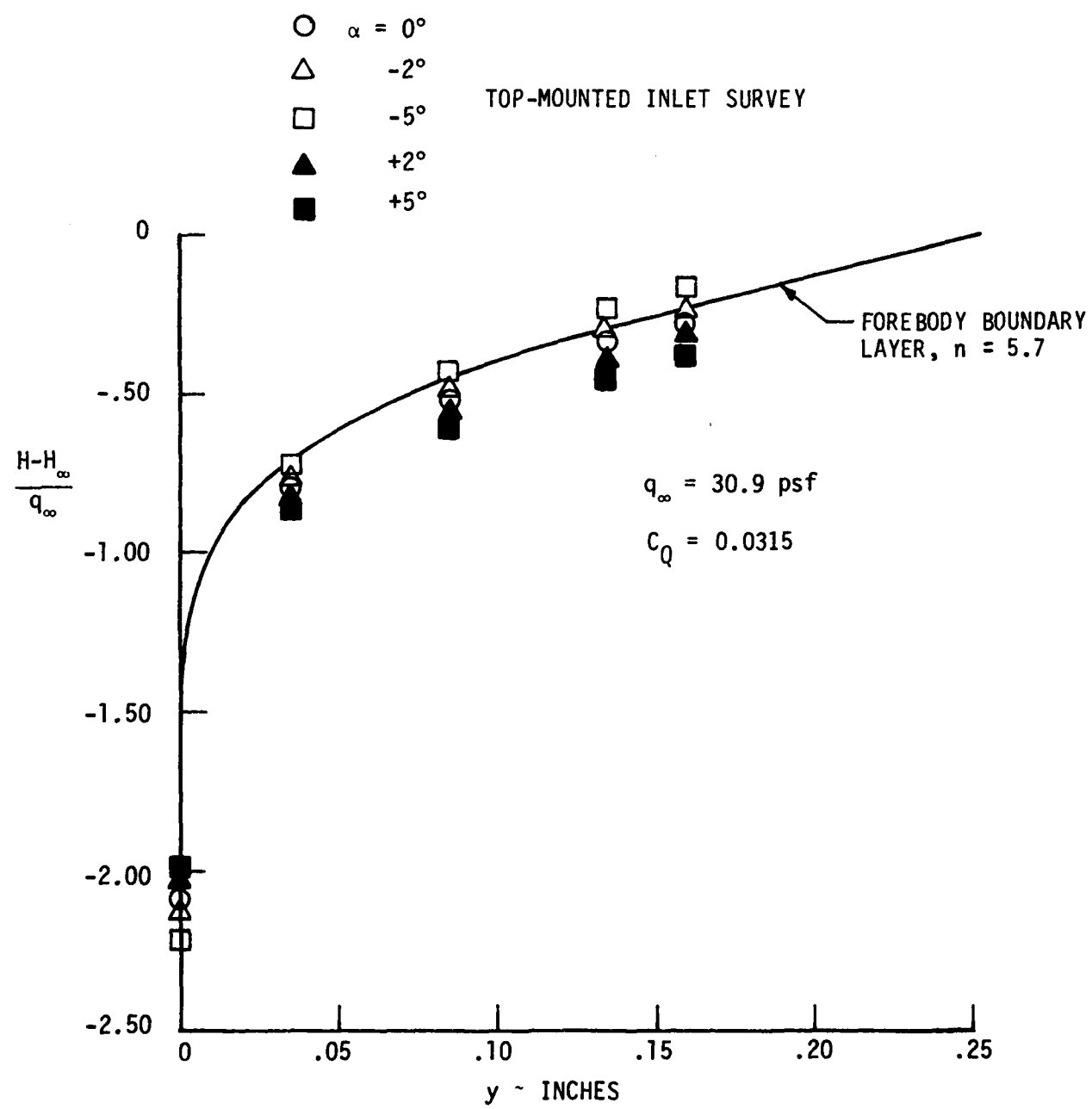


FIGURE 5-10 INLET ANGLE OF ATTACK CHARACTERISTICS - ATV/SEMI-FLUSH

The finite-difference intake design technique appears to be quite adequate for initial definition of turbulent-flow circumferential intakes. Refinements considering internal-channel viscous mixing are required to provide better static pressure predictive capability and determine intake channel total pressure losses.

5.4 BLOWING JET CHARACTERISTICS

As was discussed in Section 2.2.4 real fluid effects cause the jet nature to differ from the core flow model used in the analyses and this has an effect on the actual jet thrust produced as a function of flow rate. This section presents data that describe the nature of the blowing jet in detail and compares the measured results with analytical predictions.

5.4.1 Jet Static Pressure

The static pressure distribution across the blowing jet at the exit is not easily predictable. It is affected by curvature and boundary layer build-up inside the BLC duct and has to adjust to the external pressure field and additional curvature upon exit. The data in Figure 5-11 show that the static pressure coefficient is higher on the lip-side of the exit than on the body-side, as would be expected from curvature. There is no sensitivity to free-stream velocity, but there is a consistent flow rate dependence, approaching the potential flow level as the flow rate increases. A linear interpolation across the jet was used when calculating velocity profiles from total pressure rake measurements.

5.4.2 ATV BLC/Jet Velocity Profiles

Figure 5-12 shows the measured jet velocity profile data for the ATV at a tunnel $q_\infty = 20.7 \text{ lbs/ft}^2$. The data are plotted dimensionally as local jet velocity, u_j , versus distance across the jet exit, y , and are presented for dimensional flow rates from approximately 4 to 14 cubic feet per second. The probe measurements are seen to lie in the core of the jet flow and show a slightly skewed distribution. Assumed wall boundary layers are shown by dotted lines calculated for 1/7th power-law boundary layers at both the body and lip surfaces. The data are very consistent and display the trends

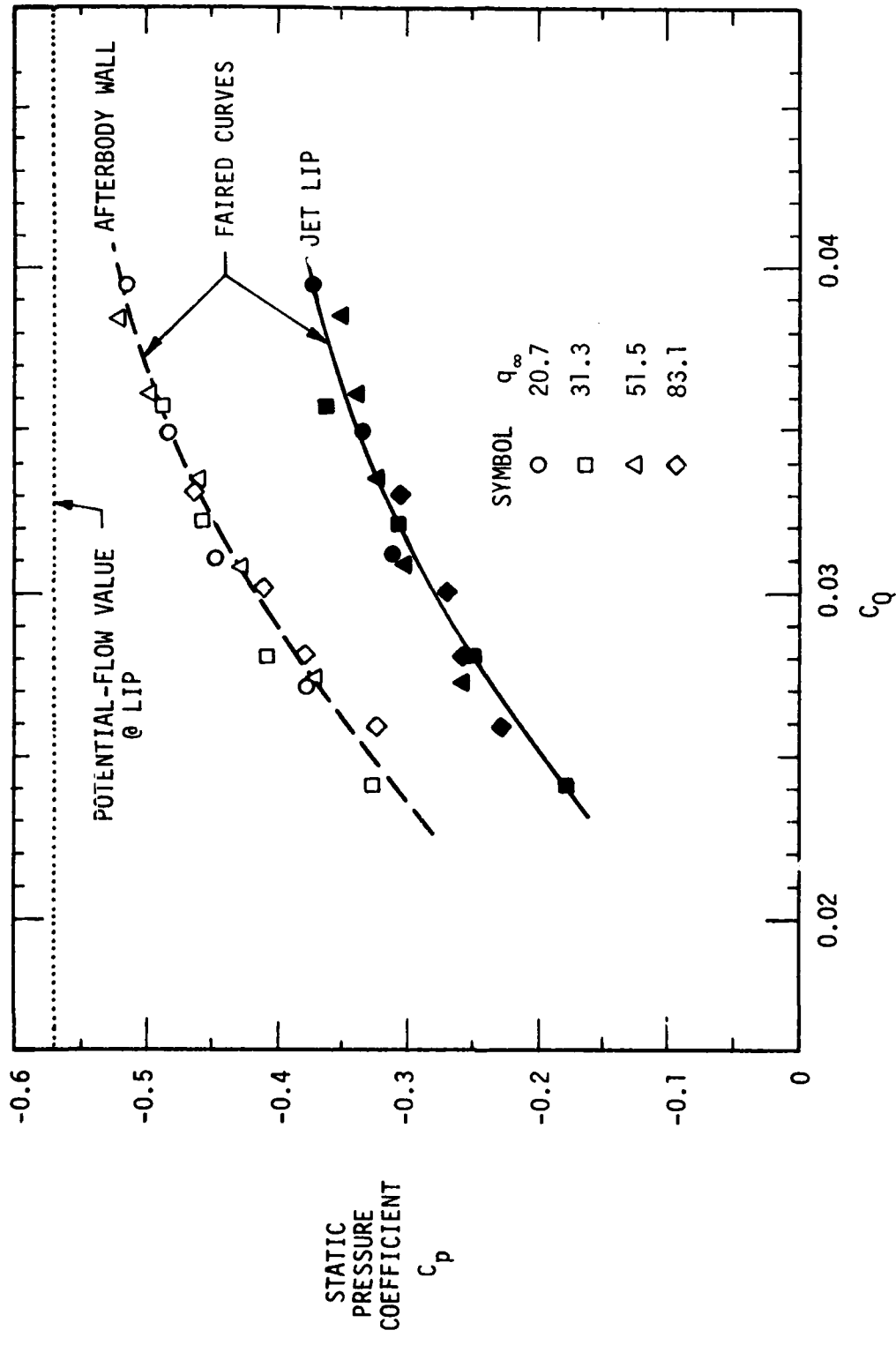


FIGURE 5-11 ATV BLC-JET EXIT STATIC PRESSURE VARIATION

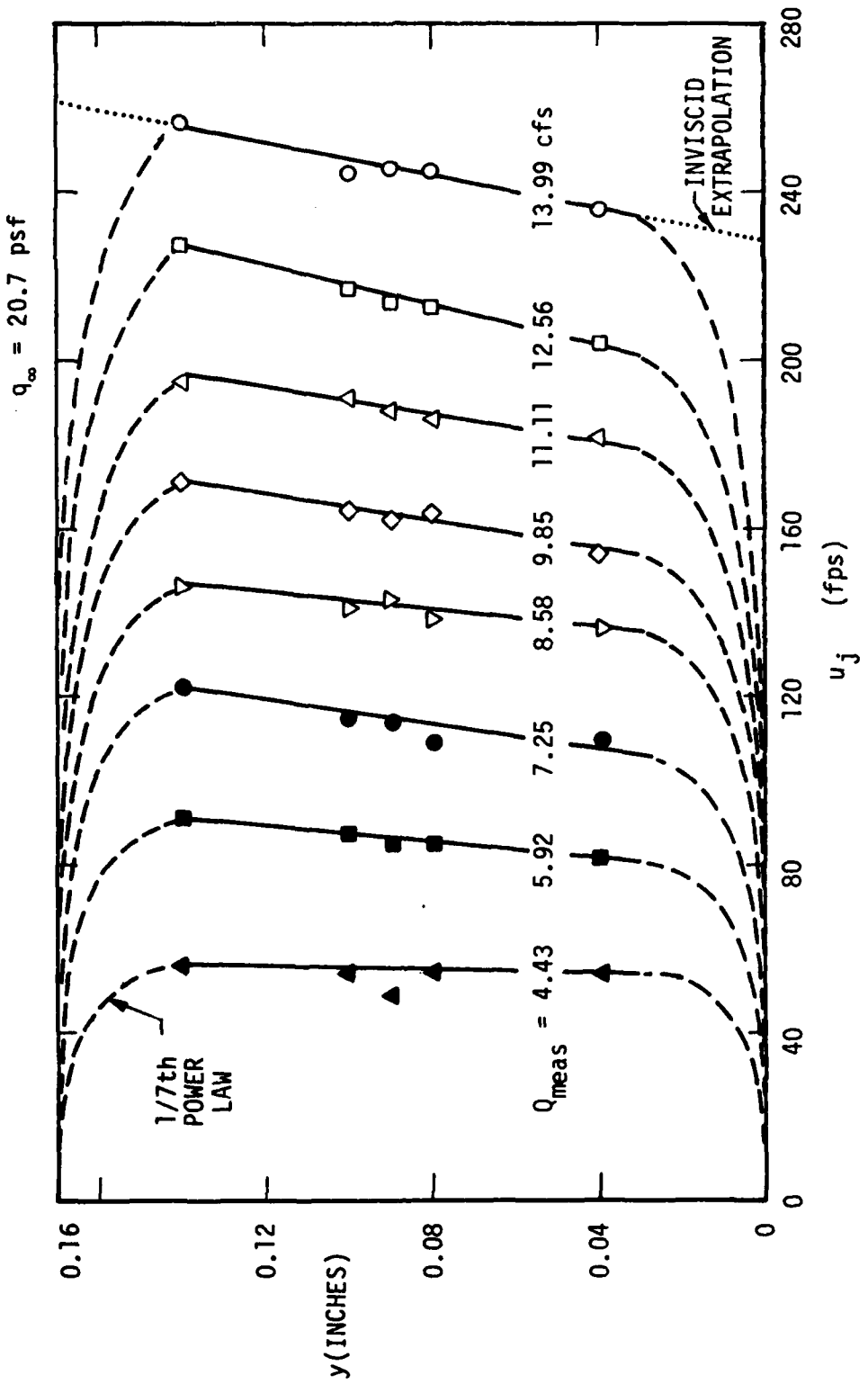


FIGURE 5-12 ATR BLC-JET VELOCITY PROFILES

expected due to the geometry and turning conditions. The velocity survey data were used in this manner, to determine jet thrust and power as a function of integrated flow rate.

5.4.3 ATV BLC/Jet Circumferential Velocity Distribution

The jet velocity profiles presented in Figure 5-12 for the ATV have one other characteristic not yet discussed. The model assemblies, consisting of actual range vehicle hardware, had a set of stators located in the blowing jet duct. There were six stators that each fitted over a main structural through-bolt to provide both spacing between the BLC duct bulkheads and streamline fairing around the through-bolts. These stators caused a local blockage in the duct that affected the exiting jet velocity as shown in Figure 5-13. In this figure the jet velocity is shown for a typical flow rate as a function of the azimuthal location. The stator locations are indicated in the figure. A survey was made under static conditions ($q_\infty = 0$) with a three-probe total pressure rake. The rake was traversed around the jet circumference to provide the data shown. It is seen that each stator location results in a low velocity segment in the jet, due to blockage. Furthermore, the flow between stators shows two velocity peaks for each segment as the flow accelerates around each stator. Jet velocity measurements, such as those shown in Figure 5-12, were taken at mid-points between stators and agreed well with the average of the circumferential distribution. Integrations of the profiles, both directly and with an integrated circumferential average, gave good agreement with direct flow meter mass flow measurements.

5.4.4 ATV Jet Viscous Blockage Factor

The viscous and jet skewness effects shown in Figures 5-12 and 5-13, have been taken into account to establish the blockage characteristics for the ATV jet. Figure 5-14 shows the viscous blockage factor, defined as

$$\lambda_v = \frac{Q_{\text{integrated}}}{Q_{\text{inviscid}}}$$

plotted versus the reciprocal of the power-law exponent for the assumed internal wall boundary layers. This correlation provides a means for determining the equivalent core-flow jet velocity from the actual flow rate and is only used with the empirical afterbody drag characteristics as discussed in

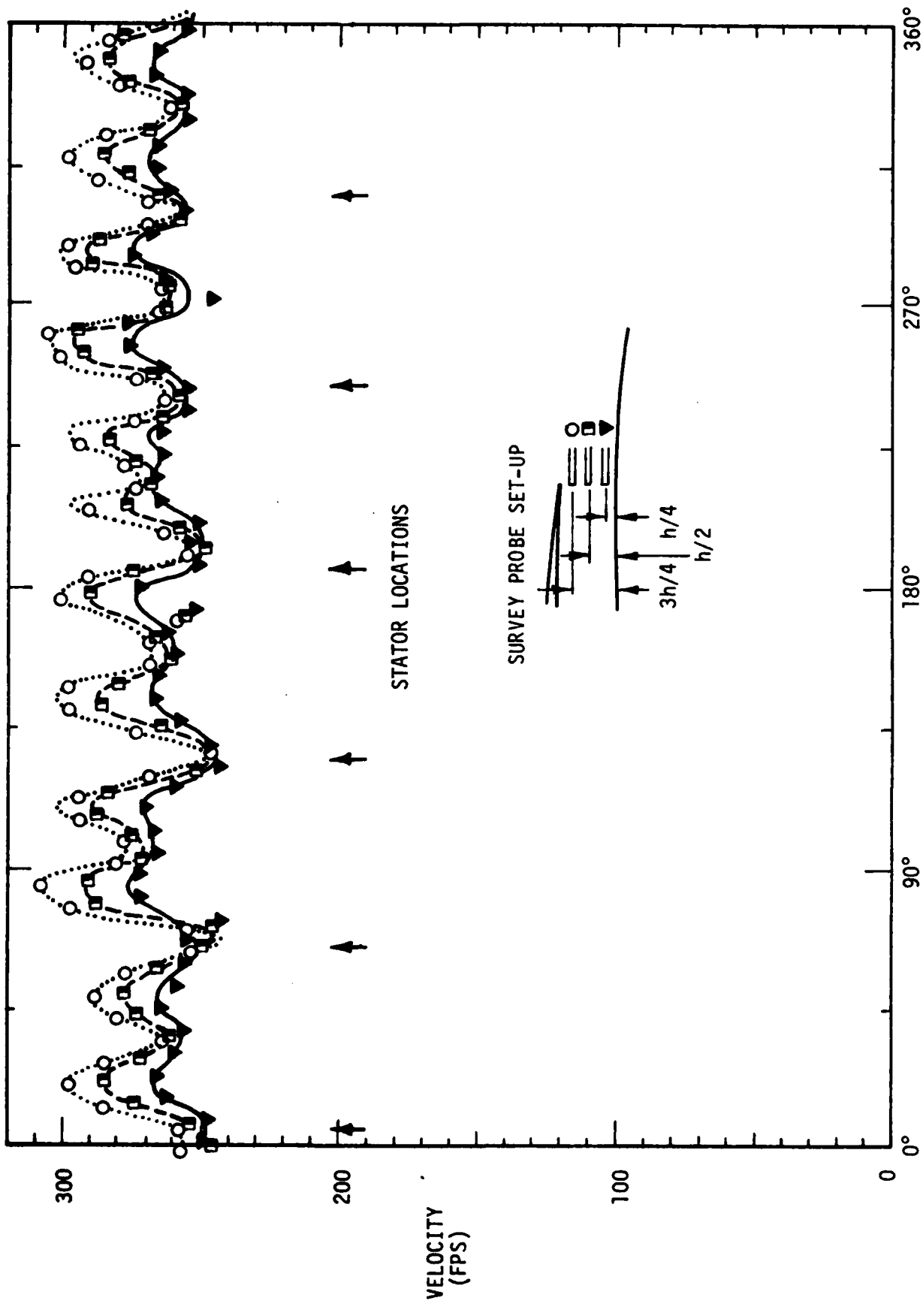


FIGURE 5-13 ATV BLC-JET CIRCUMFERENTIAL VELOCITY DISTRIBUTION

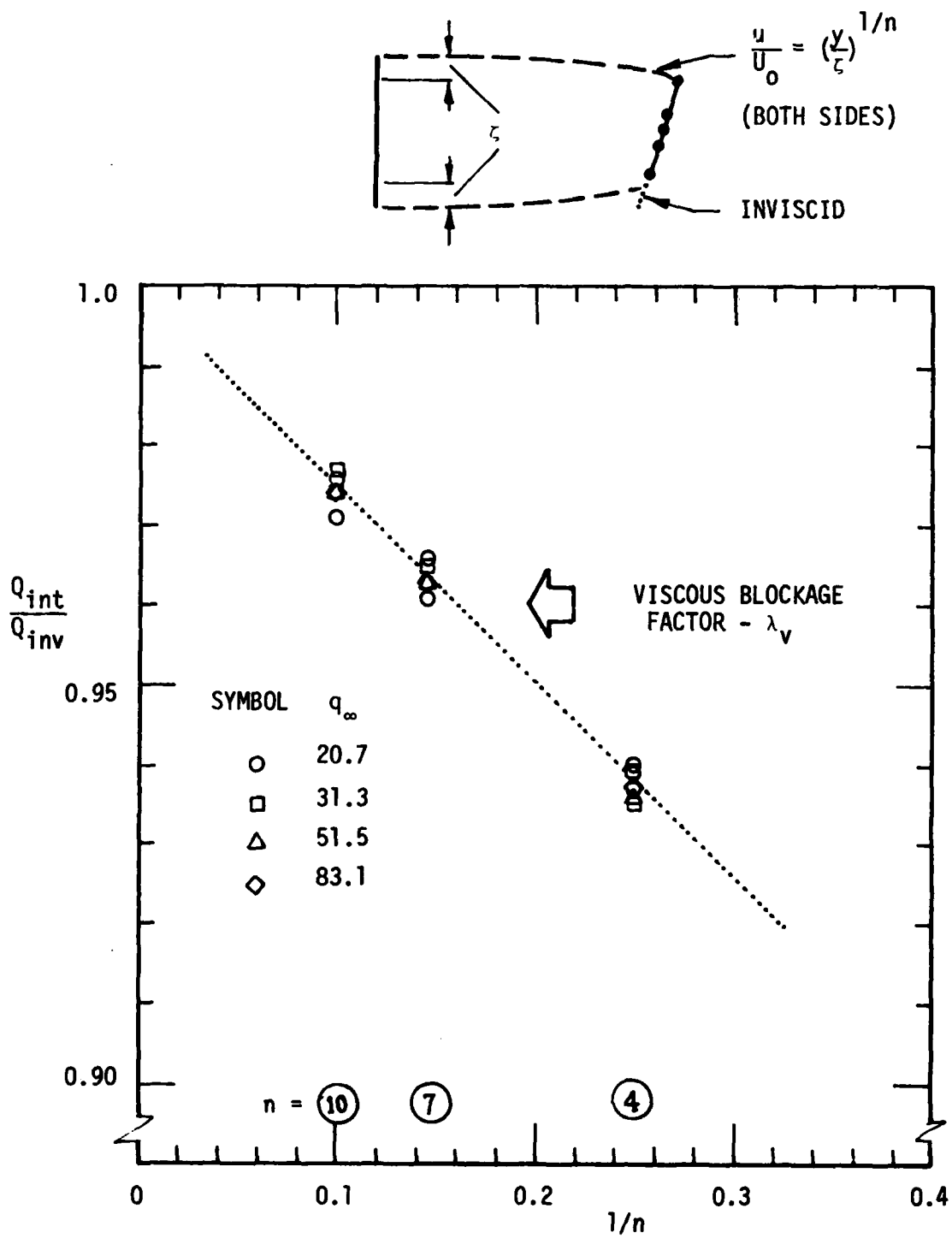


FIGURE 5-14 ATMOSPHERIC TEST FACILITY JET VISCOSITY BLOCKAGE FACTOR

Section 2.2.3. This equivalent inviscid flow rate can then be used with core-flow jet analyses (uniform velocity assumed) in the prediction of jet thrust and power. Figure 5-15 illustrates the relationship of the flow rate integrations of the jet exit survey to the measured flow rates from the orifice meters. Based on the well behaved correlation, the jet thrust and power excess could be confidently determined from integration of the jet survey information.

5.4.5 Jet Thrust and Power Characteristics

Jet thrust coefficients for the ATV are shown in Figure 5-16. The data points represent values calculated from integration of velocity profiles such as those shown in Figure 5-12 and include the real skewness effects. The integrated thrust coefficients at a given C_Q exceed predictions based on a uniform velocity at a lip $C_p = -0.57$. The deviation arises from two sources: first, the jet-exit pressure was higher than the inviscid prediction (See Figure 5-11) and second, the velocity profile exhibited a viscous nature and slight skewness (Figure 5-12). (It is a well-known fact that a non-uniform jet produces more net thrust than a uniform velocity (core-flow) jet at the same flow rate.) A similar trend for power excess also exists.

Integrated thrust coefficients for the HDV and IRV are presented in Figure 5-17. It will be noticed that the integrated thrust values for these configurations are closer to the prediction for a uniform jet velocity than was the case with the ATV. This is the result of the jet nozzle and duct producing less skewness in the velocity profile due to having a longer and more gradual jet nozzle than was available in the ATV.

Integrated jet power coefficients are presented in Figures 5-18 and 5-19. These were calculated similarly to the thrust coefficients from the same pressure rake data. The same trends are apparent, as should be expected.

5.5 FLOW FIELD SURVEYS

5.5.1 Afterbody Boundary Layer Surveys

To complete the investigation of afterbody drag characteristics a series of test runs was made with a set of total pressure rakes attached to the ATV

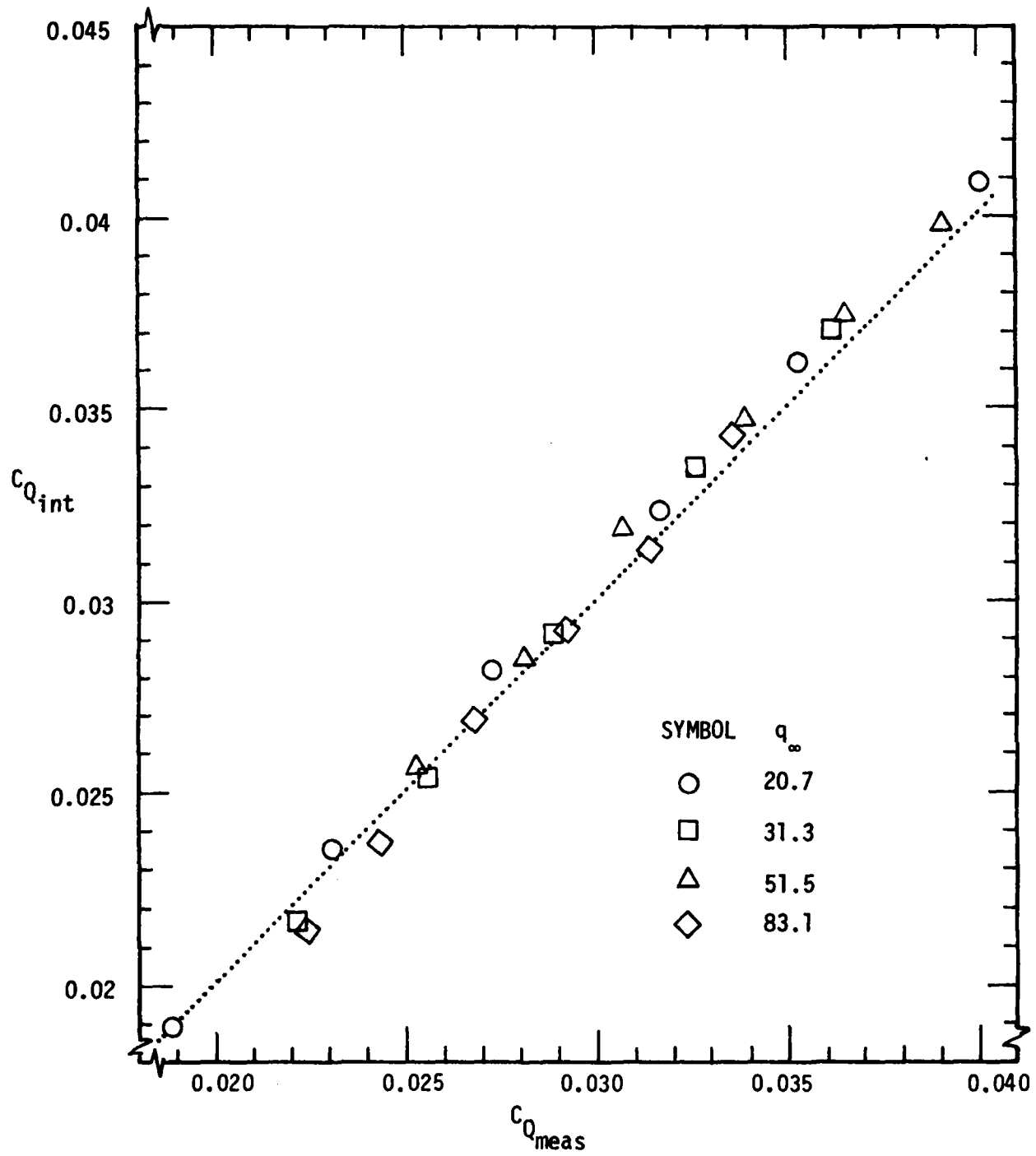


FIGURE 5-15 ATV JET FLOW RATE CHARACTERISTICS

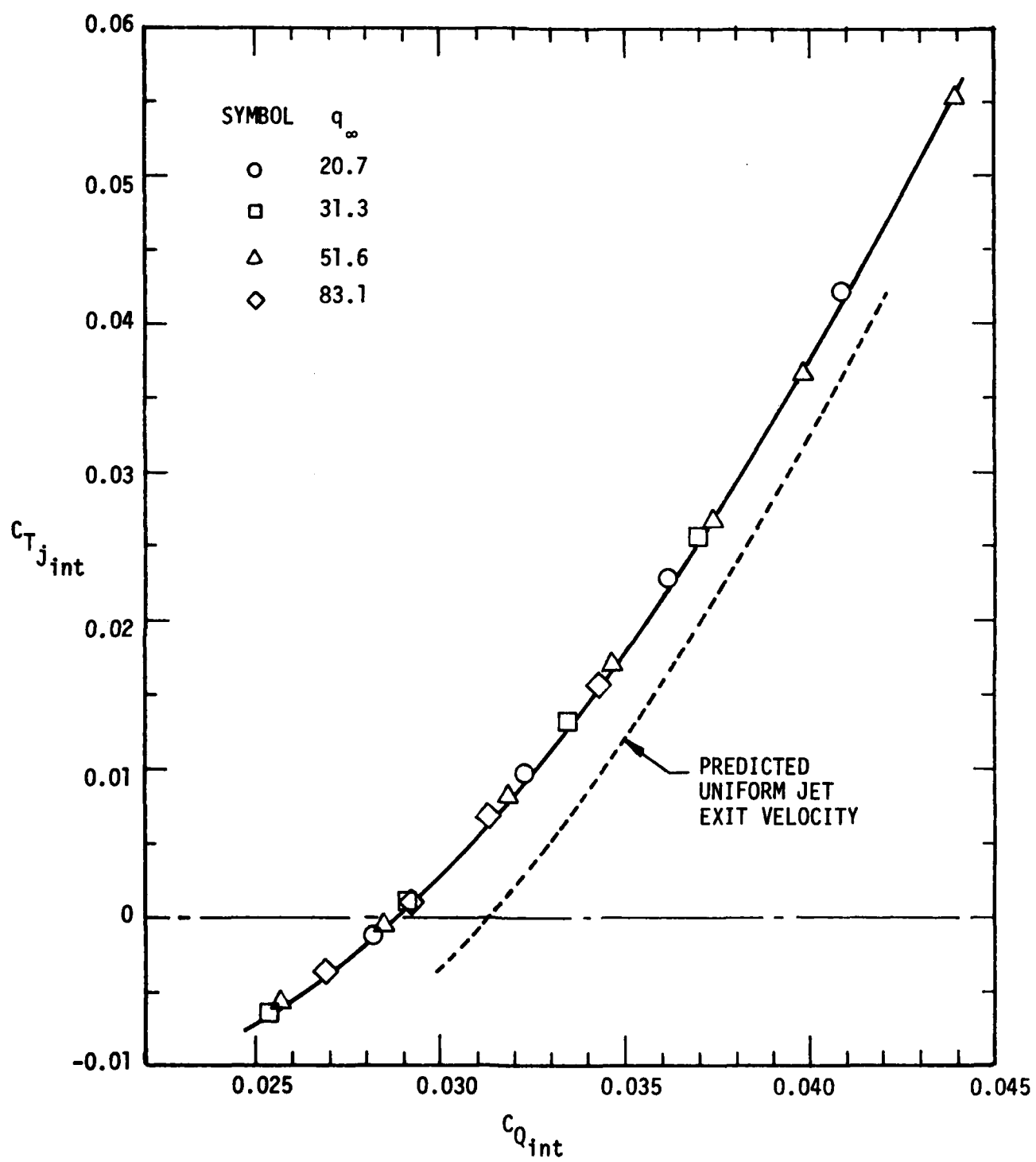


FIGURE 5-16 ATV INTEGRATED JET THRUST COEFFICIENTS

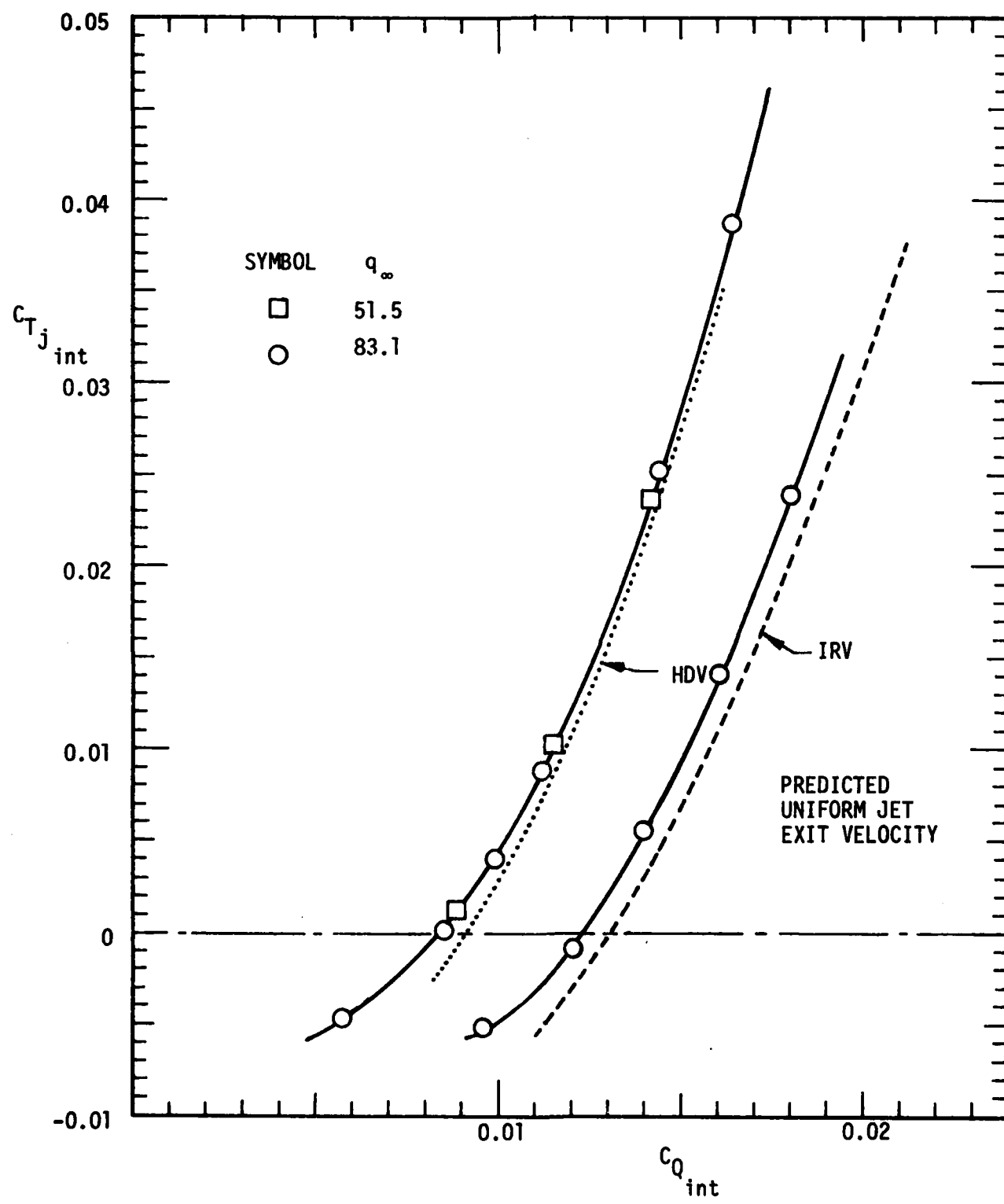


FIGURE 5-17 HDV/IRV INTEGRATED JET THRUST COEFFICIENTS

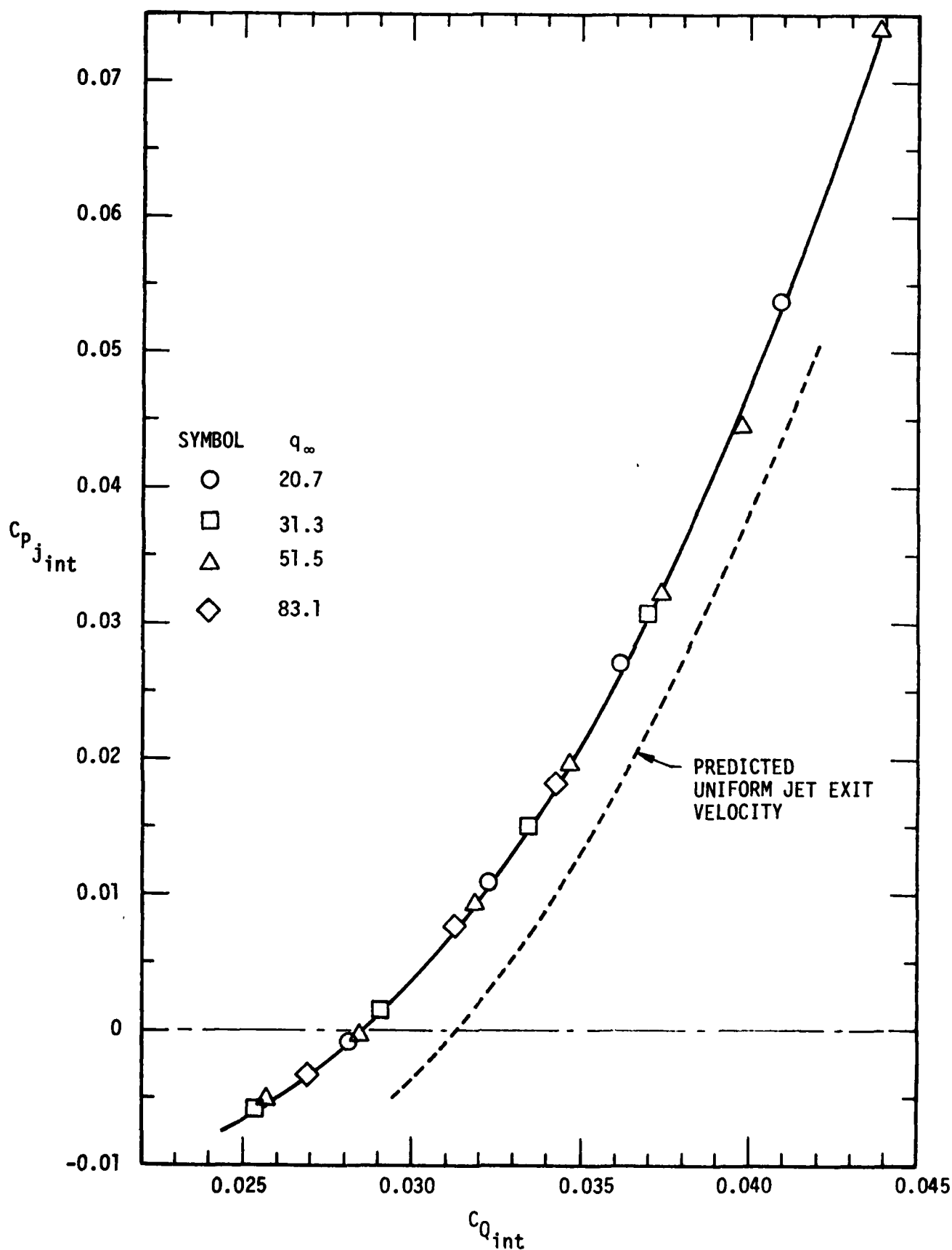


FIGURE 5-18 ATV INTEGRATED JET POWER COEFFICIENTS

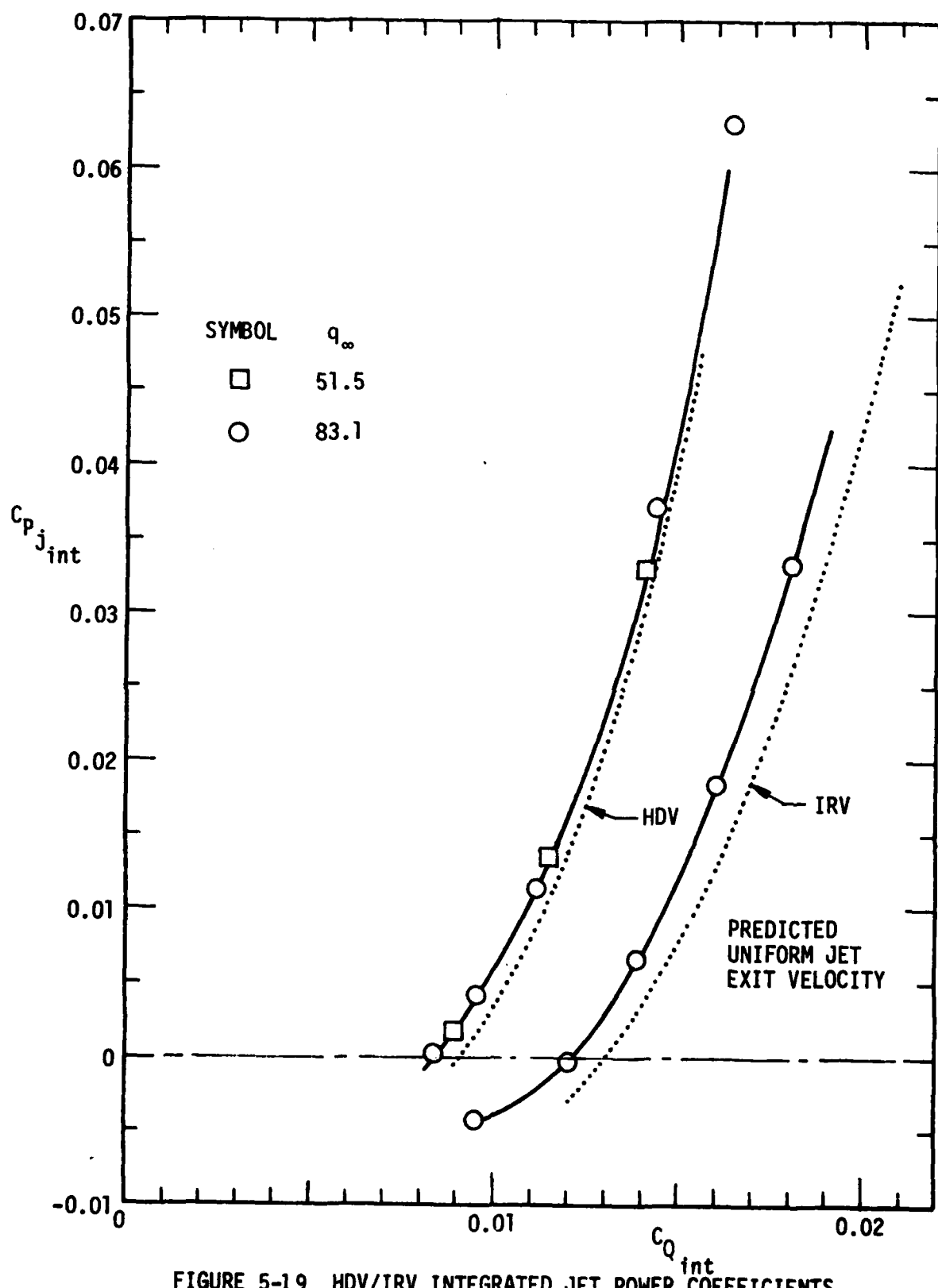


FIGURE 5-19 HDV/IRV INTEGRATED JET POWER COEFFICIENTS

afterbody as described in Section 4.3.6. Figure 5-20 presents the data from these rakes taken at a tunnel q of 31.3 psf and with blowing set for self-propulsion. Although there were static pressure probes included on several of the rakes the static pressure data were not considered complete enough to define the static pressure distribution throughout the flow field with sufficient accuracy to allow calculation of local velocities. Therefore the rake measurements are shown only as the distribution of total head through the boundary layer and along the body. It is obvious that the jet and shroud boundary layer mix rapidly in the first few inches downstream of the jet exit and the discrete nature of the jet quickly disappears. The last three surveys show an effect on the surveyed wakes of the internal blowing duct stators. Since it occurs near the body surface this deficit is actually small compared to the total head integrated cylindrically throughout the flow field, as confirmed by the far wake measurements. These results illustrate the validity of a mixing model for the afterbody flow and confirm the capability of being able to integrate the propulsive jet with the external viscous flow to provide a uniform trailing edge momentum distribution at self-propulsion conditions.

5.5.2 Far Wake Surveys

Wake pressure surveys were taken downstream of the models on all runs. A sample of the data is shown in Figure 5-21. This run was made with the bare-body ATV at zero angle-of-attack and at a tunnel dynamic pressure of 30 psf. The first survey is at a condition of overblowing ($T > D$) and illustrates the residual excess momentum in the wake as shown by the high total pressure in the core. The second survey was at a blowing rate very near but just below that for self-propulsion, as verified by the small total head deficit. The other surveys were taken at successively lower blowing rates and clearly show the build-up in momentum deficit as thrust decreases. The survey data were integrated cylindrically to obtain the total wake momentum deficit or excess from which the net axial body force was calculated. The agreement between the

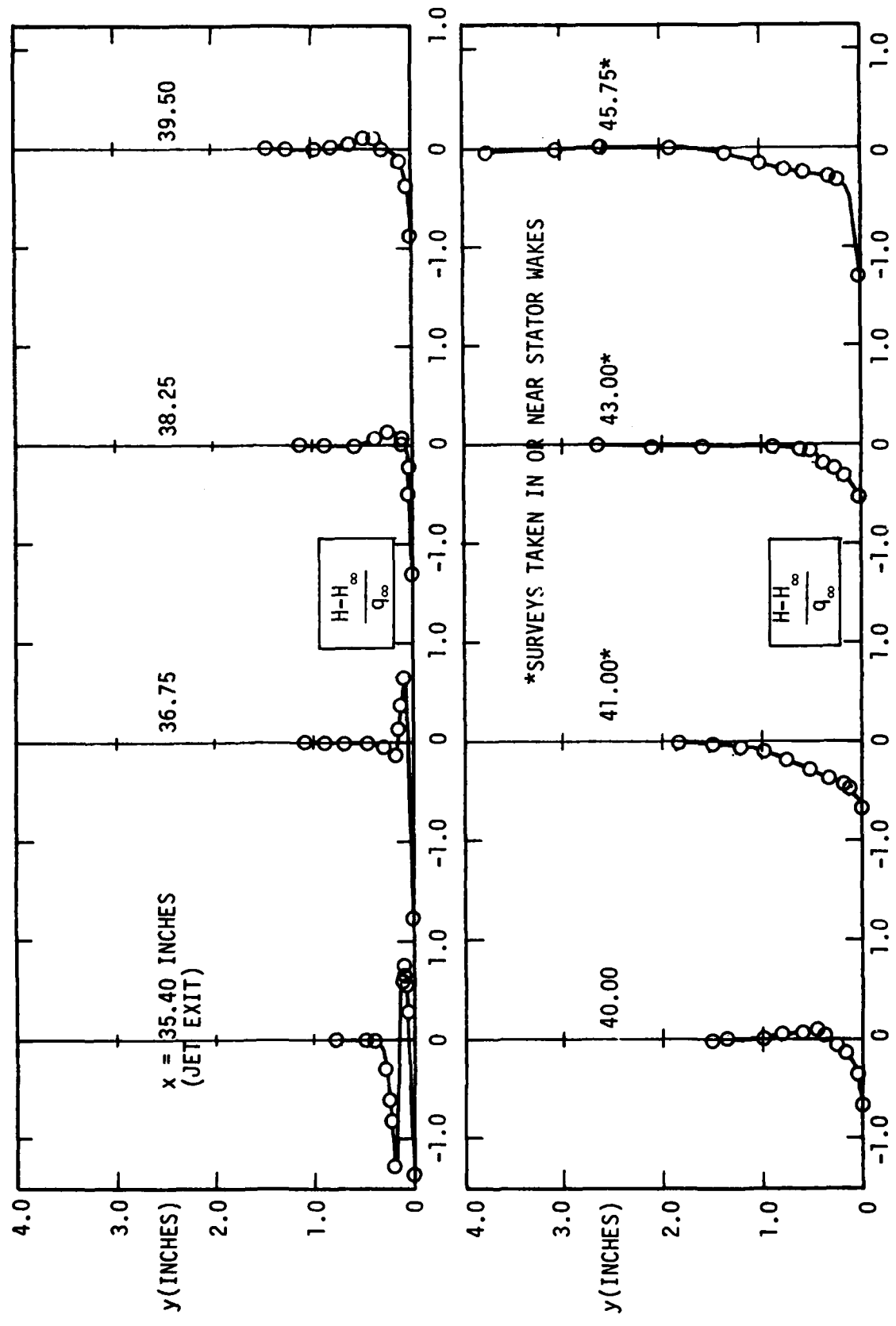


FIGURE 5-20. ATV AFTERBODY FLOW FIELD TOTAL HEAD SURVEYS

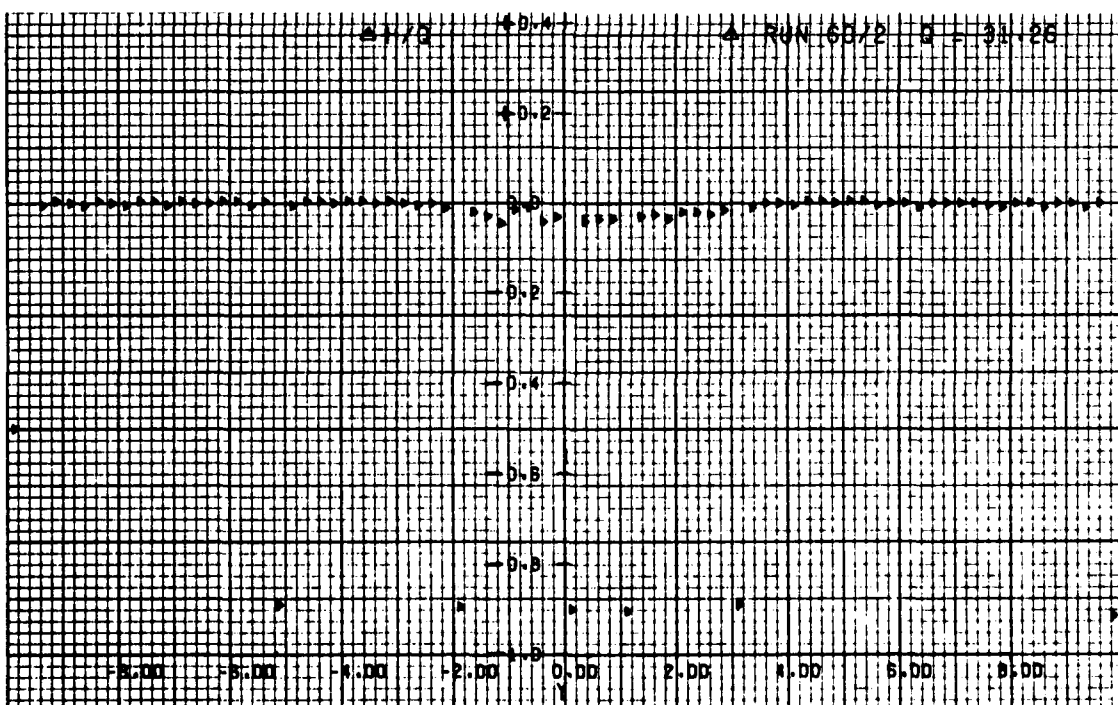
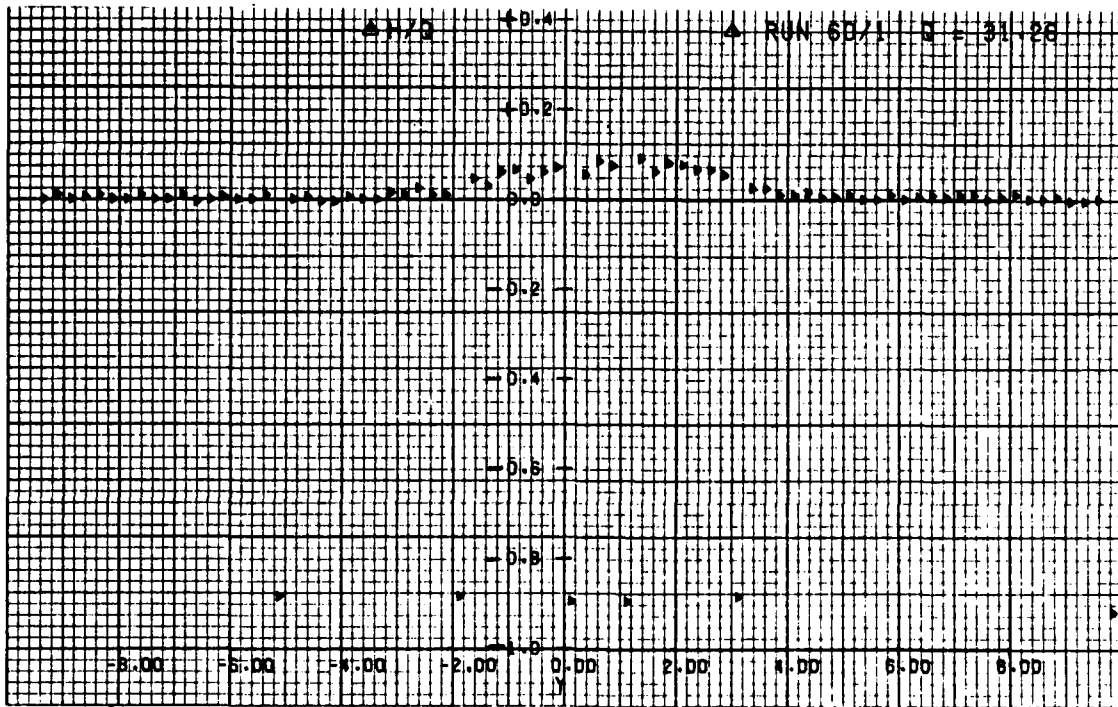


FIGURE 5-21(a) AFTERBODY FLOW FIELD SURVEYS

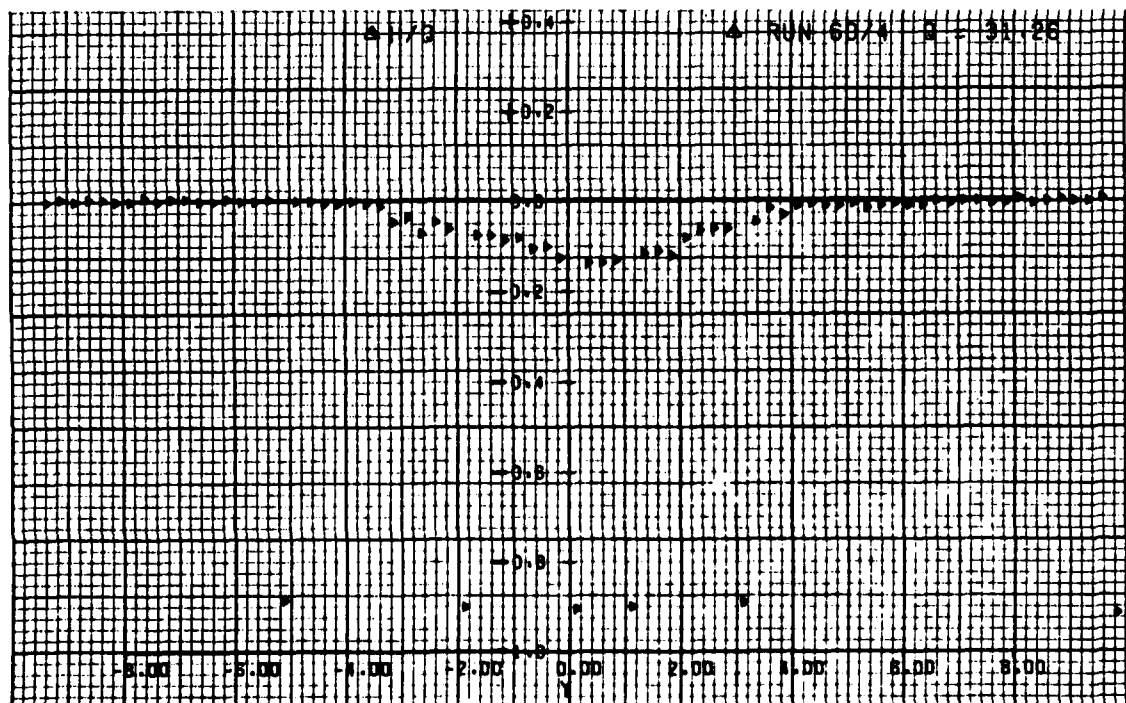
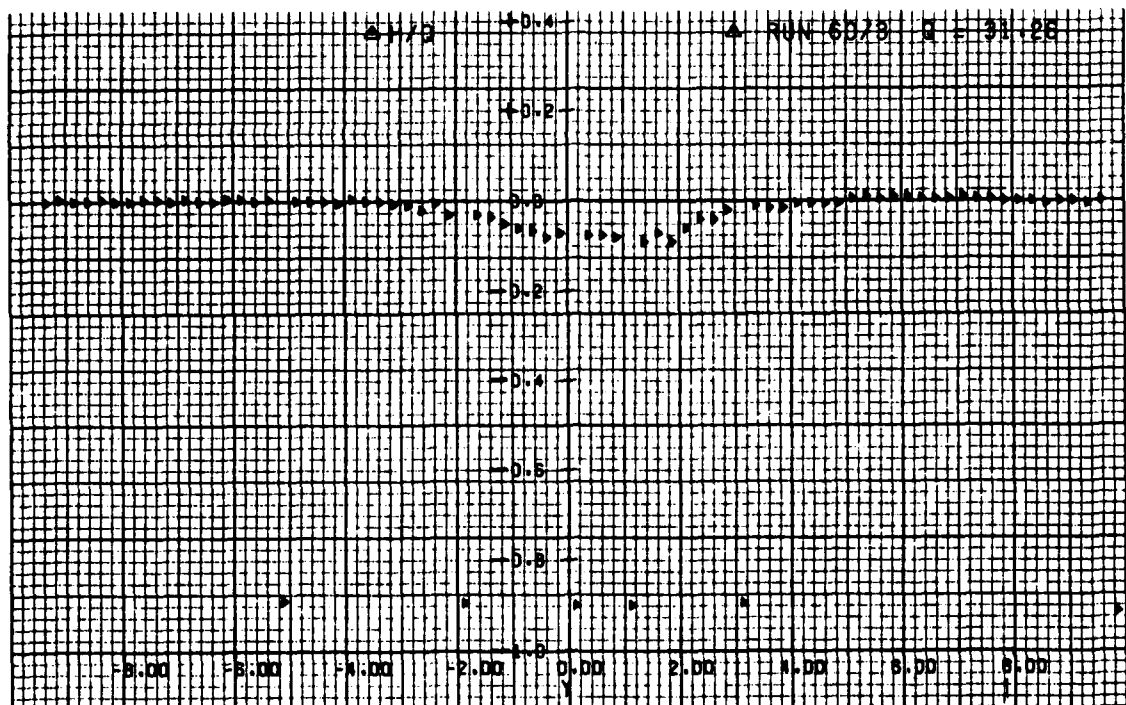


FIGURE 5-21(b) AFTERBODY FLOW FIELD SURVEYS

wake rake results and the measured balance forces was always very good, as will be shown in Figures 5-23 and 5-24.

5.6 SELF-PROPULSION DETERMINATION

The condition of self-propulsion for a powered model configuration in a wind tunnel is obviously achieved when the net force is zero. In the case of a BLC propulsive afterbody, this condition occurs when sufficient jet thrust is supplied to overcome the vehicle drag. Coincident with supplying the jet thrust, an equal mass flow must be ingested into the inlet to assure an accurate simulation of vehicle operating conditions. If the model could be suspended in the tunnel without any support effects, the self-propelled condition would occur when the internal balance read zero axial force (at zero angle-of-attack). Wake rake measurements can also be used to determine self-propulsion if a sufficiently large region of the wake is surveyed. This is extremely difficult if fins or other protuberances are present without employing an extensive number of pressure probes. Wake rake information is extremely useful, however, to verify self-propulsion for symmetric configurations (body-only). For this reason, balance data was used throughout this report to evaluate net resultant model forces, with wake rake measurements providing verification, particularly in determining strut interference tares.

5.6.1 Support System Tare Forces

Pressure-induced tare forces on the dual-flow bellows assembly were calibrated statically with the inlet and BLC jet sealed and the tunnel not running. Strut interference tare forces were evaluated through the use of an image strut and verified with far-wake pressure rake surveys.

5.6.1.1 Dual-flow Bellows Tares

The dual-flow bellows assembly, with the force balance in place, was calibrated for tare effects on force measurements due to pressure and vacuum loadings on the blowing and suction ducts respectively. Each duct was sealed separately and the appropriate pressure or vacuum was applied while the other duct was vented to atmosphere. The calibration results are given in Figure 5-22. The difference between indicated force and applied force was typically less than \pm 1.00 percent. The force balance calibration was checked several

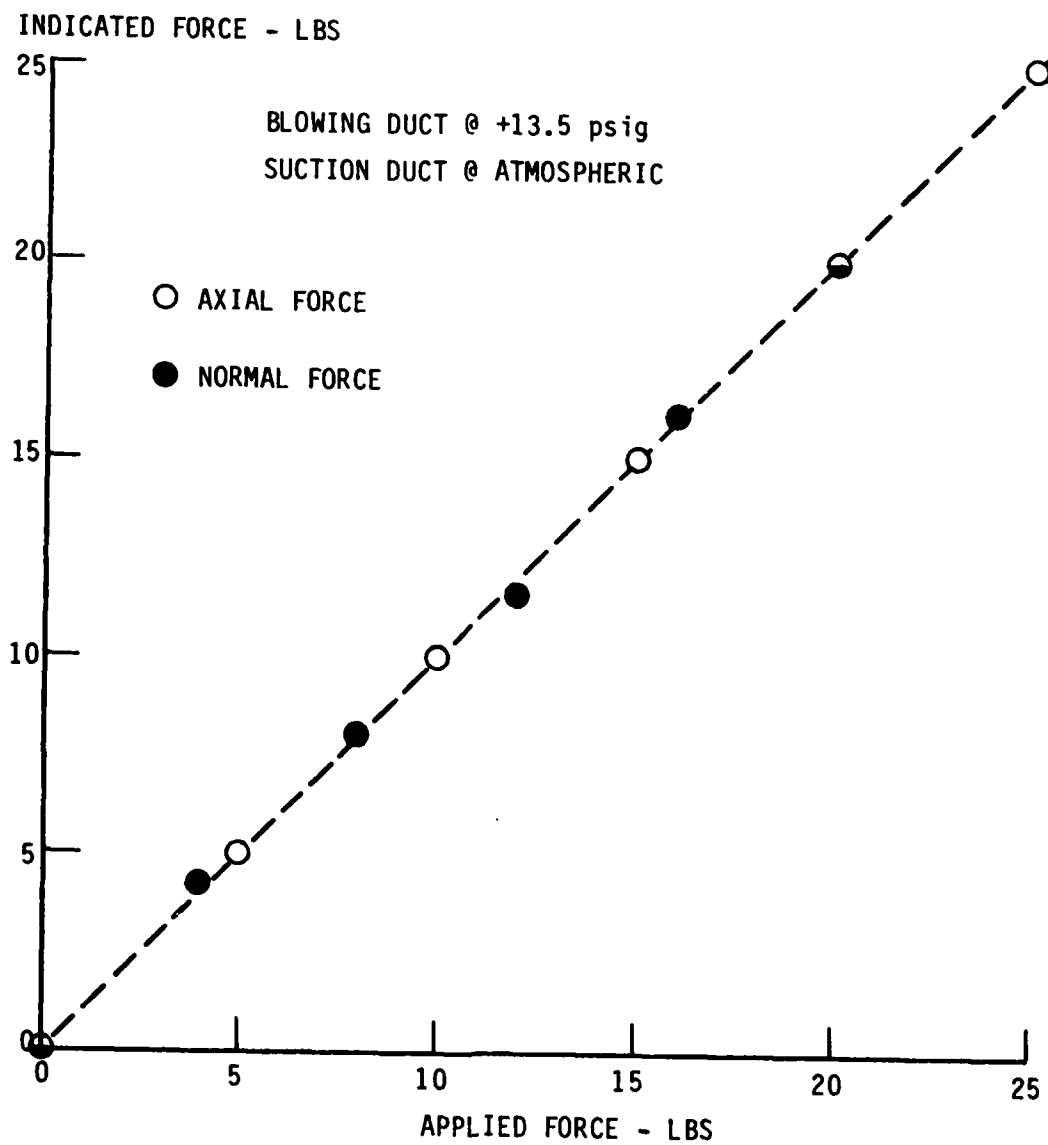


FIGURE 5-22(a) BELLows TARE FORCES

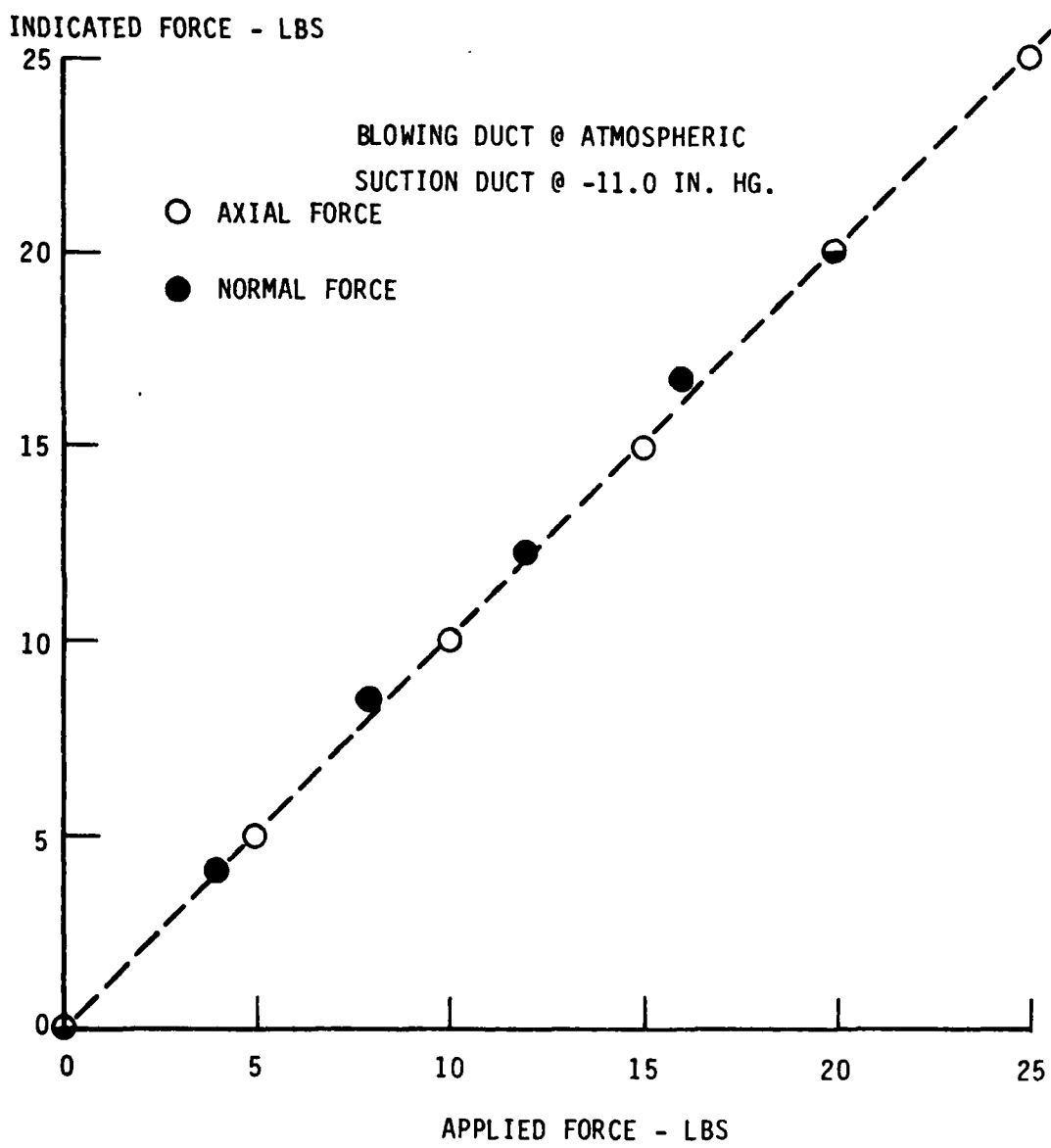


FIGURE 5-22(b). BELLOWS TARE FORCES

times before, during, and after the test series and all calibration results were within ± 0.50 percent.

5.6.1.2 Strut Interference

Although the models were mounted to float free of the mounting strut, the strut's presence still caused an interference effect in the force measurements because of the absence of a portion of the vehicle forebody exposed to a favorable pressure gradient and the pressure field generated by the strut itself. All axial force measurements presented here have been corrected for strut interference. The procedure was to record force data over the full range of test conditions both with and without an identical image strut mounted opposite the support strut and fixed to the mounting installation. The incremental force difference on the model between an installation with one strut and an installation with two struts was taken to be the interference effect of a single strut. This force increment was then subtracted from all data taken with the single mounting strut to infer the force that would be felt by the model if no struts were present.

Suction was applied to the struts to remove the strut boundary layers to minimize the effect of the strut wake washing over the model. Strut suction flow rate was varied to find the optimum suction rate for minimum total interference with the model axial force. For the turbulent ATV configuration, strut suction was found to have a negligible effect and was unnecessary. For the laminar flow HDV and IRV configurations strut suction proved to be only important for maintaining laminar boundary layers on the forebody and shroud and was maintained at appropriate levels for each test condition (≈ 0.6 lbm/sec). As expected strut suction did not seem to affect the pressure-generated interference forces.

The results of the strut interference test for the ATV (body-only, no fins) are shown in coefficient form in Figure 5-23. Force data were taken over a range of tunnel dynamic pressure from about $21 \text{ lbs}/\text{ft}^2$ to $83 \text{ lbs}/\text{ft}^2$ and a range of model flow rates that bracketed the predicted self-propulsion levels. Open symbols in the figure denote data with both the image and support struts present. Closed symbols denote data for the support strut only. The dotted curve represents the difference between the two sets of data applied as a correction to the support-strut-only data and is taken to be the axial force characteristic of the configuration as a function of BLC flow

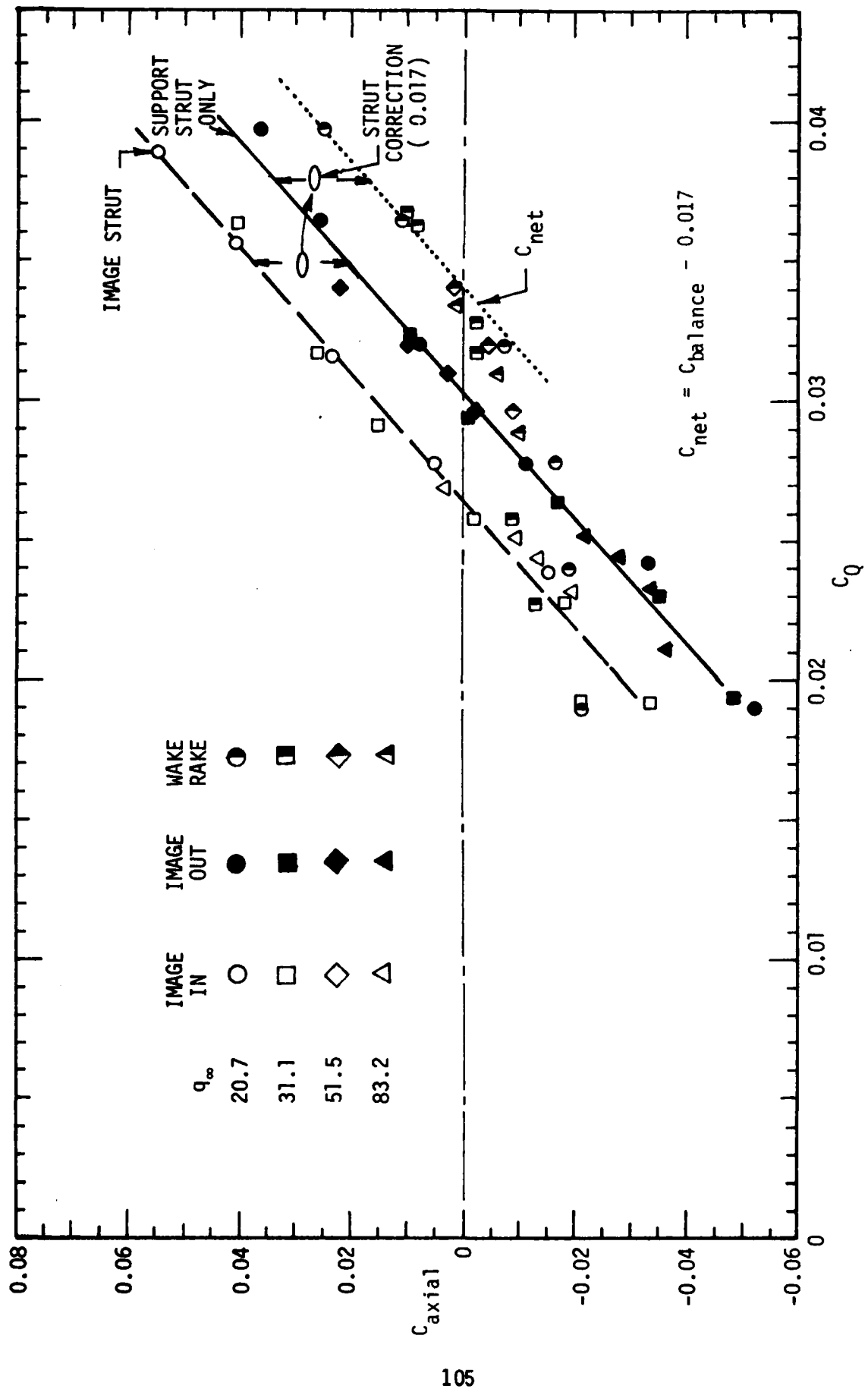


FIGURE 5-23 ATV STRUT INTERFERENCE/WAKE RAKE COMPARISON

rate. Verification of the accuracy of the interference correction is provided by data from far-wake total pressure surveys (half-shaded symbols) from which net force was determined by integration of the wake momentum deficit or excess. Agreement is seen to be quite good at conditions from slightly below to well above self-propulsion levels where the model wake is centered and well defined.

Similar results are presented in Figure 5-24 for the HDV configuration with fins at a tunnel q_∞ of 83 lbs/ft², which matches a portion of the freerunning range test data base. The strut interference correction is seen to be equally as good and of the same value as for the ATV.

5.6.2 Self-propulsion Thrust Requirements

Net axial force coefficients (corrected for support strut and bellows tares) for the ATV configuration at freestream dynamic heads of 20.7 and 31.2, the HDV configuration at 83.2, and the IRV at 83.2 are presented in Figures 5-25 thru 5-28 respectively. The intercept point at $C_{net} = 0$ determines the self propulsion flow rate $C_{Q_{sp}}$ which in turn is used to evaluate jet thrust and power requirements. Near self-propulsion all configurations are reasonably well behaved so that the interpolation can be accurately performed.

The thrust required for self-propulsion represents the single most important quantity that characterizes the BLC-propulsive afterbody performance, since it encompasses all aspects of the concept including afterbody drag, shroud momentum deficit energization, and fin effects. Thrust coefficients for each of the vehicle configurations are presented in Figure 5-29. Both measured values (Figures 5-16 and 5-17) and core-flow predictions (Figure 2-16) are provided. The symbols on each curve represent self-propulsion conditions. Although the equilibrium thrust occurs at different flow rates, an effect discussed previously in Section 5.4, the agreement between prediction and experiment is excellent for all configurations.

A review of the prediction methodology candidates, described in Table 2-2, is shown in Table 5-1 with comparisons to measurements in the wind tunnel and clearly illustrates the validity of the mixing model. The non-mixing hypothesis ignores a fundamental aspect of the BLC-propulsive afterbody that accounts for a 50 percent reduction in jet thrust required for the ATV and over an 80 percent decrease for the IRV. Use of a non-mixing afterbody drag model would obviously lead to considerably misleading results.

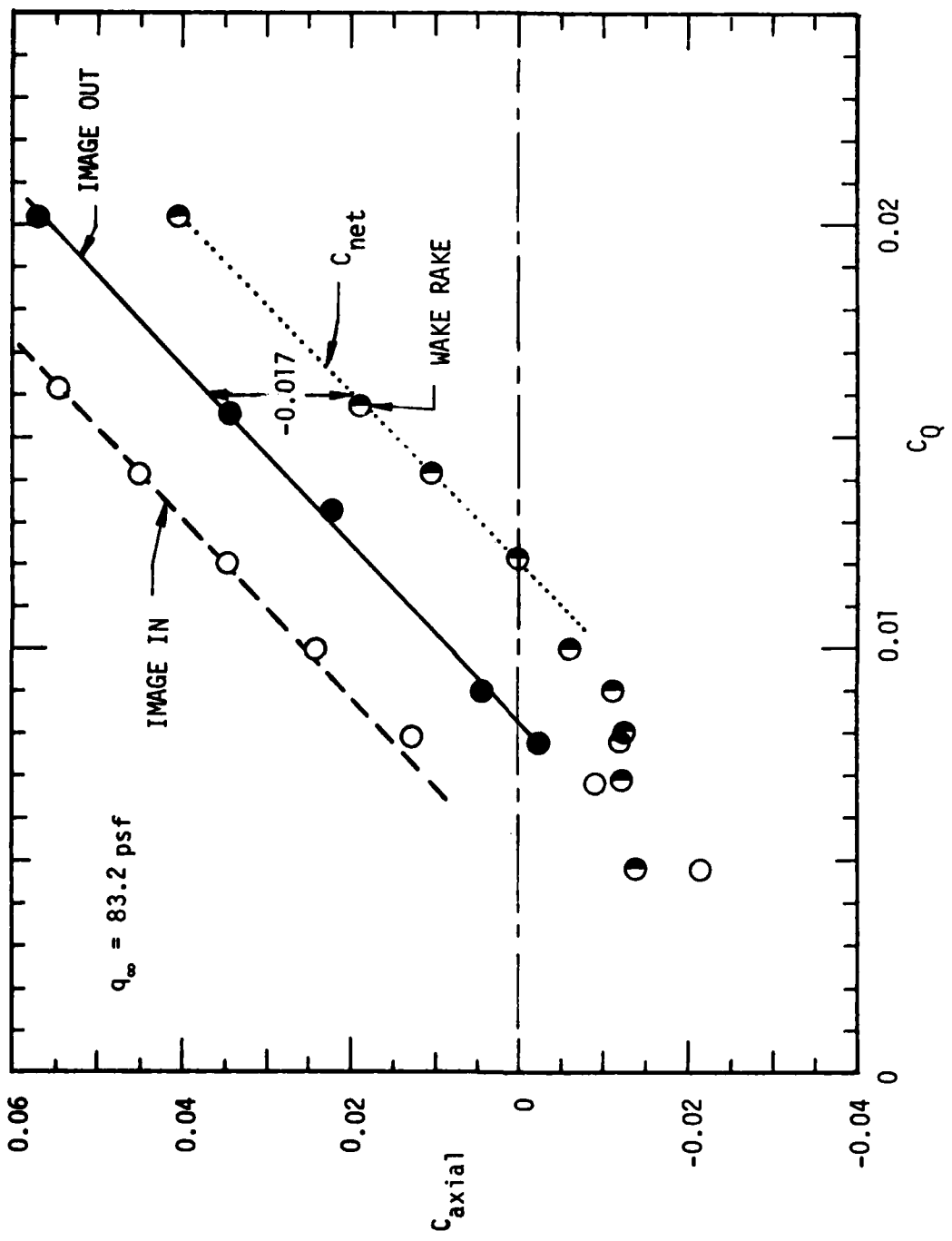


FIGURE 5-24 HDV STRUT INTERFERENCE/WAKE RAKE COMPARISON

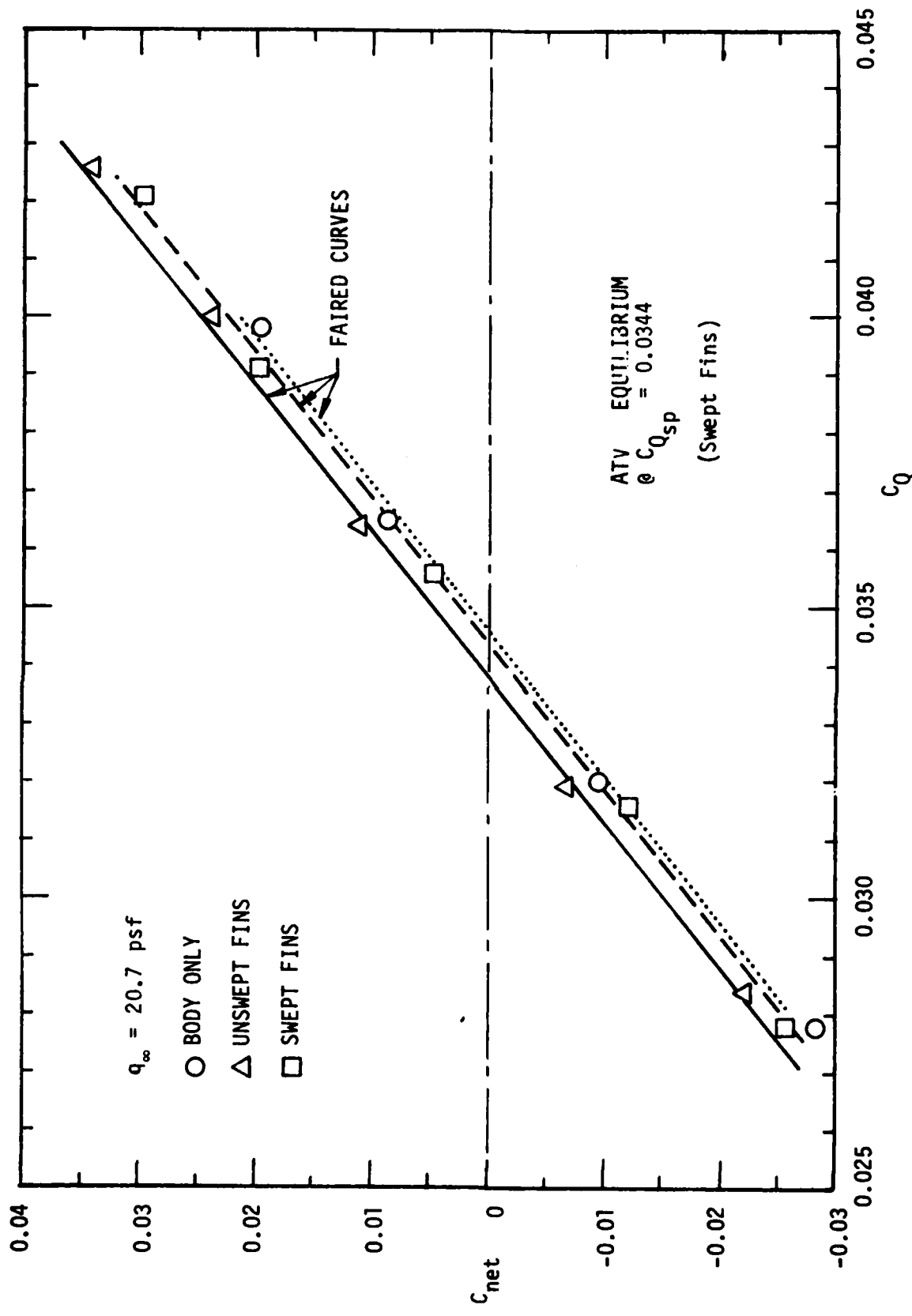


FIGURE 5-25. ATV NET FORCE CHARACTERISTICS

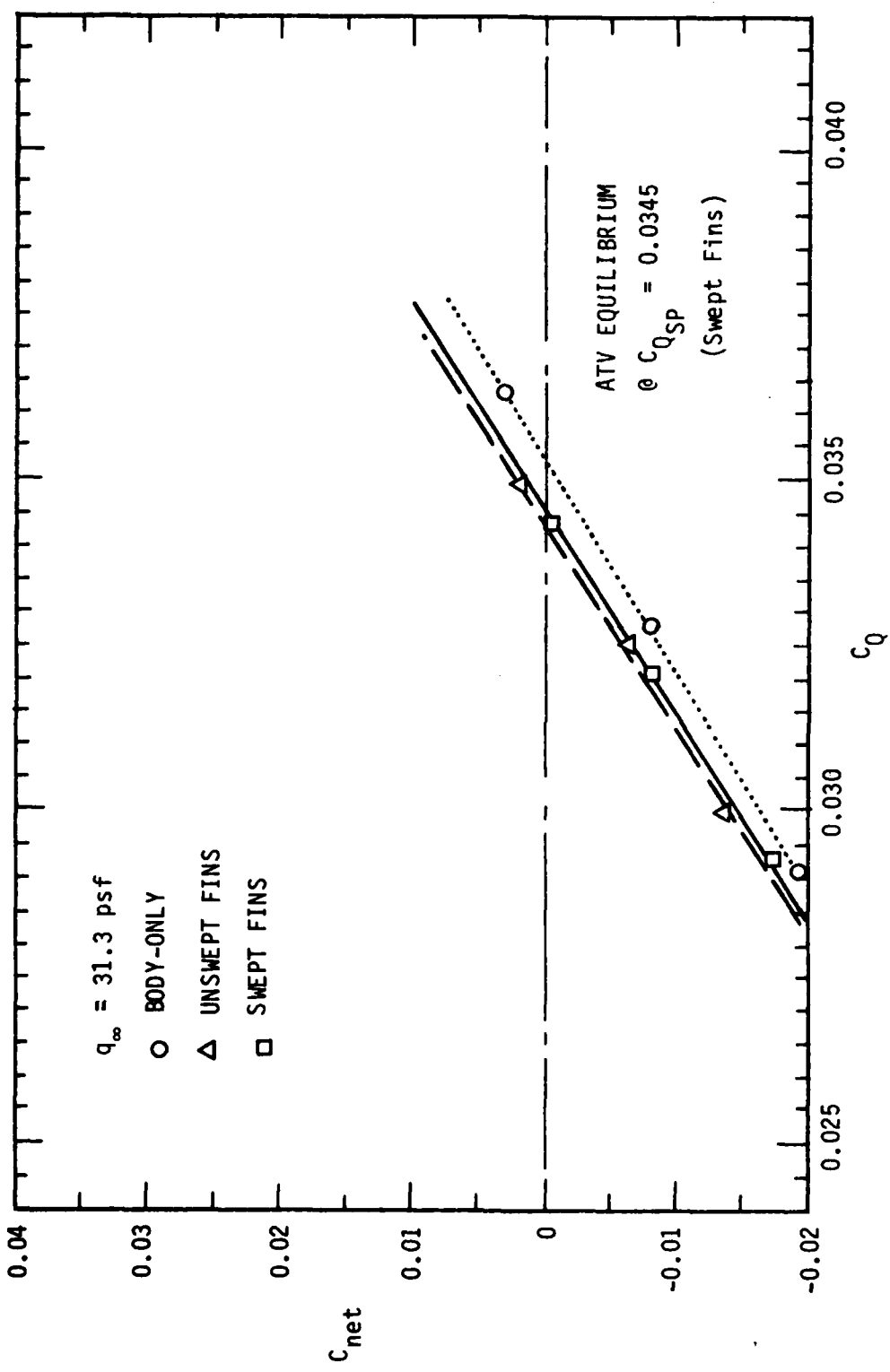


FIGURE 5-26. ATV NET FORCE CHARACTERISTICS

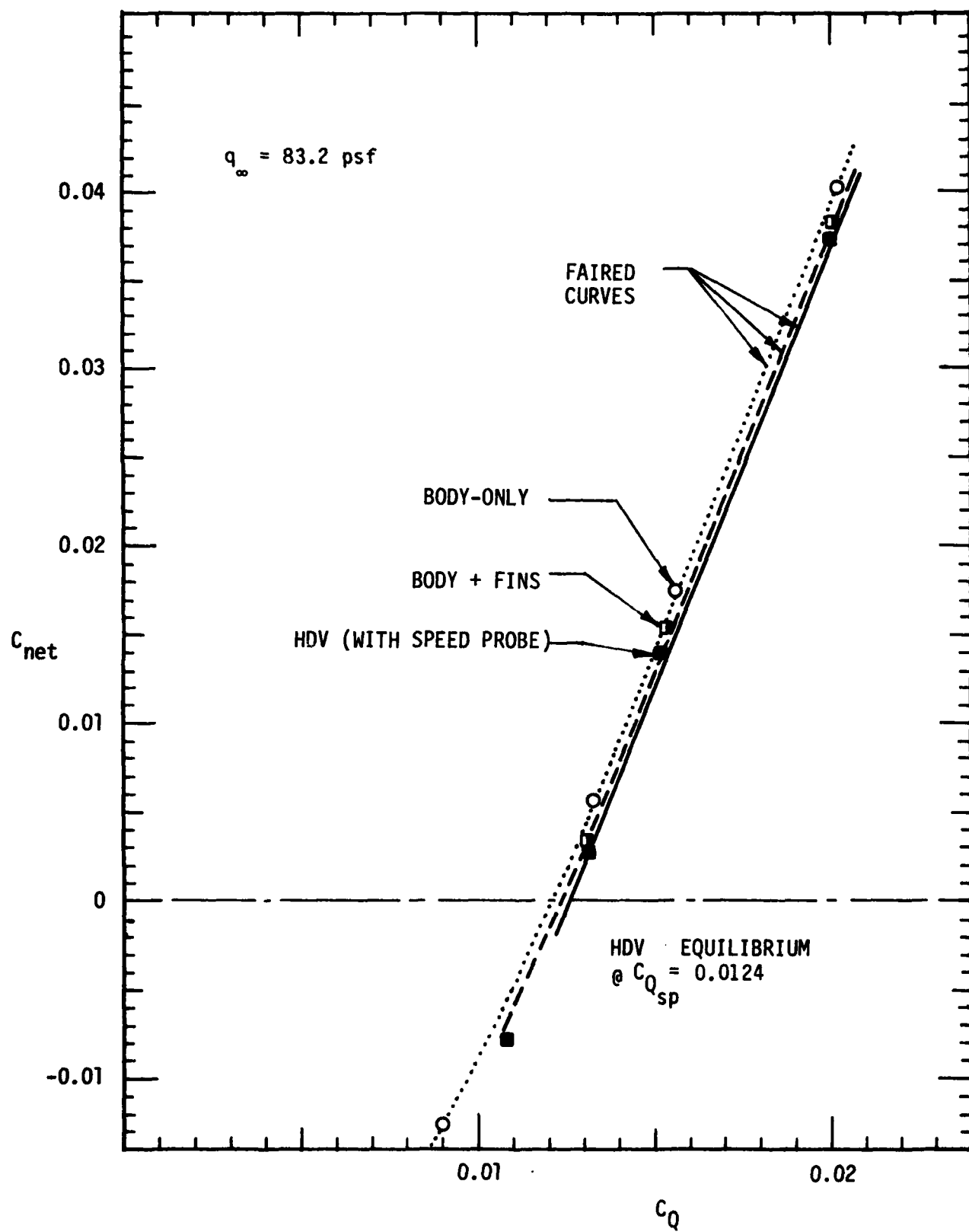


FIGURE 5-27 HDV NET FORCE CHARACTERISTICS

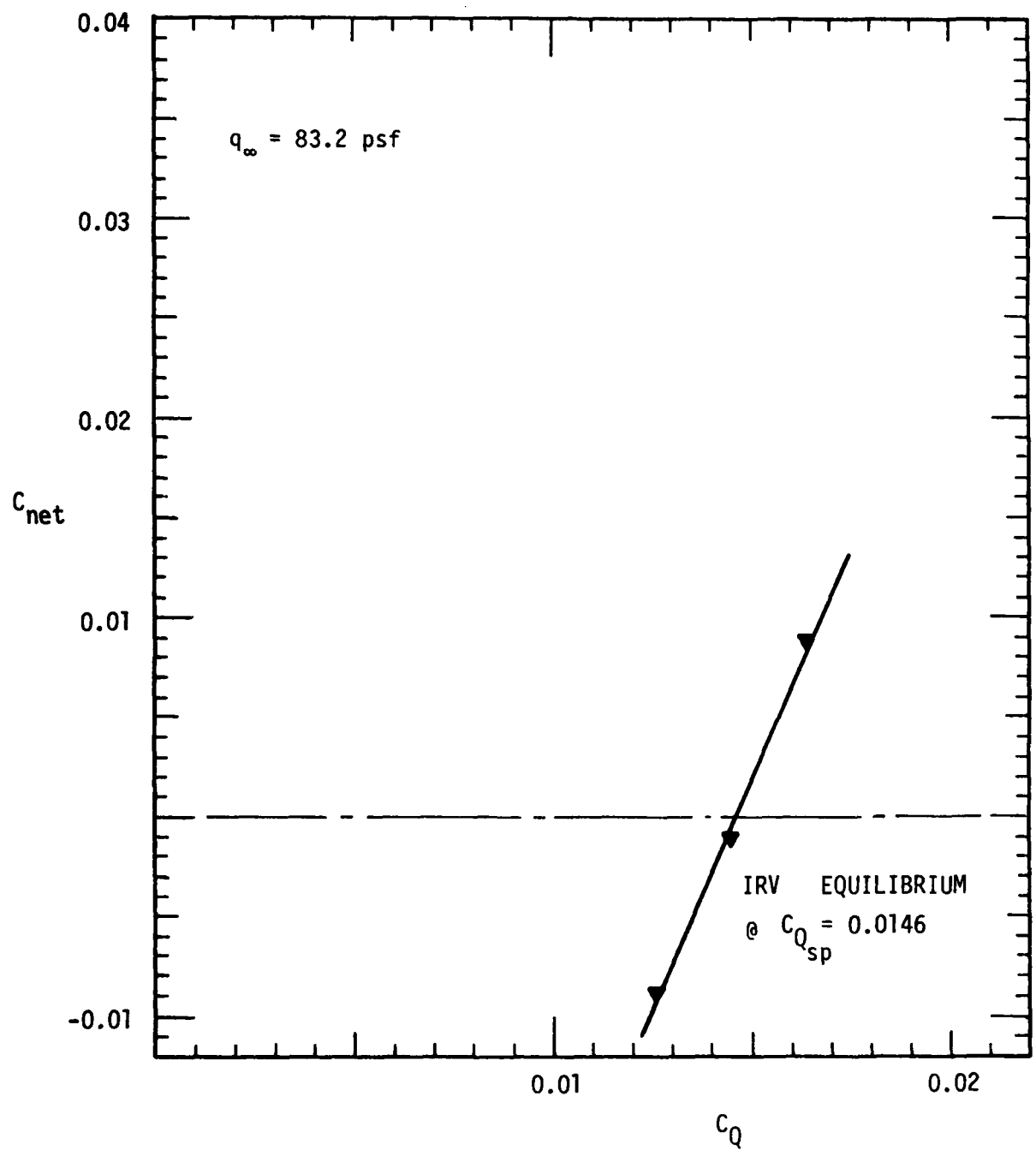


FIGURE 5-28 IRV NET FORCE CHARACTERISTICS

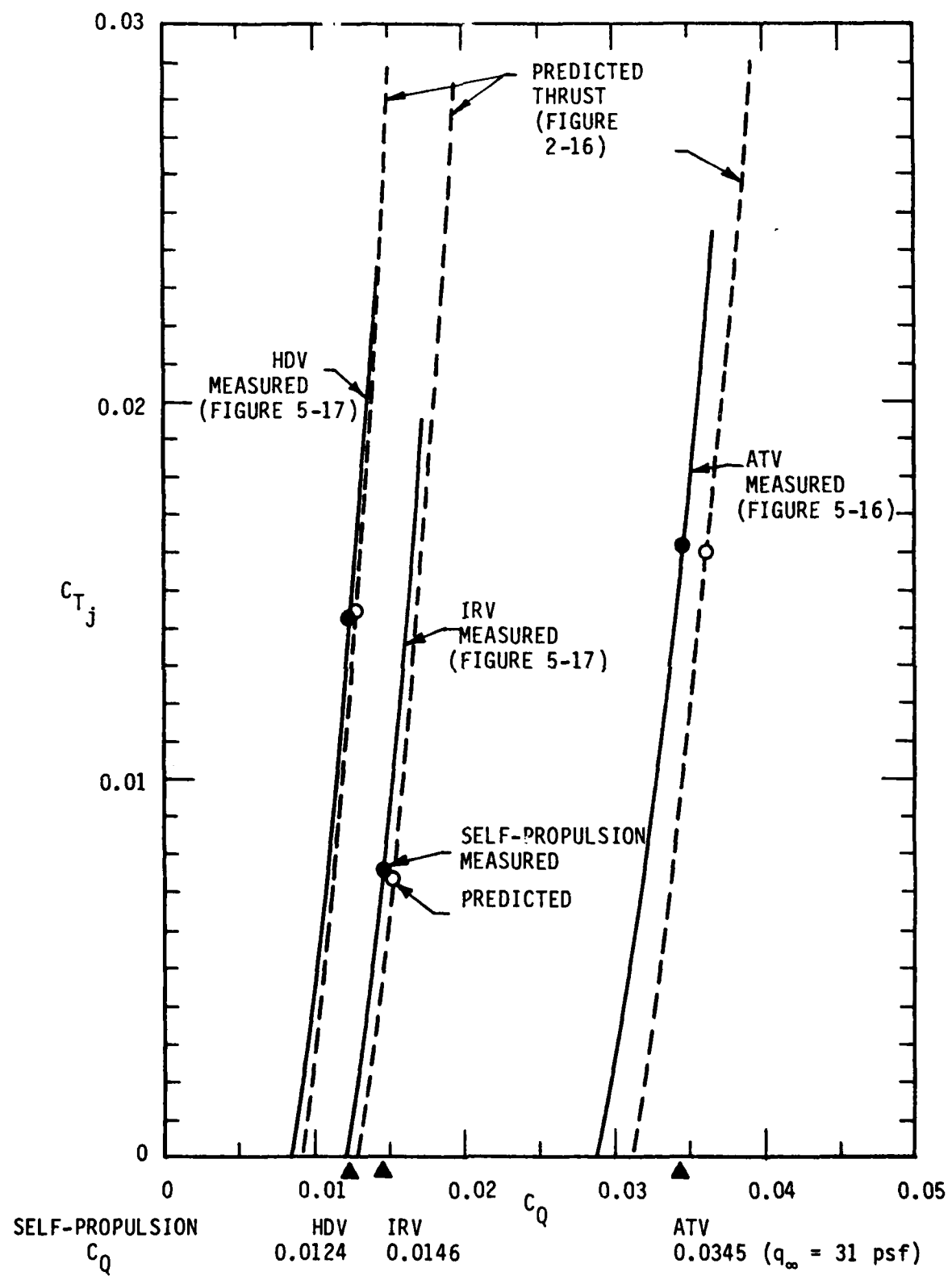


FIGURE 5-29 COMPARISON OF PREDICTED AND MEASURED SELF-PROPULSION THRUST

TABLE 5-1. COMPARISON OF MEASURED PERFORMANCE VERSUS PREDICTION METHODOLOGY AT VEHICLE DESIGN POINTS

VEHICLE CONFIGURATION	q_{∞} (psf)	C_Q	C_{TJ}	C_{P1}	C_{PJ}	C_{PT}
ATV - Swept Fins	30	Mixing	0.0360	0.0160	0.0133	0.0308
		Non-Mixing	.0383	.0247	.0134	.0422
HDV-Tailboom Fins	80	Measurement	0.0345	0.0162		
		Mixing	0.0127	0.0145	0.0027	0.0188
IRV-Unswept Fins	80	Non-Mixing	.0135	.0184	.0027	.0245
		Measurement Range Test	0.0124	0.0142 0.0140- 0.0147		
		Mixing	0.0151	0.0074	0.0027	0.0085
		Non-Mixing	.0166	.0138	.0027	.0163
		Measurement	0.0146	0.0081		
						0.0112 .0190

5.7 VEHICLE STABILITY/CONTROL FIN EFFECTIVENESS

5.7.1 ATV Normal Force Characteristics

The normal, or lifting, force characteristics of the ATV configuration were obtained from force balance measurements of the model at self-propulsion conditions with and without fins over an angle-of-attack range of $\pm 5^\circ$ and a tunnel dynamic pressure range of 20-50 psf. Data taken at $q_\infty = 31.1$ psf are presented in Figure 5-30. The bare body has a normal force slope of $C_{N_a} = 0.0096/\text{degree}$, which is about twice the value given by Hoerner¹⁸ for airship bodies at this low l/d ratio. This higher value of C_{N_a} can be attributed to the BLC which keeps the flow fully aligned and attached on the ATV afterbody as opposed to the cross flow and separation zone that occurs at the aft end of the airship hull, killing some of its lift.

Predictions were made for the lift forces expected with the two sets of fins. The force predictions assumed a local potential flow field over the fins as described in Section 2.2.2.5 and illustrated in Figure 2-13. Conventional three-dimensional lifting surface characteristics¹⁸ were used to predict the fin lift force increment as a function of angle-of-attack and the potential flow velocity distribution. The predicted force increments were added to the bare body lift curve and the results are represented by the dashed lines in Figure 5-30. The experimental data points for both fin sets are seen to lie higher than the predicted curves, showing an enhancement in effectiveness over predictions of about 30 percent for the swept fins and about 100 percent for the unswept fins. This trend was consistent throughout the test and appears to be typical for control fins mounted on a high-pressure-recovery propulsive afterbody.

5.7.2 ATV Static Stability Characteristics

Streamlined axisymmetric bodies are inherently statically unstable. At small angles-of-attack the neutral point (point about which the pitching moment is zero) is typically $1/3$ to $1/2$ ahead of the actual body. At low to moderate values of length to diameter ratio the static stability of the body can be strongly influenced by the aft-end geometry and particularly by the addition

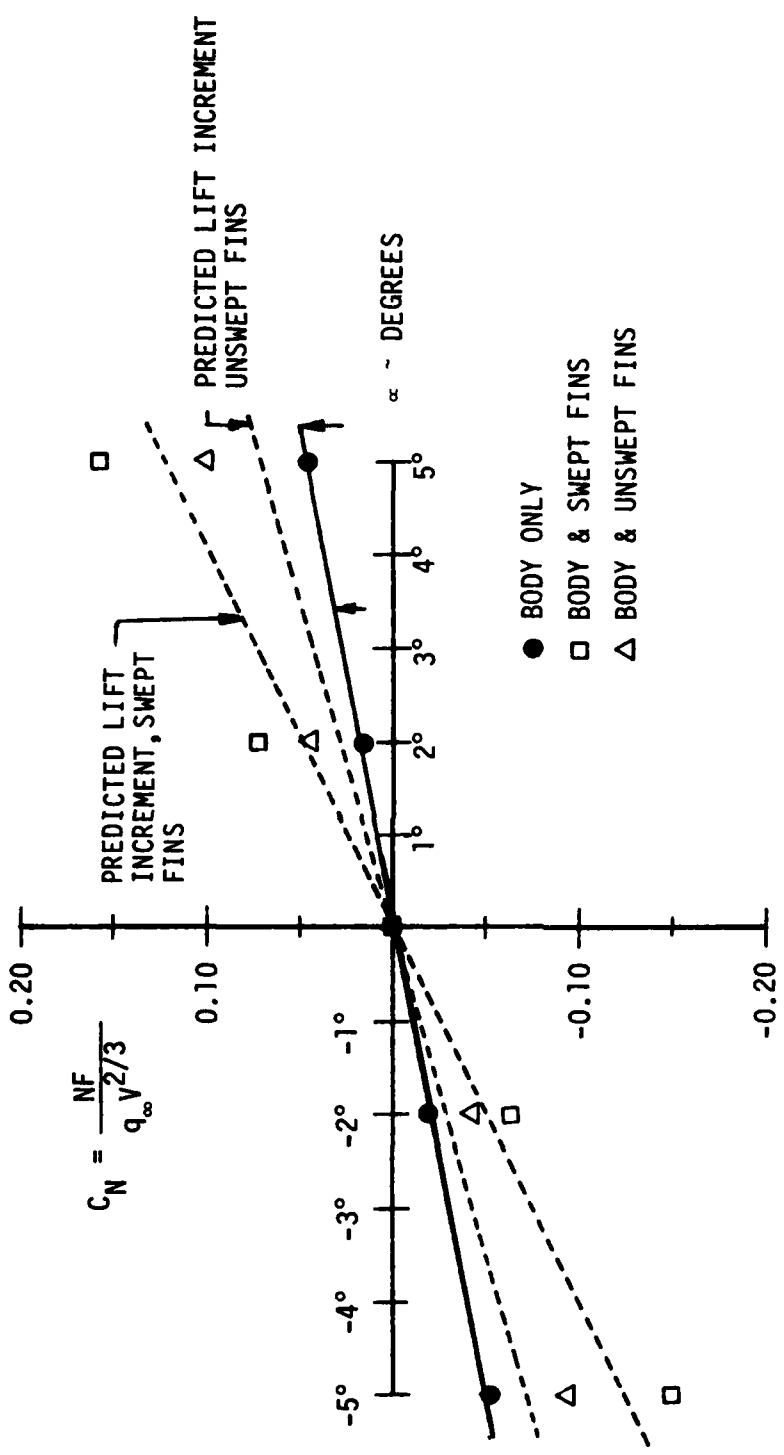


FIGURE 5-30 ATV FIN CONTROL FORCE CHARACTERISTICS

of fins. Pitching moment data for the ATV are presented in Figure 5-31. These data were taken for the same conditions and at the same time as the normal force data shown in Figure 5-30. A positive slope of the C_M vs C_N curve indicates a statically unstable configuration (i.e. as the body angle-of-attack increases causing an increase in C_N , the pitching moment increases and induces a further increase in angle-of-attack). The ATV body without fins is seen to be quite unstable. The addition of the small unswept fins reduces the slope of the $C_M - C_N$ curve by about 75 percent but still leaves the configuration unstable. Doubling the size of the fins and adding sweepback to move the fin center of pressure farther aft further reduced the $C_M - C_N$ slope to a negative level, creating in this case a stable configuration with a 6 percent static margin.

5.7.3 ATV Control Fin Effectiveness

In Figure 5-32 are presented fin control moment characteristics. The change in C_M with δ_F as shown goes in opposite directions for the two configurations because the swept fins were deflected with the trailing edge up and the unswept fins were deflected with the trailing edge down. These results demonstrate the effectiveness of the two fin configurations in generating maneuvering control forces and trimming moments. For example, if a free-running underwater vehicle of this configuration had a specific gravity greater than 1.0 such that a $C_N = +0.25$ was necessary to maintain a constant running depth, then the swept fin would have to be positioned at approximately 3 degrees to trim the pitching moment to zero while maintaining the required C_N . To achieve the same trimmed condition using the unswept fins would require about 11 degrees of deflection. It should be remembered that these results just address the control effectiveness of the fins. The static stability of the configuration does not basically change although the static margin (dC_m/dC_N) appears to decrease slightly with fin deflection.

5.7.4 HDV/IRV Static Stability Characteristics

Static stability characteristics of the HDV and IRV are presented in Figure 5-33. The HDV, with its long tail length, is just slightly stable, about 1 percent static margin. The IRV, with its close coupled fins, is seen to be unstable. Actually, even though the body size and shape are the same as the ATV and the fins are identical, the IRV is about 33 percent more unstable

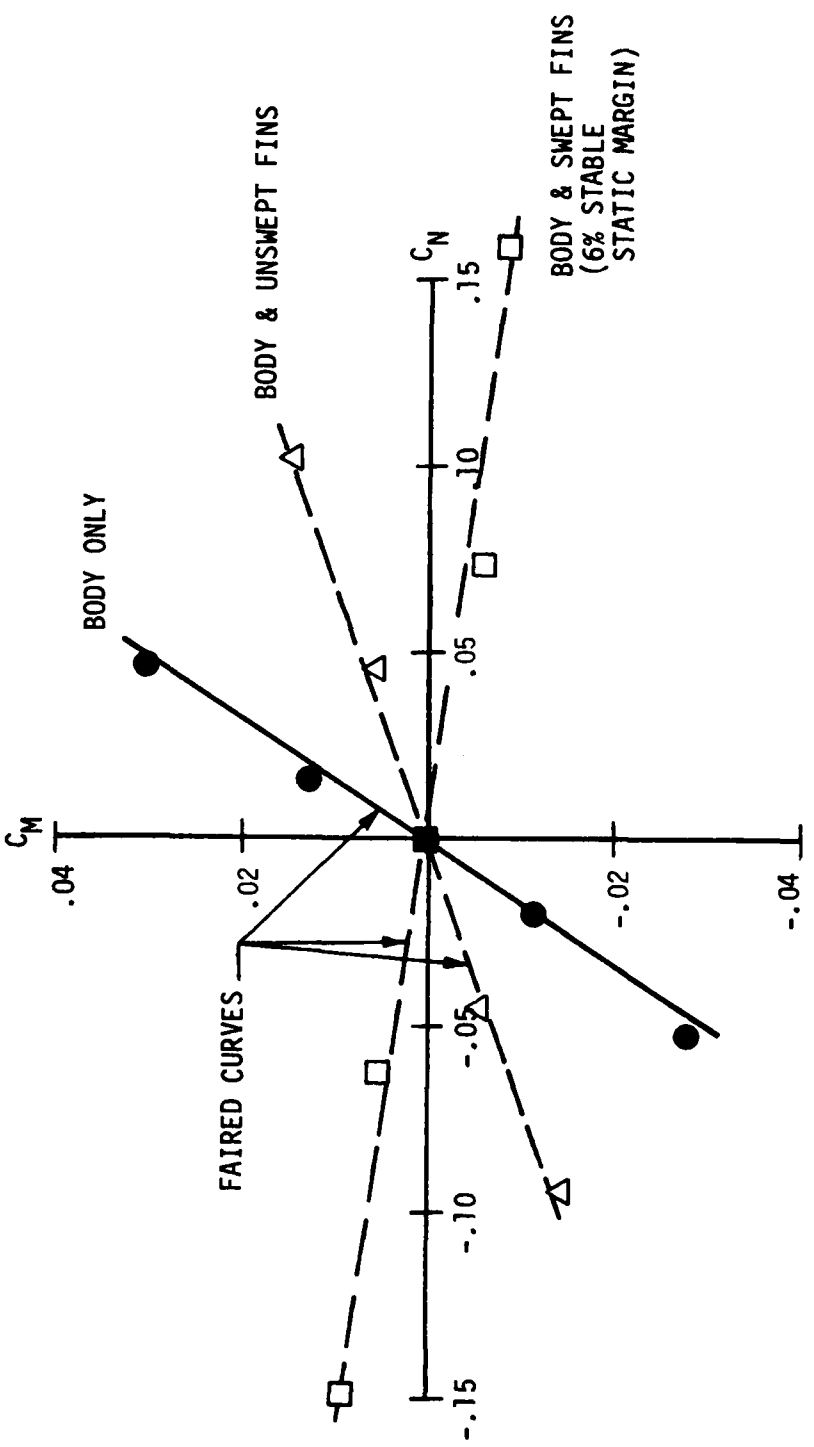


FIGURE 5-31 ATV STATIC STABILITY CHARACTERISTICS

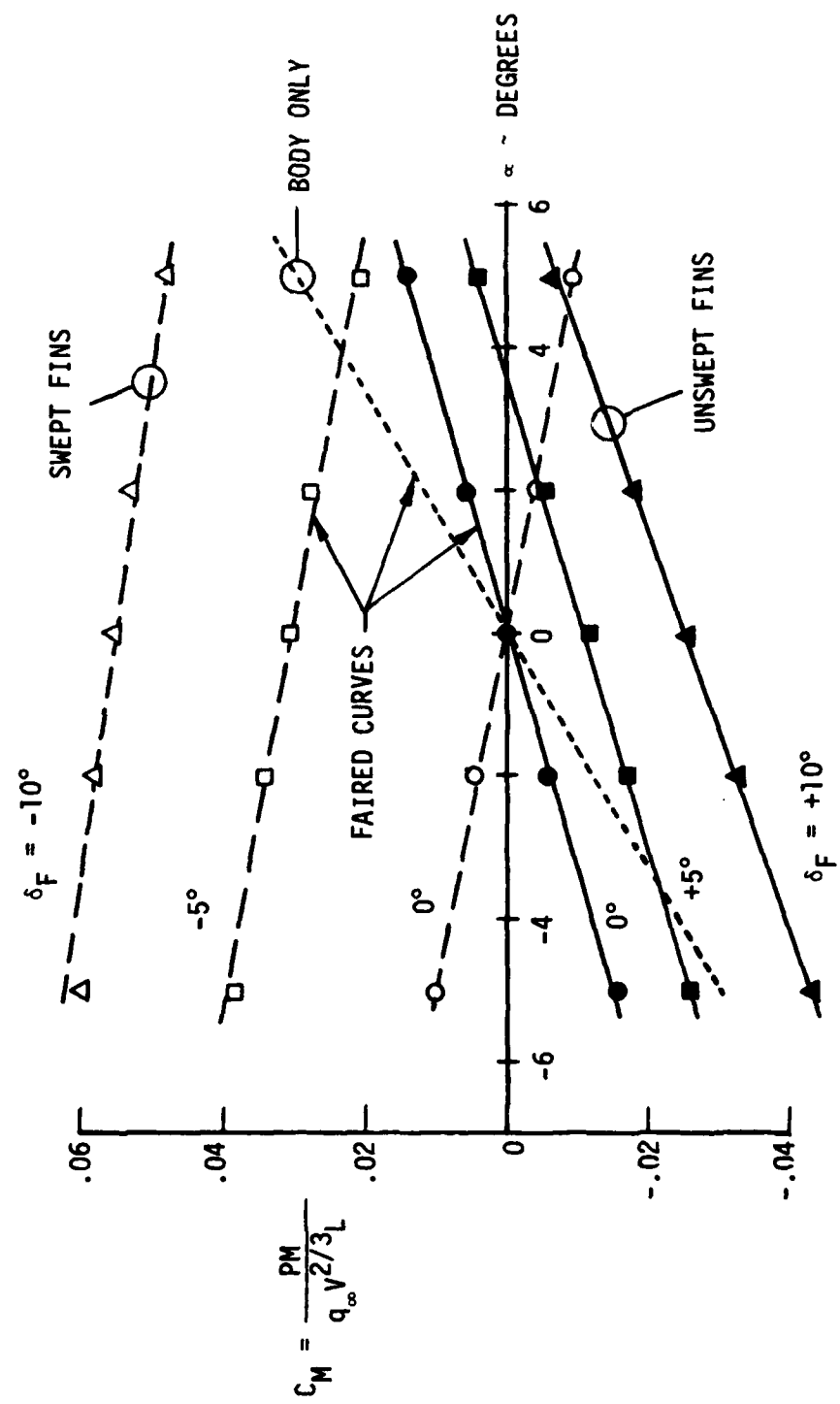


FIGURE 5-32 ATV FIN EFFECTIVENESS

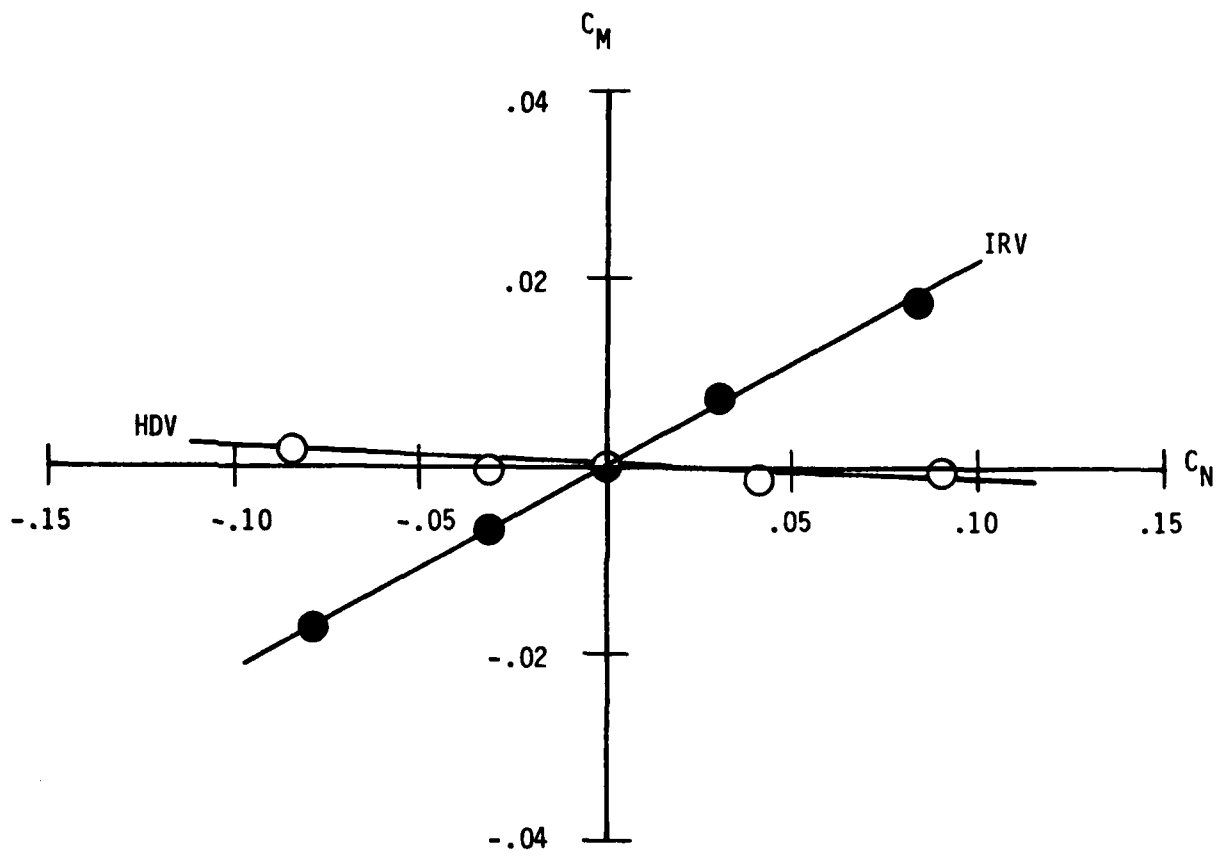


FIGURE 5-33 HDV AND IRV STATIC STABILITY CHARACTERISTICS

than the ATV with the unswept fins. The flow on the afterbody is the same (turbulent) for both configurations and its contribution to the stability characteristics should be the same in both cases. However, the forebody flow is laminar on the IRV and turbulent on the ATV and this leads to the greater instability of the IRV. Hoerner¹⁸ shows that for axisymmetric bodies C_N increases and C_M decreases at small angles of attack as the body drag increases, particularly if the drag increase is associated with the forward portion of the body. The lower degree of static instability with the ATV is due to the forebody boundary layer being tripped.

5.8 ATV DRAG CONSTITUENTS

The constituent drag of the ATV is evaluated in the following paragraphs based on measured quantities for comparison to the analytical methodology described in Section 2.2.2.

5.8.1 Shroud Drag

The drag on the ATV centerbody shroud is directly related to the spillage of the forebody boundary layer past the inlet. It has already been explained that the flow momentum deficit swallowed by the inlet is treated as a loss in the propulsor system. Any remaining momentum deficit from the forebody boundary layer that spills over onto the shroud manifests itself as a drag constituent at the BLC jet lip designated as C_D _{lip}. Figure 5-34 presents a comparison of velocity profiles at the ATV jet lip calculated from total pressure rake surveys. A constant static pressure was assumed through the boundary layer based on a wall tap measurement at each BLC flow rate. It can be expected that some degree of error will be introduced by this assumption because of body curvature and the jet interaction described in Section 5.4.1. A predicted profile is shown by the dotted line for the case of no spillage and boundary layer growth calculations made by the Granville method.¹⁴ The experimental data show how the velocity profiles approach the zero spillage prediction with increasing C_Q . The self-propulsion condition for the ATV at this test condition occurred at $C_Q = 0.0344$ which is seen to have a slight but definite increase in boundary layer thickness resulting from spillage effects. Figure 5-35 shows how the total drag on the shroud varies with C_Q . The lower dashed curves represent the forebody momentum deficit "spilling

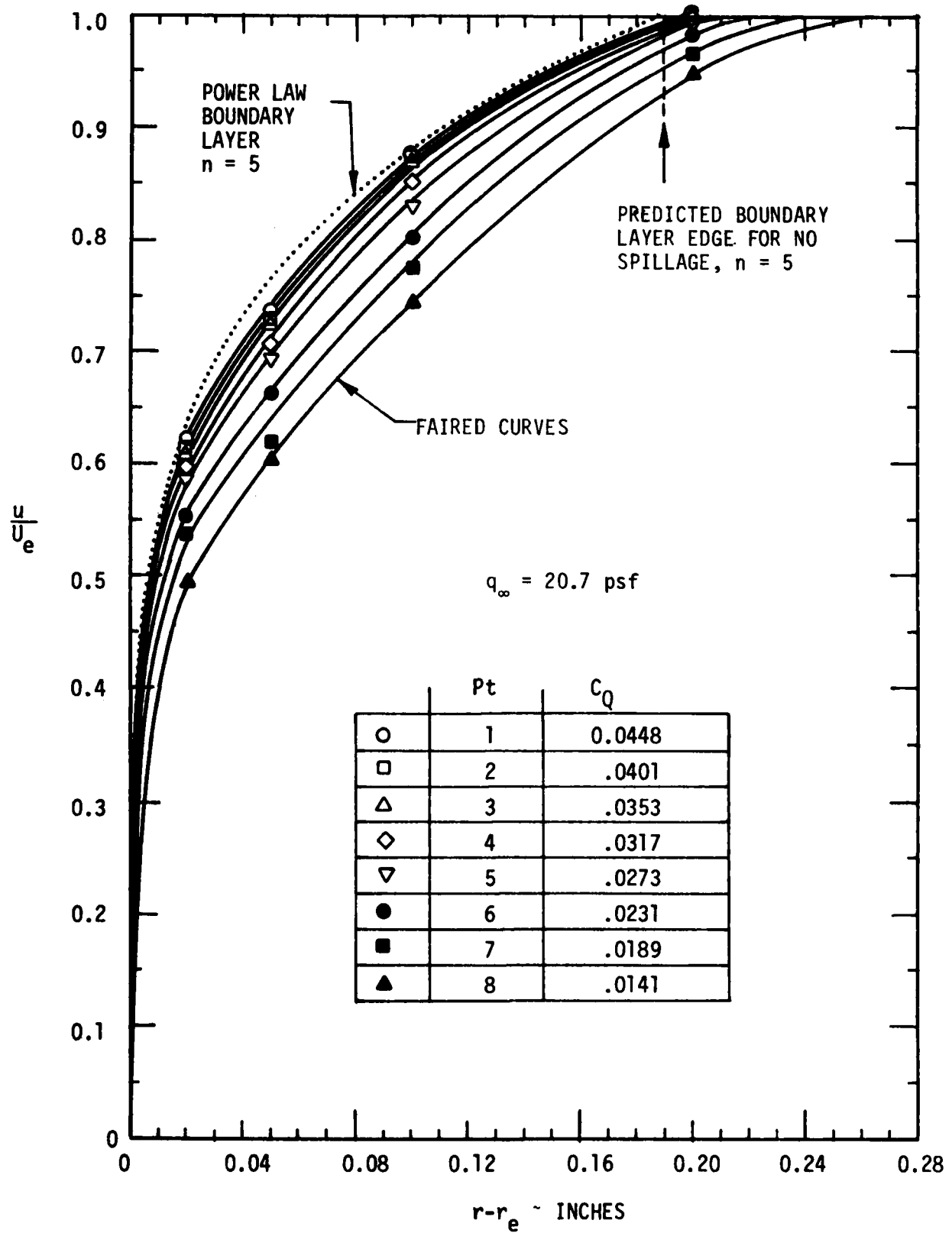


FIGURE 5-34 ATM BLC-JET LIP SURVEY DATA

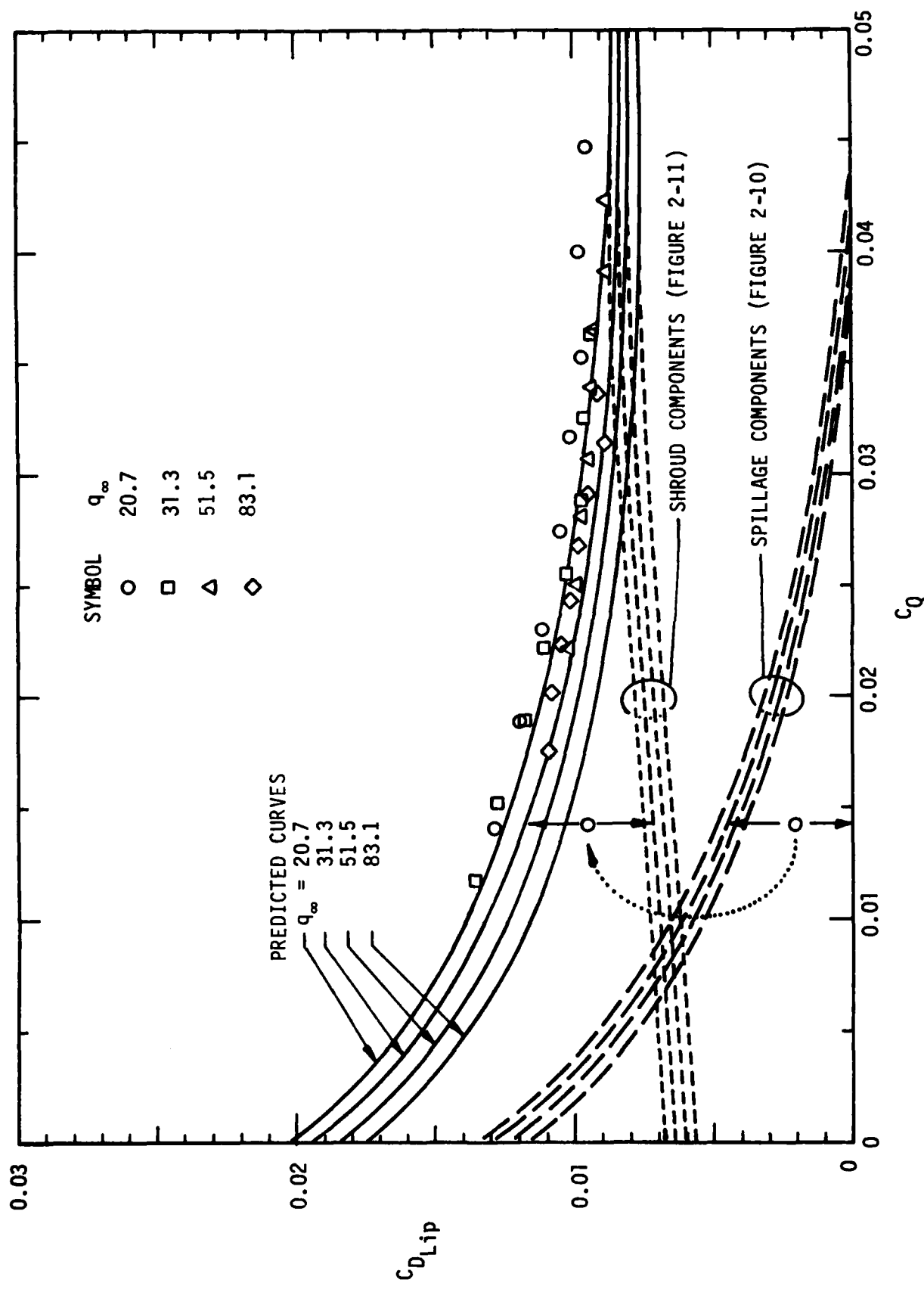


FIGURE 5-35 ATC LIP DRAG COEFFICIENTS

"over" onto the shroud as a function of BLC flow rate. The dotted curves illustrate the shroud drag coefficients influenced by an initial momentum deficit generated by the spillage, as a function of C_Q . The solid curves represent the total drag at the trailing edge. The trends and distribution of the data show good agreement with the predictions but generally fall a little high, which is believed to be caused by the uncertainty in the static pressures through the boundary layer at the lip, where the wall measurement was used as a constant through the surveys.

5.8.2 ATV Aft-Body Drag

The aft-body drag of the ATV is displayed in Figures 5-36 through 5-38 for $q_\infty = 20.7, 31.3$, and 51.5 psf respectively. The empirical afterbody drag curve from Figure 2-12, the shroud drag prediction from Figure 2-11, and the spillage drag from Figure 2-10 were summed to establish the dotted curves for body-only drag prediction (following the procedure described in Figure 2-14). The dashed curves represent the predicted aft-body drag with the small unswept fins attached wherein a fin-drag increment was included. The solid curves are the predictions with the large swept fins attached. The wind tunnel data points consist of the measured jet thrust less the balance net force corrected for support strut interference (See Figure 2-9). A comparison of the tunnel measurements with predicted aft-body drag characteristics definitively shows the validity of the analytical methodology, especially for the two configurations with fins. The body-only measurements however depart substantially from the predictions, although the difference becomes less for the higher q_∞ (51 psf). Tuft patterns near the cusp terminus, observed during the tests, indicated definite unsteadiness when the fins were removed. It may be concluded that at the low Reynolds numbers, a small amount of flow separation existed near the afterbody terminus, which disappeared when either set of fins was attached. This separation is probably aggravated by the circumferential non-uniformity of the BLC jet due to the internal stators, as illustrated in Figure 5-13. The blockage caused by the addition of fins has a favorable effect on the steep adverse pressure gradient on the body such that the flow does remain attached. Also, the data show expected trends of the drag curve and the C_Q for self-propulsion with both decreasing with increasing Reynolds number; and the body-only data lie closer to the predicted curve, indicating an improvement in the afterbody flow behavior with increasing Reynolds number.

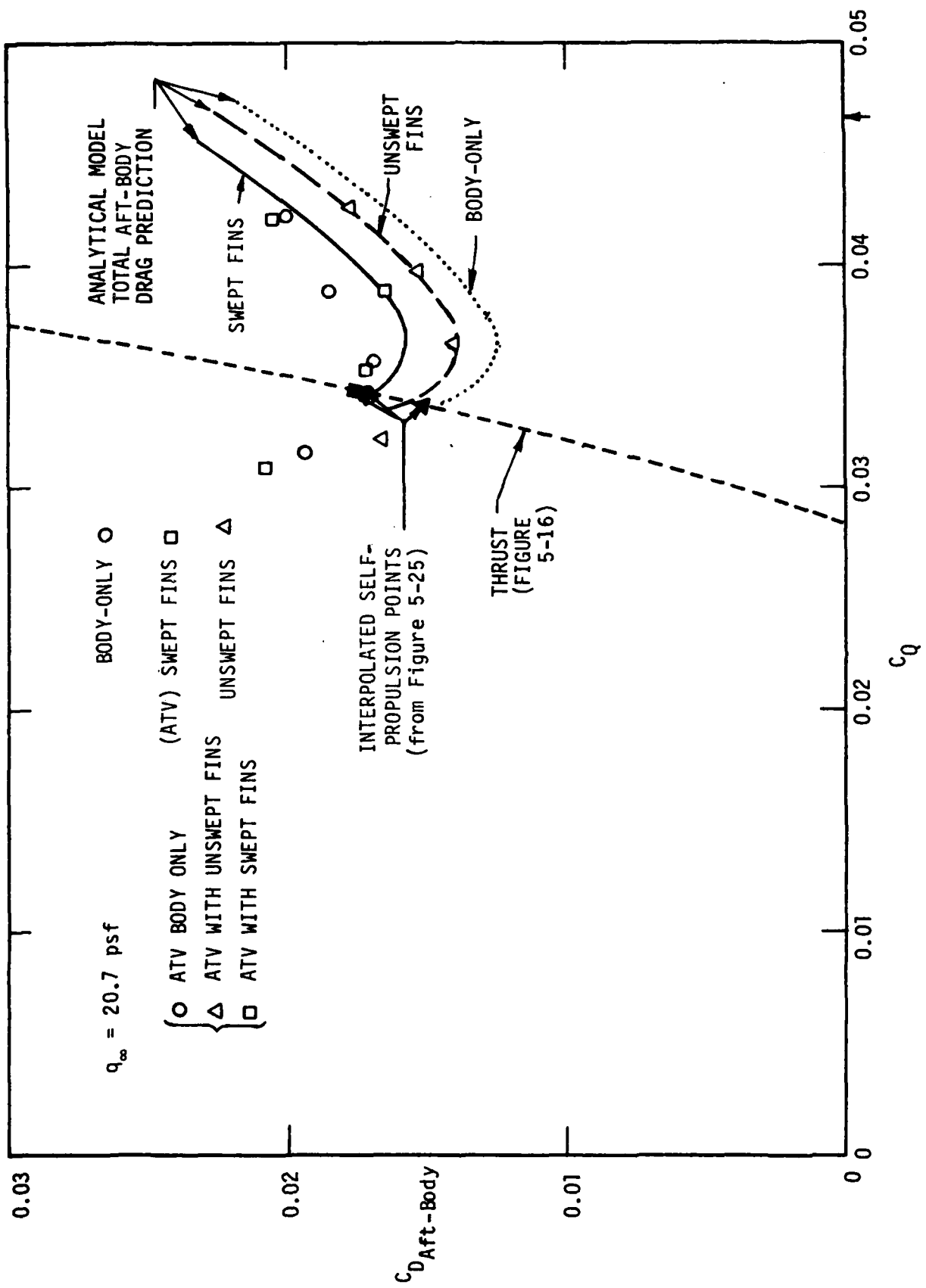


FIGURE 5-36 ATV AFT-BODY DRAG CHARACTERISTICS

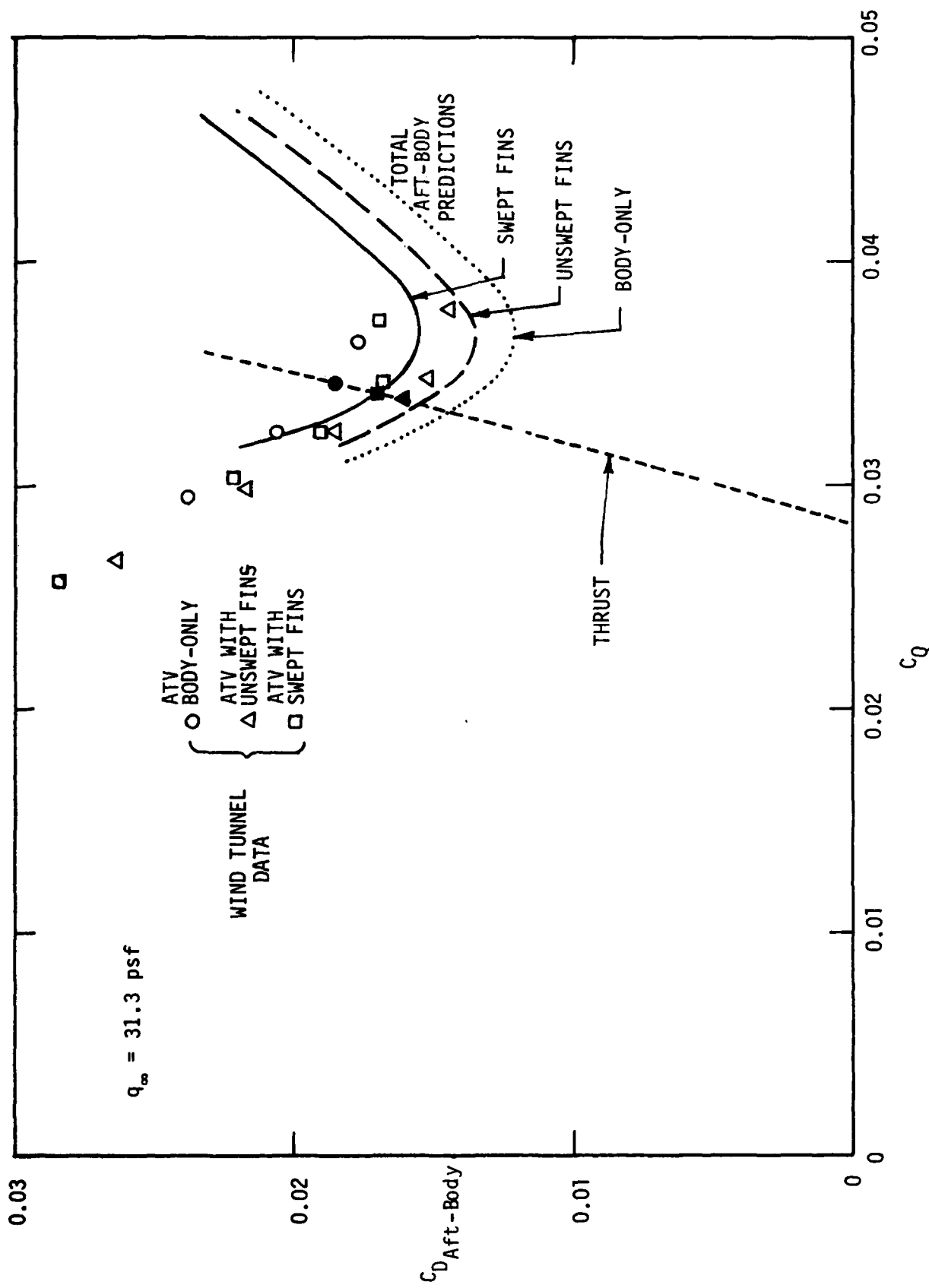


FIGURE 5-37. ATV AFT-BODY DRAG CHARACTERISTICS

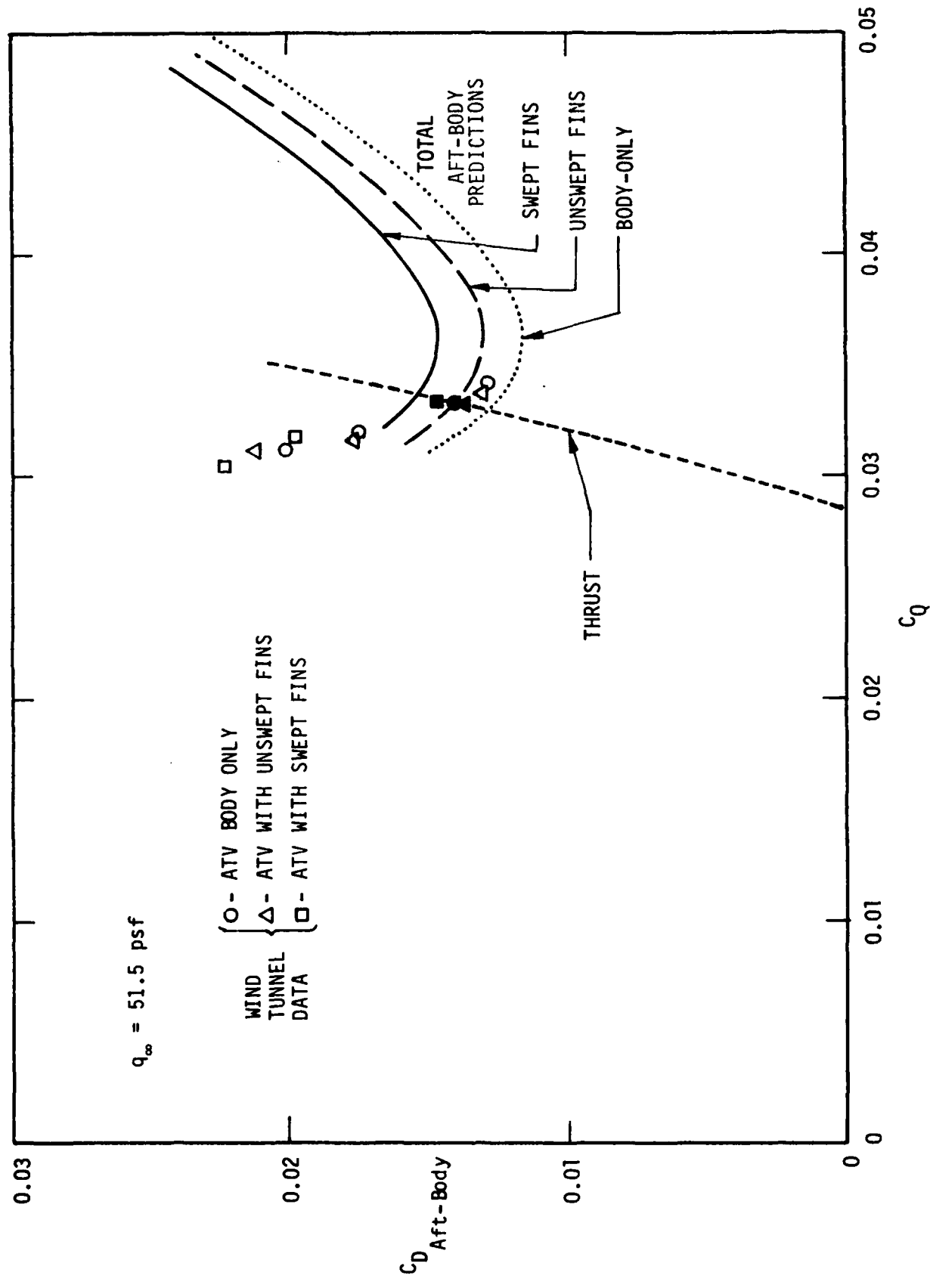


FIGURE 5-38. ATV AFT-BODY DRAG CHARACTERISTICS

The integrated thrust curve from Figure 5-16 is also shown in each figure. The self-propulsion points, interpolated for zero net force (the balance reading corrected for interference), are denoted by the solid symbols on the thrust-available curves. The agreement obviously is excellent for both finned configurations at all freestream conditions.

Also evident in Figures 5-36 through 5-38 is the fact that self-propulsion was achieved on the "back side" of the drag curve substantially off the drag minimum. This is attributed to the higher thrust content (at a given flow rate) in the blowing jet as shown in Figure 5-16 and discussed in Section 5.4.5. Needless to say, if the jet viscous characteristics had been known a priori, a jet exit area reduction could have been made to bring self-propulsion closer to the aft-body drag minimum and reduce somewhat the thrust (and power) requirements. Clearly, however, the propulsive afterbody performance characteristics have been validated and, additionally, the analytical predictive capability has been completely verified.

5.8.3 Preston Tube Skin Friction Measurements

The Preston tube instrumentation described in Section 4.3.7 was active on nearly all runs but the usefulness of the data was questionable. Typical results, reduced to local skin friction coefficients, are shown in Figure 5-39. The main problem arose from pressure tubes not lying flush on the body surface, probably due to handling damage. Also, the forward-most Preston tubes (at or near the jet exit) inadvertently did not get connected in the instrumentation matrix in any of the configurations and this left out the local measurements at the point where skin friction would be the highest and the incremental areas would be the greatest. For these reasons the Preston tube data were not used in any assessment of afterbody drag.

5.8.4 Afterbody Drag Summary

The drag characteristics of all three propulsive afterbody configurations are compared to the empirical prediction in Figure 5-40. The HDV data base¹¹ from previous wind tunnel and in-water tests, upon which the correlation is based, is also included. All data were scaled to a common Reynolds number of 14×10^6 to match the range data base. The original wind tunnel test model of the HDV had a wide jet opening which provided self-propulsion at

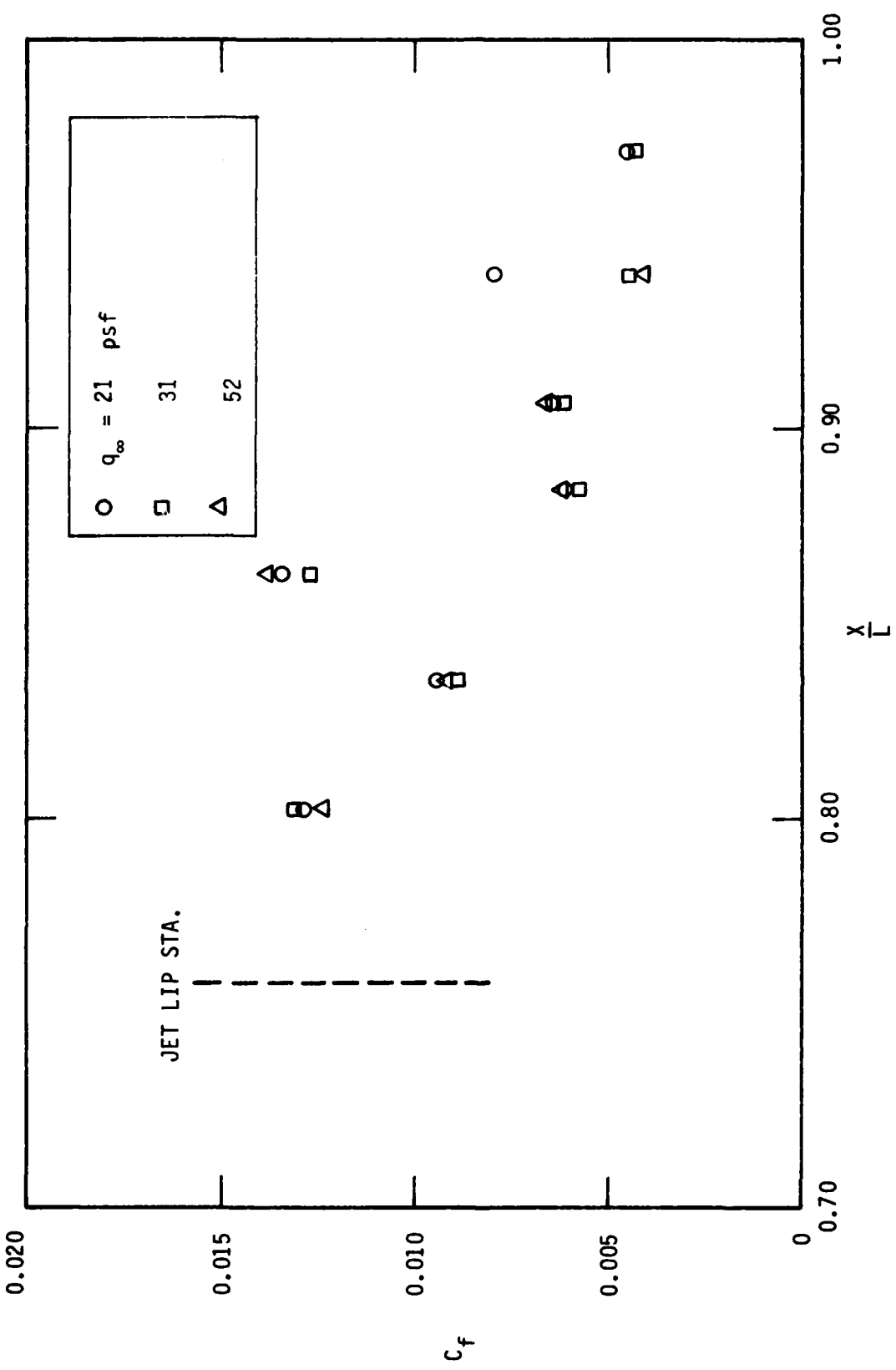


FIGURE 6-39. ATF SKIN FRICTION MEASUREMENTS (PRESTON TUBES)

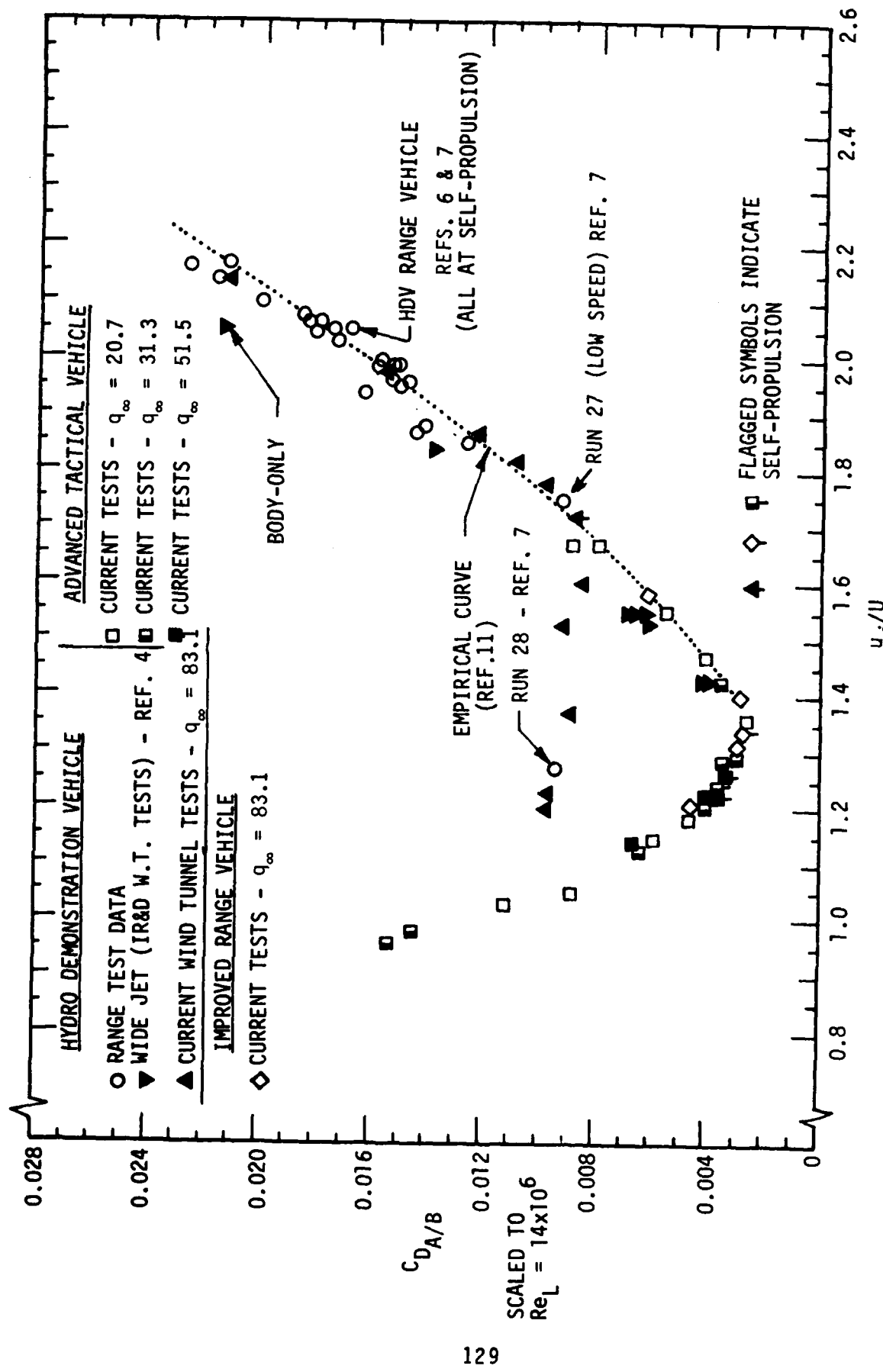


FIGURE 5-40. AFTERBODY DRAG CHARACTERISTICS - SUMMARY

low jet velocities similar to the ATV and IRV. It also was tested without fins. All other data in the figure were measured with fins attached. The HDV data from the current tests are seen to correlate very well with the in-water range results, with the self-propulsion wind tunnel point falling right beside the range data point for the same configuration (run 27, ref. 7).

The wind tunnel data clearly indicate that at blowing conditions equal to self-propulsion and above, the propulsive afterbody drag is a unique function of jet velocity ratio. Below the self-propulsion points there is one fundamental difference displayed in the figure. The high-flow-rate/low-velocity jet configurations (ATV, IRV, original HDV wind tunnel) show a drag curve that equilibrates with thrust at low drag levels and low jet velocity ratios and has a steep drag rise with reduced blowing rates. This is indicative of a separated boundary layer and wake region, producing a large base drag component at underblowing conditions. The HDV range test configuration shows a different drag characteristic below self-propulsion. The afterbody boundary layer also separates here, but the combination of a thin high-velocity jet and a favorable pressure gradient established on the tail boom at jet velocity ratios greater than 1.15 allows the flow to re-attach on the tail boom rather than going directly to a turbulent wake. Thus a separation zone exists but not a large turbulent wake, and the drag rise rate at reduced blowing rates is very gradual, similar to a form drag trend. For jet velocity ratios near 1 the pressure gradient along the tailboom is not favorable enough to sustain re-attachment and the drag behavior then becomes similar to the other configurations. An HDV range data point (run 28, ref. 7) falls within the jet velocity range where the separation bubble exists, and again the agreement between the range result and the wind tunnel test is very satisfactory.

It may thus be concluded from these results that the empirical afterbody drag curve is well substantiated for both laminar and turbulent flow forebody configurations. Furthermore, the drag "bucket" is predictable and BLC jet geometries can be reliably designed to provide self-propulsion operation at the minimum drag levels for any generic configuration, whether laminar or fully turbulent.

5.9 PROPULSOR FLUID POWER REQUIREMENTS

Evaluation of the propulsor power coefficients may be accomplished in a

straightforward manner. The total fluid power is simply the difference between the jet excess power (at the self-propulsion flow rate) obtained from Figure 5-18 or 19 and the inlet power deficit from Figure 2-15. This quantity represents the fluid power input required from an internal propulsor defined by a control volume whose entrance is the inlet and that exits at the BLC-jet exhaust. The power coefficients for all test configurations are presented versus volume-Reynolds number in Figure 5-41. Wind tunnel test goals, determined prior to initiation of the test program, are also shown. These goals were established using the methodology described in this report, with a 20 percent 'conservatism' factor added to the afterbody drag characteristics near the bucket (based on the previous body-only, wide-jet HDV model wind tunnel test, Figure 2-12).

The ATV Reynolds number dependence follows the characteristic turbulent flow trend defined by the goal curve. Overall uncertainty in power coefficients, due to experimental accuracies, is judged to be on the order of 5 percent, based in part on the close agreement with the analytical model.

The laminar-flow vehicle configurations show a substantial reduction in required propulsor fluid power. Indeed the IRV requires only about a third of the power needed for the same vehicle configuration with turbulent flow, even at these low Reynolds numbers. At higher Reynolds numbers, of course, this difference would be even greater.

A final summary comparison of the test results of Figure 5-41 with the design-point predictions provided in Section 2 has been made in Table 5-2 below:

TABLE 5-2 POWER COEFFICIENT SUMMARY

CONFIGURATION	$Re_{v1/3}$	PREDICTED	MEASURED
Advanced Tactical Vehicle	1.5×10^6	0.0308	0.0321
Hydrodemonstration Vehicle	2.4×10^6	0.0202	0.0213
Improved Range Vehicle	2.4×10^6	0.0112	0.0128

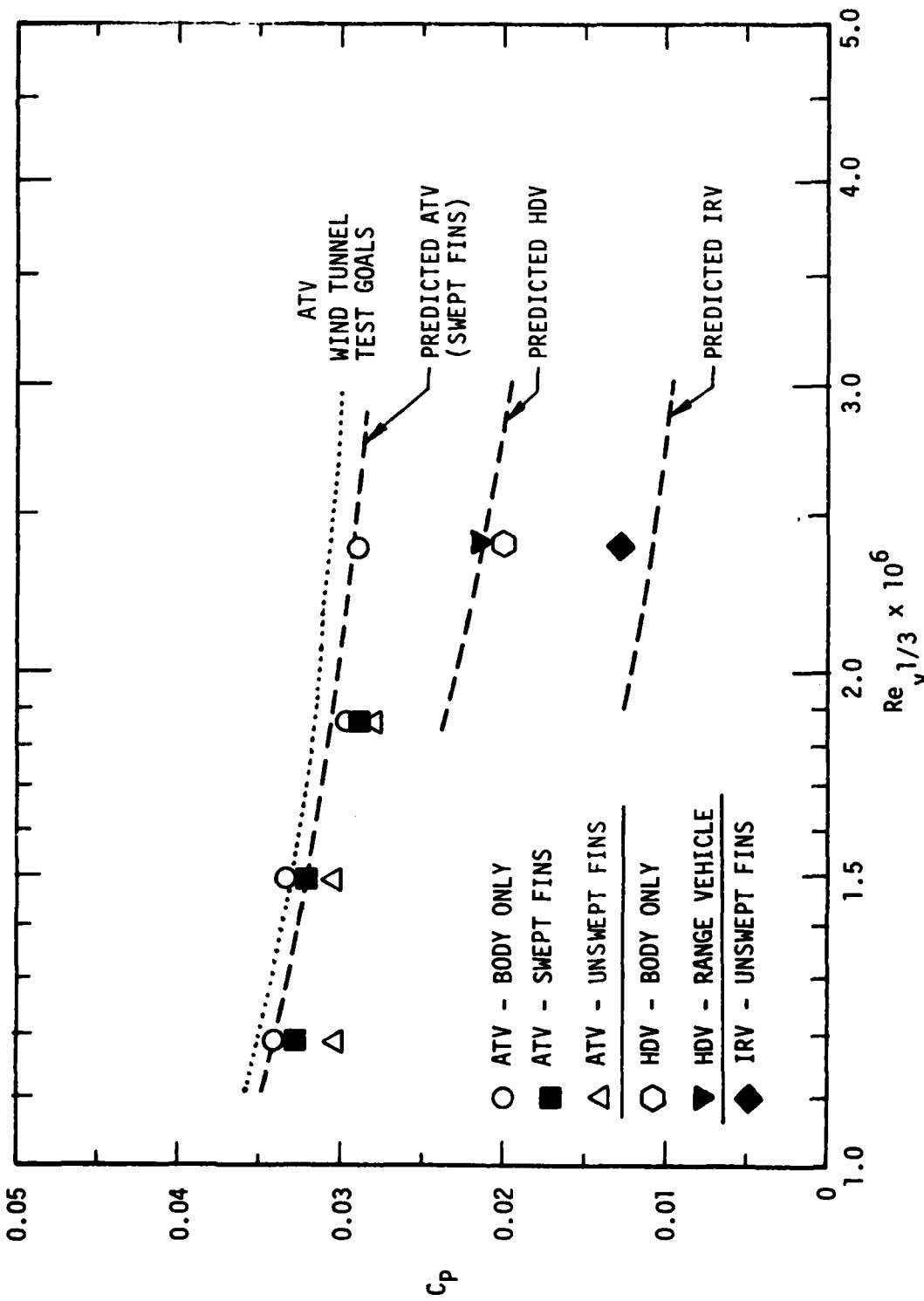


FIGURE 5-41 VEHICLE FLUID POWER COEFFICIENTS

6.0 MISSION VEHICLE PERFORMANCE

The validation of the integrated BLC-propulsor performance and predictive methodology provides the basis for an evaluation of a mission capable vehicle operating over the same Reynolds number range. Whereas the current test program was performed with existing hardware from the Hydropropulsion Demonstration program, a mission-capable configuration can be more optimally synthesized. Two configurations have been addressed, namely a 2.75 fineness-ratio body, selected for direct comparison to alternate afterbody propulsor concepts, and a high-prismatic-coefficient design with a 4.7 fineness ratio, specified to interface with selected launch platforms.

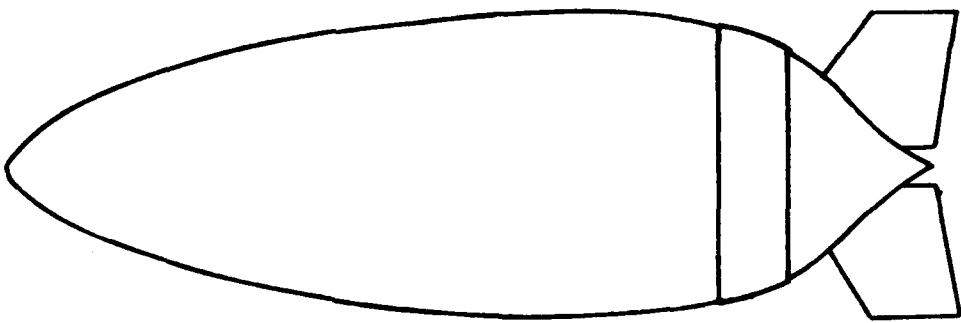
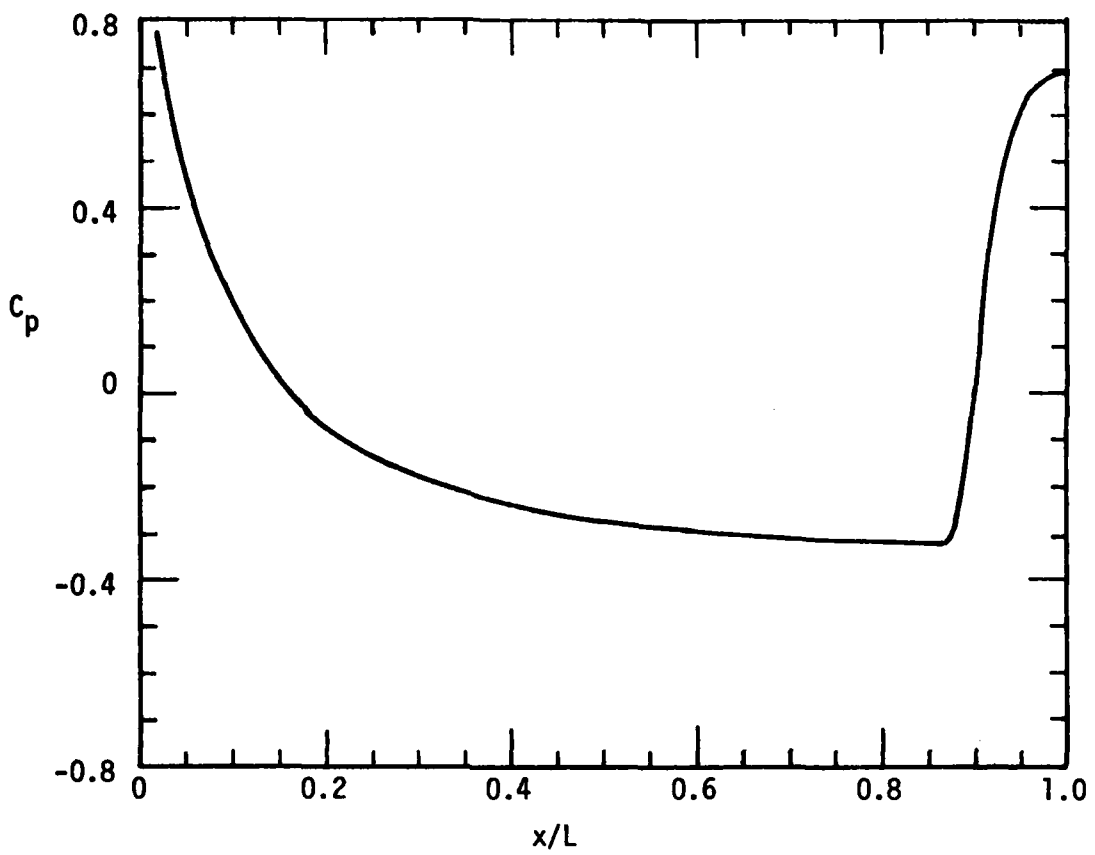
6.1 IMPROVED ADVANCED TACTICAL VEHICLE

Configuration dimensions, hydrodynamic layout and inviscid body pressure distribution is provided in Figure 6-1 for the Improved ATV. The body maximum diameter is identical to that of the original ATV model configuration. The larger volume (4.70 cf compared to 3.50 cf) results from a slight length increase (for a 2.75 fineness ratio) and the fuller forebody contour, identical to a discrete-suction body configuration.²³ The body prismatic coefficient is 0.61.

The inlet and blowing jet stations have both been located farther aft than on the original ATV and represent optimization for a turbulent-flow configuration at this fineness ratio rather than the laminar-flow-design HDV. Inlet-to-jet spacing, approximately 7 percent of the body length, has been selected to accommodate an axial-flow turbine pump rather than the centrifugal-type previously used. Fin selection was based on a 2 percent stable static margin and located on the afterbody within the maximum diameter constraint.

A comparison of the pressure distribution with that of the original ATV (Figure 2-8) reveals the less-favorable forebody pressure gradient produced by the fuller, higher prismatic-coefficient shape that provides more available volume. The afterbody shape and adverse pressure gradient is essentially identical to that of the original ATV.

Constituent drag components for the forebody (tripped at ten percent length), shroud, afterbody, and fins, as well as the selected BLC jet thrust



	NOSE	CENTER OF BUOYANCY	INTAKE	AFTER-BODY LIP	FIN LEADING EDGE	TERMINUS
STATION (INCHES)	0.00	28.81	41.90	45.82	47.89	54.42
DIAMETER (INCHES)	0.00	17.45	15.81	13.86	10.63	0.00
AREA (SQ. INCHES)	FLUSH		—	9.21		
VOLUME (CF)	4.70					

FIGURE 6-1 IMPROVED ATV CONFIGURATION

characteristics are provided in Figure 6-2 for a volume Reynolds number of 1.2×10^6 . The intersection of the thrust and total aft-body drag (spillage, shroud, afterbody and fins) occurs at a C_Q of 0.029. The jet exit area is 9.21 in.² for this self-propelled condition. The fluid power coefficients, as a function of flow-rate, are also provided in Figure 6-2. At the self-propulsion C_Q , the total fluid power coefficient ($C_{P_i} + C_{P_j}$) is 0.030 for the $Re_v^{1/3} = 1.2 \times 10^6$. The vehicle power system requirements for operation at this Reynolds number could be obtained by dividing by a pump efficiency, probably in the 0.8-0.9 range. A more exact determination of pump efficiency would require additional analytical/experimental information that is currently unavailable.

6.2 ADVANCED UNDERWATER VEHICLE

The adaptability of the BLC-propulsive jet concept to a high prismatic-coefficient torpedo-shaped configuration has been evaluated for an advanced underwater vehicle design. A fineness ratio of 4.7 was selected to interface with certain launch platforms. Body fullness, in both the forebody and afterbody regions, was maximized within constraints imposed by flow separation at a $Re_v^{1/3} = 1.2 \times 10^6$. The AUV configuration is essentially a fully-turbulent configuration with transition occurring ahead of the 8 percent axial location. Configuration details and body pressure distribution are provided in Figure 6-3.

The same integrated-propulsor and static-margin criteria, used for the improved ATV configuration, have been adopted for the AUV. The AUV body prismatic coefficient is 0.85.

AUV drag and thrust characteristics are presented in Figure 6-4 along with fluid power coefficients. Data format is identical to that of the improved ATV in Figure 6-2. Self-propulsion, near the aft-body drag minimum, occurs at a $C_Q = 0.025$ for a jet exit area of 12.56 sq. inches. As indicated in Figure 6-4, the portion of forebody drag that 'spills over' (not ingested into the inlet) is much larger than that of the ATV test configuration described in this report. Energization of this momentum deficit, along with the shroud contribution, is achieved by the blowing jet on the afterbody to prevent flow separation. This feature permits a flow-rate optimization to achieve self-propulsion at minimum power. That is, afterbody flow separation prevention

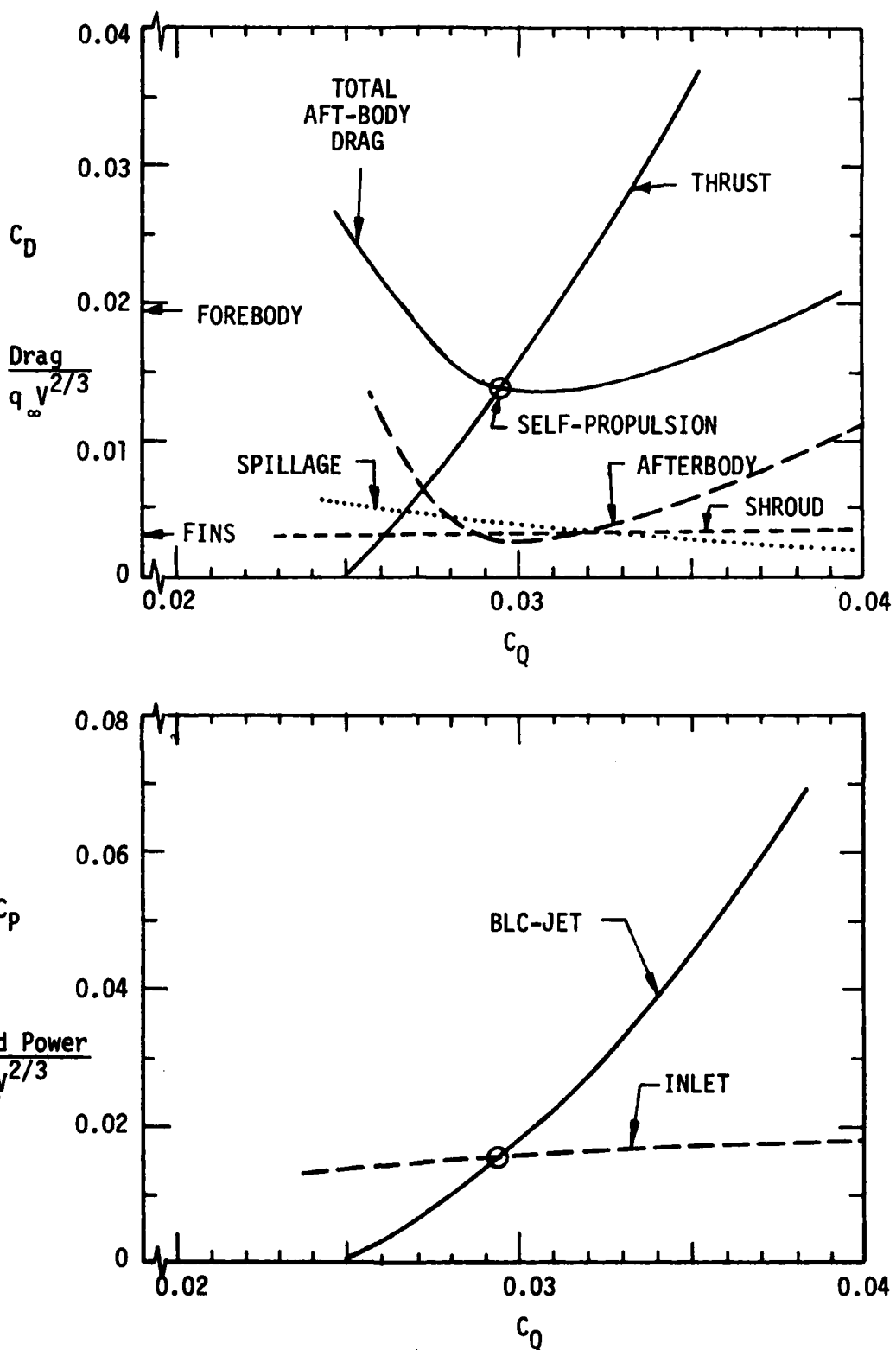
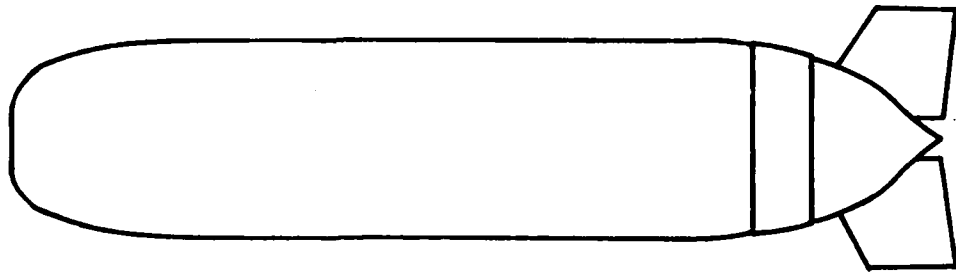
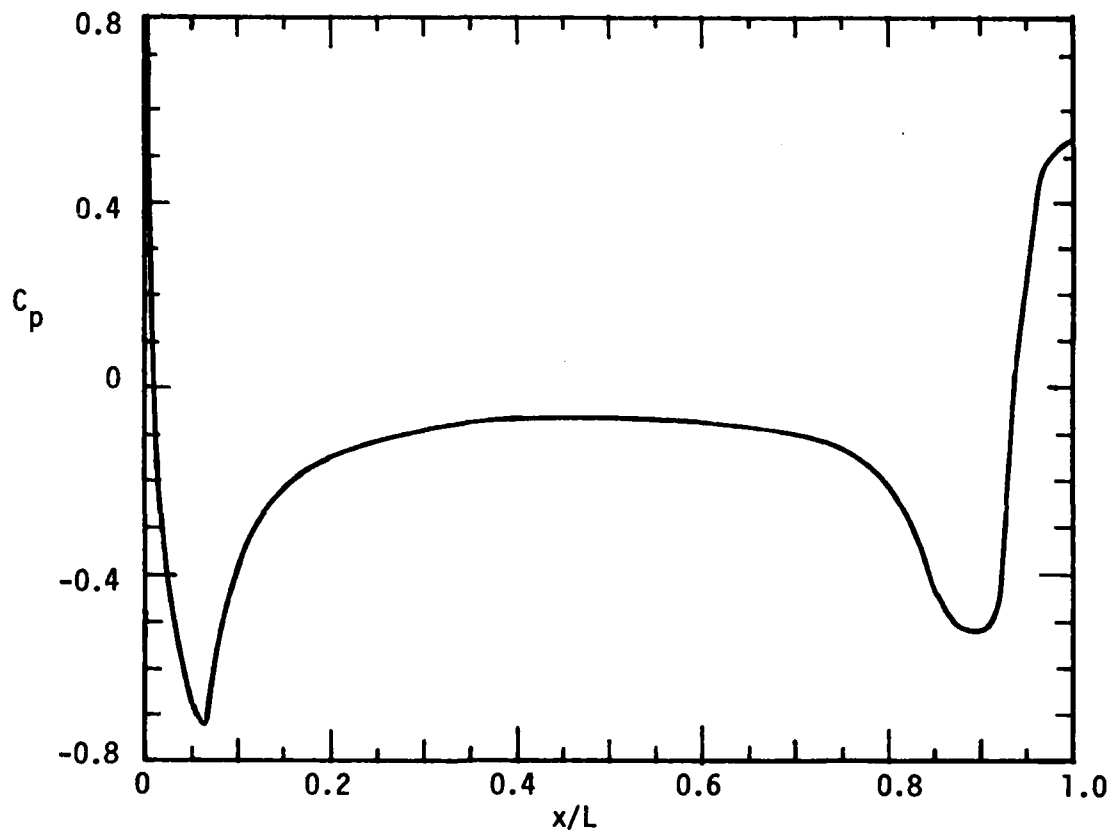


FIGURE 6-2 THRUST-DRAG AND POWER CHARACTERISTICS
FOR IMPROVED ATV AT $Re_y^{1/3} = 1.2 \times 10^6$



	NOSE	CENTER OF BUOYANCY	INTAKE	AFTER-BODY LIP	FIN LEADING EDGE	TERMINUS
STATION (INCHES)	0.00	38.36	66.00	71.34	73.83	82.95
DIAMETER (INCHES)	0.00	17.65	16.79	15.10	13.40	0.00
AREA (SQ. INCHES)			—	12.56		
VOLUME (CF)	9.91					

FIGURE 6-3 ADVANCED UNDERWATER VEHICLE CONFIGURATION

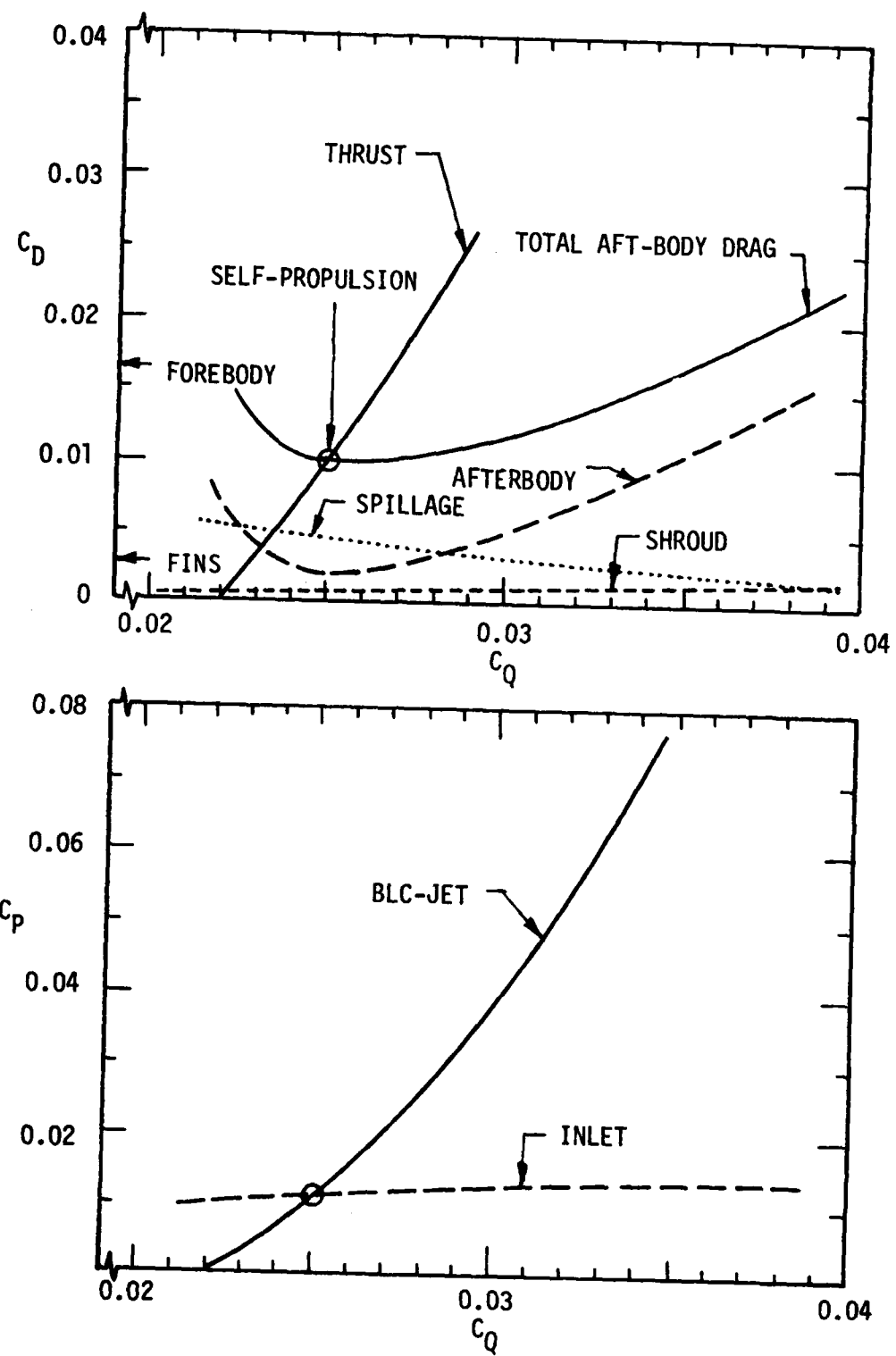


FIGURE 6-4 THRUST-DRAG AND POWER CHARACTERISTICS
FOR AUV AT $Re_{1/3} = 1.2 \times 10^6$

does not require that a large portion of the forebody momentum deficit be ingested into the intake.

The AUV total fluid power coefficient for self propulsion ($C_{P_i} + C_{P_j}$) is 0.022 at $Re_V^{1/3} = 1.2 \times 10^6$, for a statically-stable vehicle configuration. This represents a 35 percent reduction in propulsion power requirements compared to the improved ATV configuration and over 50 percent less than the ATV test configuration. In addition, for a cylindrically constrained application, the AUV offers a very substantial increase in available vehicle volume, a characteristic of paramount importance for weapon applications.

The predicted fluid-power characteristics for the improved ATV, AUV, and ATV test configuration are provided in Figure 6-5, along with the ATV wind tunnel data. All curves represent analytical predictions based on methodology validated in this report. As illustrated, propulsor power characteristics follow expected Reynolds number scaling behavior.

Advanced Tactical Vehicle test data include results from both wind tunnel facilities, Vought low speed wind tunnel and David Taylor Naval Ship Research and Development Center. As indicated, very close agreement between both facilities and the prediction methodology is evident.

Data points for a spherical forebody configuration with a discrete afterbody suction slot²³ are included in Figure 6-4. Data with transition at 10 percent of the body length was used, similar to that for the other configurations shown. A fin power increment of 0.004, as cited in reference 23, was included.

Two important aspects of the integrated BLC propulsion vehicle performance should be emphasized. First, drag characteristics are wholly determined by fluid friction effects within the turbulent boundary layers formed on the body and thus are accurately evaluated using the methodology described in this report. Thus higher speeds and/or larger bodies may be simply treated by using standard boundary layer codes. Likewise, conventional Reynolds number scaling is equally applicable. Secondly, verification of the HDV wind tunnel data with the range test data assures that, for this type integrated propulsor, total propulsor thrust and power requirements can reliably be determined

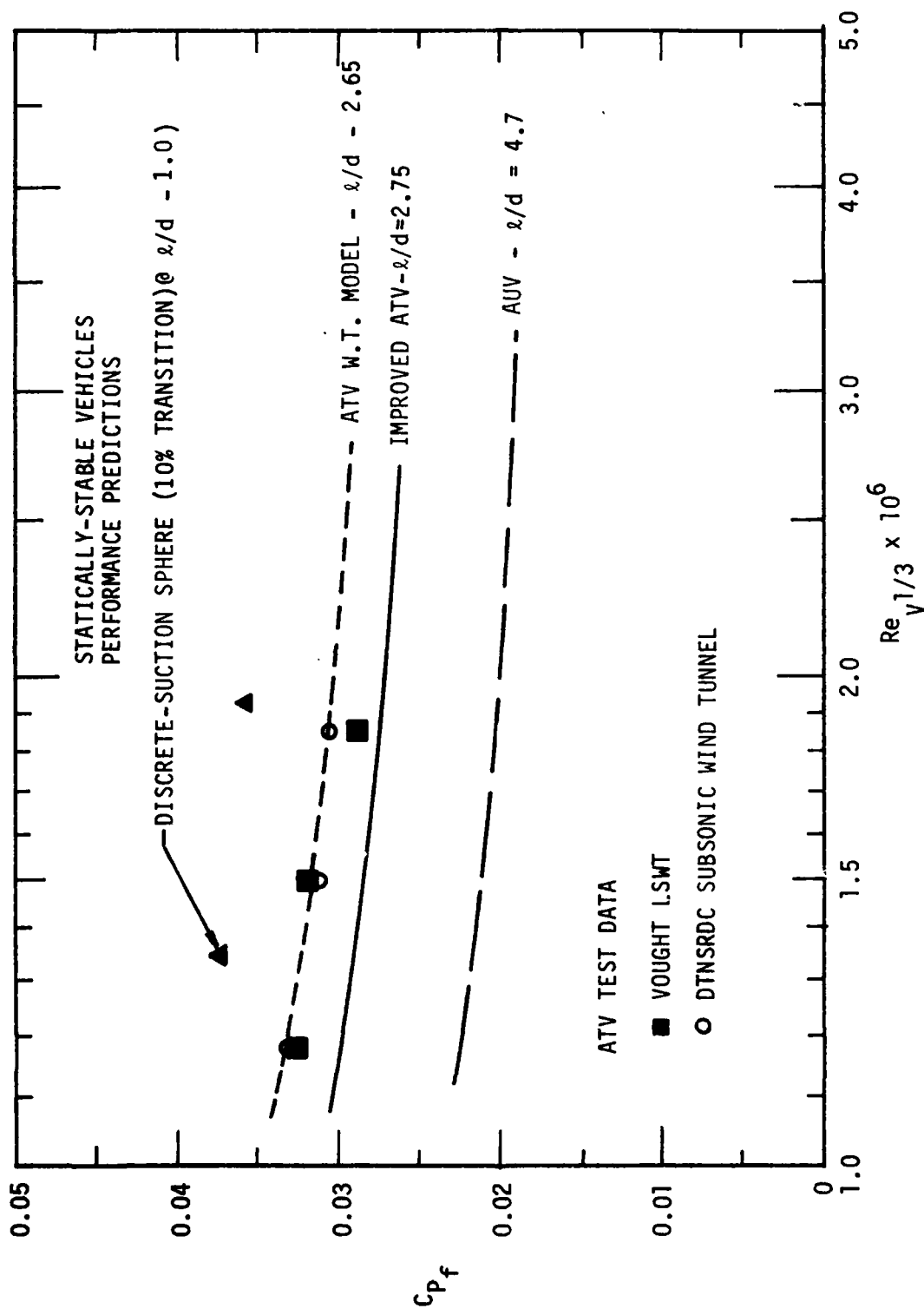


FIGURE 6-4 POWER COEFFICIENT COMPARISON

in wind tunnel facilities. That is, the propulsor flow and head coefficient requirements for zero net force (thrust = drag) in a wind tunnel are the same as those of a self-propelled vehicle operating in water at the same Reynolds number. Thus vehicle performance for the Vought BLC-propulsor can confidently be predicted over a wide range of missions.

7.0 CONCLUSIONS

The conclusions of this test program can be best drawn by addressing each individual objective that was established at the initiation of this study.

1. "Demonstrate hydrodynamic propulsive performance for a 2.65 fineness ratio turbulent-flow body employing an integrated propulsive/BLC afterbody."

CONCLUSION - The low-drag, low-installed-power characteristics of such a configuration were completely demonstrated and validated in this wind tunnel test. The analytical methodology based on a "mixing model" characterization of the afterbody drag was verified. Close agreement was achieved between prediction and experiment for the total integrated system as well as for the individual constituents.

2. "Provide wind tunnel test validity for hydrodynamic vehicle by comparing with in-water free-running test vehicle range performance."

CONCLUSION - Experimental data were obtained that provide a direct comparison between the performance of the HDV in the wind tunnel and its performance in the free-running in-water range demonstration program. HDV drag characteristics determined in the range test program were verified by the wind tunnel results, and were indeed duplicated in the Reynolds number range corresponding to the low-speed portion of the range tests.

Suspected off-design performance of the HDV radial inlet that occurred in the range program was verified in the wind tunnel, confirming the degradation in propulsive performance and distinguishing it from hydrodynamic drag characteristics. The evidence confirms that the wind tunnel provides a very accurate simulation of hydrodynamic performance.

3. "Verify the "design fix" for the range test vehicle."

CONCLUSION - As described above, the wind tunnel test results confirmed the drag characteristics and performance demonstrated by the HDV in the range test program. The radial inlet performance was verified as the factor that most prevented the HDV from accelerating to the speed range that would have placed the BLC jet "on design." The change to a higher flow-rate, lower-velocity BLC jet, with an attendant change in the inlet to relieve viscous blockage effects (submerged inlet design) demonstrated

the ability to achieve low afterbody drag performance (i.e., self-propulsion at lower jet velocity ratios). Further modifications to eliminate the tailboom and place the control fins on the closed afterbody (IRV configuration) brought the total configuration drag down to a level that matched the goals of the original HDV program. The design fix was not totally achieved, as the submerged inlet performance fell below expectations. However, these results reinforced the confidence in designing and predicting the performance of an integrated afterbody BLC propulsor and emphasized the difficulty of integrating a suction inlet with a laminar flow body.

4. "Assess the applicability of this concept to advanced underwater vehicles."

CONCLUSION - The applicability of the concept for advanced underwater vehicles was fully demonstrated. The low-drag, low-power requirements were conclusively demonstrated. Analysis of a higher-fineness-ratio configuration ($\ell/d = 4.7$) clearly shows a significant reduction in propulsor power requirements relative to more conventional approaches. Additionally, the inherent ability to design for a high-prismatic-coefficient, fully turbulent body, and the demonstration of enhanced control fin effectiveness on the propulsive afterbody supports the practicability of an advanced underwater vehicle based on this concept.

In summary, the Vought integrated afterbody propulsor concept has been validated as a viable mature-technology approach to new, high-performance underwater vehicles. Benefits may be realized through design for very long-range, long-endurance missions at moderate speeds or for short-duration missions at very high speeds. In both cases, the concept offers tangible benefits in packaging efficiency and payload capability.

REFERENCES

1. ATC Underwater Prototype, Contract No. N00140-77-D-6471.
2. Krall, K. M. and Rudderow, W. H., "A Low Drag Advanced Torpedo Concept," ATC Report No. B-94300/6TR-5, December 1976 (CONFIDENTIAL).
3. Wallace, D. B., "Experimental Results of a Blown Axisymmetric ATC Afterbody," ATC Report No. B-94300/7TR-11, April 1977.
4. A Low Speed Wind Tunnel Test Investigating the Static Stability Derivatives and Fin Effectiveness of the Vought Full Scale ATC Underwater Vehicle," Vought Report 2-53730/7R-3381, July 1977.
5. Spangler, J. G., and Carollo, S. F., "Development and Testing of the Propulsion System for an Advanced Underwater Vehicle," ATC Report No. B-91100/8TR-, October 1978.
6. Spangler, J. G. and Wallace, D. B., "Range Tests of the ATC Underwater Prototype," ATC Report No. B-91100/8CR-89, May 1978.
7. Spangler, J. G. and Wallace, D. B., "Range Tests of the ATC Underwater Prototype with Modified Afterbody," ATC Report No. B-91100/8CR-124, October 1978.
8. Krall, K. M., Rudderow, W. H., and Spangler, J. G., "Free-Running Tests of an ATC Underwater Vehicle," ATC Report No. R-91200/9TR-3, March 1979.
9. Spangler, J. G., Wallace, D. B., and Krall, K. M., "Intake Design and Evaluation for the ATC Underwater Vehicle," ATC Report No. R-91200/0TR-, April 1980.
10. Report of the Hydrodemonstration Committee, Prepared for Naval Underwater Systems Center, May 1979 (CONFIDENTIAL).
11. Krall, K. M. and Spangler, J. G., "Performance Assessment of the ATC Hydrodemonstration Vehicle," Final Report, ATC Report No. R-91200/0TR-5, July 1980.
12. Schmidt, W. F., "Water Droplet Impingement Prediction for Engine Inlets by Trajectory Analysis in a Potential Flow Field-Final Report," Boeing Company Report Nos. D3-6961, D3-6961-1, D3-696-2, 29 December, 1965.
13. Gentry, A. E. and Wazzan, A. R., "The Transition Analysis Program System," Naval Sea Systems Command Report No. J7255/02, June 1976.
14. Kerney, K. P. and White, N. M., "Description and Evaluation of a Digital Computer Program for Calculating the Viscous Drag of Bodies of Revolution," NSRDC Report No. 4641, Dec. 1975.
15. Gartshore, I. S. and Newman, B. G., "The Turbulent Wall Jet in an Arbitrary Pressure Gradient," The Aeronautical Quarterly, February 1975.
16. Mangler, W., "Zusammenhang Zwischen ebenen und rotationssymmetrischen Grenzschichten in kompressiblen Flussigkeiten," SAMM 28, 97-103 (1948). See also Schlichting, Boundary Layer Theory, McGraw-Hill.

17. Miner, E. W. and Lewis, C. H., "A Finite-Difference Method for Predicting Supersonic Turbulent Boundary Layer Flows with Tangential Slot Injection," NASA CR-2124, October 1972.
18. Hoerner, S. F., and Burst, H. V., Fluid Dynamic Lift, Published by Mrs. L. A. Hoerner, Brick Town, N. J., 1975.
19. Schlichting, H., Boundary Layer Theory, McGraw-Hill Book Co., Inc., New York, 1968.
20. Winski, S. Z., "Stress Analysis of Support System For ATV Full-scale LSWT Model," Vought Report No. 2-53700/1R-96, 15 May, 1981.
21. Preston, J. H., "The Determination of Turbulent Skin Friction by Means of Pitot Tubes," J. Roy Aero. Soc., 58, 1954.
22. Patel, V. C., "Calibration of the Preston Tube and Limitations on Its Use in Pressure Gradients," J. Fluid Mech., Vol. 23, 1, 1964.
23. Leitner, R. T., and McCabe, E. F., "Preliminary Assessment of the Feasibility of a Low-drag Spherical Submersible," David W. Taylor Naval Ship Research and Development Center Report No. DTNSRDC/ASED-81/20, Dec. 1981.

DISTRIBUTION LIST

<u>ADDRESSEE</u>	<u>NUMBER OF COPIES</u>
Director Defense Advanced Research Projects Agency Attention: Program Management/MIS 1400 Wilson Boulevard Arlington, Virginia 22209	3
Defense Technical Information Center Cameron Station Alexandria, Virginia 22314	12
TACTEC Battelle Memorial Institute 505 King Avenue Columbus, Ohio 43201	1
Commander (1603) David W. Taylor Naval Ship R&D Center Bethesda, Maryland 20084	25